Integration of Dye Lasers and Microfluidics for Biochemical Analysis

Thesis by

Yan Chen

In Partial Fulfillment of the Requirements
for the Degree of
Doctor of Philosophy

California Institute of Technology
Pasadena, California

2009

(Defended July 18th, 2008)

Acknowledgements

The six years at Caltech have been the most memorable time in my life so far, I owe many thanks for my experience here. First of all, I would like to thank my advisor, Prof. Axel Scherer, for providing me with the opportunity and resources to complete my Ph.D. at Caltech. I am grateful to his guidance and support through all these years. His broad perspective, valuable advice, and sincere mentorship have always been a source of inspiration and motivation.

I would also like to thank my committee members: Prof. Changhuei Yang, Prof. Oskar Painter, Prof. Yu-Chong Tai, and Prof. Chin-Lin Guo, and other members in my candidacy committee: Prof. Mory Gharib, and Prof. Mladen Barbic.

My great thanks go to my collaborators: Dr. Zhenyu Li and Dr. John Zhong. It has been great to work with Dr. Zhenyu Li, I am most grateful for all the helpful discussions and valuable advice from him. Collaboration with Dr. John Zhong in USC Medical School has been very fruitful and enjoyable. I thank him for providing many valuable resources for research, and being a great friend.

The Nanofabrication group is a great place to work and study. I would like to thank all the members in the Caltech Nanofabrication Group. I would first like to thank Dr. Zhaoyu Zhang, who helped me get started from the first day I arrived in the lab. I also benefit a lot from many of our former group members, Dr. George Maltezos, Dr. Saurabh Vyawahare, Dr. Tereal Neal, Dr. Koichi Okamoto, Dr. Michael Hochberg, Dr. Tom Baehr-Jones, Dr. Emil Kartalov, and Dr. Joyce Wong. I am grateful to the remaining members of the Nanofabrication group for their support and help in the lab, and their friendship, Chris

Walker, Teresa Emery, Lin Zhu, David Henry, Michael Shearn, Uday Khankhoje, Guangxi Wang, Ting Hong, Jingqing Huang, and Sameer Walavalkar. I would like to thank our secretary, Kate Finigan, and our lab coordinator, Dr. Guy DeRose, who have been working hard to enable an efficient working environment for all of us. I have been extremely fortunate to work with so many wonderful people in my time at Caltech.

Finally, but most importantly, I am eternally grateful to my parents and my grandmother for their unconditional love, constant support and confidence in me throughout my life. Above all I owe my deepest thanks to Jiarui Han, for his tremendous love, encouragement, and support during the past six years, none of this could have been accomplished without him.

Abstract

This dissertation describes the study of two important aspects of integration in microfluidics: optics and biochemistry. In optics integration, two types of miniaturized dye lasers, namely the solid-state polymer dye lasers and optofluidic dye lasers were demonstrated. Both of the dye lasers possess a resonant cavity with circular grating geometry, and they are suitable to serve as low-threshold, surface-emitting coherent light source in microfluidic networks. The mass production and large scale fabrication of such low-cost dye laser arrays can be realized by the well developed nanoimprint and soft lithography, making this technology attractive for various biochemical applications. In biochemistry integration, a microfluidic system was developed to fully utilize the complexity of microfluidic circuits to process single cells and extract gene expression information in a parallel manner. The work presented here explored both the optics and biochemistry integration in microfluidics, which are the key issues for further development of complete "lab-on-a-chip" systems.

Contents

List of Figures

List of Tables

Glossary of acronyms

2D – Two-dimensional

DBR – Distributed Bragg reflector

DFB – Distributed feedback

ESEM – Environmental scanning electron microscope

FDTD – Finite difference time domain

FP – Fabry-Perot

FWHM – Full width at half maximum

MIBK – Methyl isobutyl ketone

OSA – Optical spectrum analyzer

PL – Photoluminescence

RIE – Reactive ion etching

PMMA – Poly(methyl methacrylate)

Q – Quality factor

SEM – Scanning electron microscope

Chapter 1

Introduction

1.1 Overview

1.1.1 Optics in microfluidics

The field of microfluidics continues to become an important area with novel applications in biotechnology [1]. The most important goal for microfluidics is to achieve a complete “lab-on-a-chip” system, which is capable of performing biological and chemical experiments normally carried out in a standard full-size laboratory. While efforts are made to develop the microfluidic system to realize more functionality for various biochemical reactions, the integration of optical components into microfluidic systems becomes more and more indispensable.

Optical detection and spectroscopic analysis are important in most micrototal analysis systems (μTAS) [2]. Currently a majority of microfluidic systems are based on external light sources. However, the coupling of optical signals in and out of the devices, typically by optical fibers, remains one of the major challenges in integrated optics. By making on-chip light sources, we can eliminate the optics alignment, which greatly reduces the complexity of the system. Therefore, the integration of miniaturized active light sources such as lasers into microfluidic systems becomes an attractive approach for biological and chemical processes.

We are very interested in the miniaturization and integration of dye lasers into microfluidic systems because of their broadband tunablity, low cost, and easy fabrication. Dye lasers have been widely used as tunable, coherent light sources for spectroscopic analysis in the visible wavelength region (from 400 nm to 900 nm) during the past 30 years [3]. Miniaturized dye lasers, which can be integrated in lab-on-a-chip microsystems, would similarly have numerous applications. For applications in biochemical analysis in microfluidic systems, a surface emitting laser is more useful than other lasers because of its stacked substrate structure. Therefore, we choose a circular grating structure as the laser resonator design to produce low-threshold surface emitting lasing. The laser operating characteristics can be significantly improved by the two-dimensional nature of the resonator structure.

Two types of miniaturized dye lasers with the circular grating geometry are demonstrated in this thesis: solid-state and optofluidic dye lasers. For the solid-state dye laser, the laser dye is doped in the polymer forming the laser resonator, and it is fabricated using nanoimprint lithography. For the microfluidic dye laser, the laser dye is dissolved in an organic solvent and flowed through a microfluidic channel with laser resonator embedded, and it is realized by soft lithography. They can produce high-intensity and narrow-linewidth lasing with a well-defined output beam.

The well developed nanoimprint and microfluidics technology provide a convenient way of mass production and large-scale fabrication of low-cost dye laser arrays with a wide wavelength output range. It is also straightforward to build on-chip dye lasers with waveguides to replace the optical fibers necessary for the integrated optics. The miniaturized dye lasers can serve as surface emitting coherent light sources, which are very important in various biochemical applications, such as laser-induced fluorescence and spectroscopy.

1.1.2 Biochemistry in microfluidics

As we study the optical integration in microfluidic systems towards fully functional "lab-on-a-chip" system, we are exploring more capabilities of the microfluidic system in the field of biochemical analysis. Lab-on-a-chip devices have the potential to revolutionize biochemistry by allowing complicated biochemical procedures to be performed on a small microfluidic chip. Single-cell processing is one of the major applications of microfluidics that can take advantage of its nanoliter fluid handing abilities.

A microfluidic approach that can extract gene expression information from individual single cells is described in this thesis. The integrated process: cell capture/lysis, mRNA isolation/purification, and cDNA synthesis/purification for single human embryonic stem cells is implemented on a microfluidic device. With the improved design of the microfluidic circuit, a parallel processing of dozens of cells with 100% efficiency can be achieved.

The gene expression of human embryonic stem cells (hESC) is a critical aspect for understanding the normal and pathological development of human cells and tissues. Current bulk gene expression assays rely on RNA extracted from cell and tissue samples with various degree of cellular heterogeneity. These "cell population averaging" data are difficult to interpret, especially for the purpose of understanding the regulatory relationship of genes in the earliest phases of development and differentiation of individual cells. Here, we report a microfluidic approach that can extract total mRNA from individual single cells and synthesize cDNA on the same device with high mRNA-to-cDNA efficiency. This feature makes large-scale single-cell gene expression profiling possible. Using this microfluidic device, we measured the absolute numbers of mRNA molecules of three genes in a single hESC. Our results indicate that gene expression data measured from the cDNA of a cell population is not a good representation of the expression levels in individual single cells. Within the G0/G1 phase pluripotent hESC population some individual cells did not express all of the 3 interrogated genes in detectable levels. Consequently, the relative expression levels, which are broadly used in gene expression studies, are very different between measurements from population cDNA and single-cell cDNA. The results underscore the importance of discrete single-cell analysis, and the advantages of a microfluidic approach in stem-cell gene expression studies.

1.2 Thesis organization

The thesis is organized as follows: Chapter 2, Chapter 3 and Chapter 4 focus on the optics integration of the microfluidic system, and Chapter 5 highlights the biochemistry aspect of the microfluidic system.

Chapter 2 extensively studies the modeling of circular grating resonators using transfer matrix method. An analytical model is developed to locate the resonance in a circular grating resonator. Both the parameters from solid-state and optofluidic dye lasers have been applied to the analytical model, and the simulation results are compared with experimental data. Chapter 3 describes the fabrication of solid-state polymer dye lasers using nanoimprint lithography. The detection result of the surface emitting dye laser with a circular grating geometry is discussed. Chapter 4 presents the fabrication of optofluidic dye lasers using soft lithography. A hybrid material system is introduced to make functional microfluidic laser devices. Chapter 5 demonstrates the use of microfluidic system as a platform to perform single-cell gene analysis. Chapter 6 concludes the thesis with an outlook of the future work for integration of optics with microfluidics for various biochemical applications.

Chapter 2

Modeling of circular grating structure by transfer matrix method

2.1 Introduction

2.1.1 Circular grating

Laser (*Light Amplification by Stimulated Emission of Radiation*) is composed of a gain medium and a resonant optical cavity [4]. The gain medium amplifies the beam by stimulated emission, and the resonant cavity provides the feedback necessary for the lasing operation. For our solid-state and optofluidic dye lasers in Chapter 3 and Chapter 4, we choose the circular grating resonator as laser cavities for their unique two-dimensional nature and enhanced lasing performance.

In particular, we use the second-order circular grating distributed feedback (DFB) structure as the resonant cavity. The distributed feedback scheme indicates that the gain material is directly implemented in the grating structure. The circular grating DFB structure satisfies the second-order Bragg condition, $\lambda_{Bragg} = n_{eff}\Lambda$, where λ_{Bragg} is the emission wavelength, n_{eff} is the effective index of the waveguide mode, and Λ is the grating period, with an inner cavity providing a quarter- or half-wavelength shift similar to the classical DFB case.

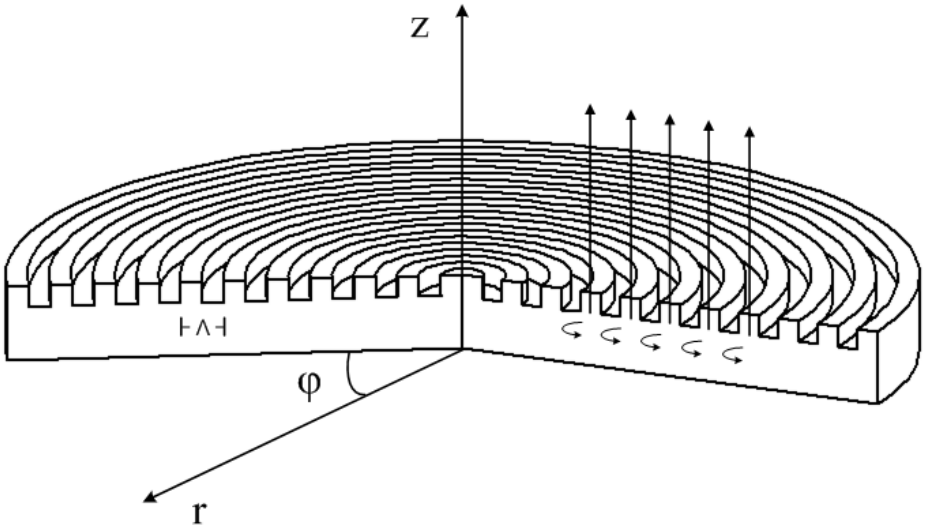

Figure 2.1: Diagram of a circular grating resonator design. The scheme illustrates the second-order Bragg diffraction including (1) normal diffraction to the grating surface (first-order) and (2) in-plane feedback (second-order).

The second-order grating is used to obtain surface emission, because it not only couples counter-propagating radial waves (via second-order Bragg reflection), but also induces coupling of radially propagating waves into the direction normal to the grating surface (via first-order Bragg reflection). Fig. 2.1 shows a cut-away diagram of a typical circular grating resonator. The corrugations in the grating structure provide both distributed feedback and output coupling of the guided optical mode via second-order and first-order Bragg scattering.

2.1.2 Transfer matrix method

To understand the resonant behavior of the circular grating, a theoretical analysis is necessary. There are many methods for modeling circular optical resonators. Most of the models are based on couple mode theory [5-9], which is more suitable for analyzing circular grating structure with shallow trenches and a modest light confinement. In this chapter, we present a transfer matrix method for analyzing circular grating structure with deep etched trenches. The deeper trenches of the structure lead to stronger in-plane effective index modulation, therefore the resonator can confine light in a smaller volume.

The transfer matrix method [10] is a straightforward method for analyzing optical structures composed of an arbitrary number of dielectric layers. When the dielectric properties are taken into account and the boundary conditions are satisfied, a transfer matrix can relate the electromagnetic field on either side of an optical region. Therefore, a complex structure can be modeled by simple matrix multiplication of basic subcomponents. The transfer matrix method is suitable to analysis of various resonant optical cavities, such as multi-section Fabry-Perot, DBR, DFB, and VCSEL geometries [11]. For our application, we are interested in utilizing transfer matrix method for the analysis of structures with cylindrical symmetry.

In this chapter, we derive a transfer matrix method appropriate for description of the optical modes of circular grating microcavities. The electromagnetic modes of cylindrical multilayer structures are analyzed in terms of propagating waves, i.e., Hankel functions. In this chapter, the theoretical analysis follows the calculations of [12] and [13]. Using this transfer matrix method based 2-D cylindrical model, the spectrum information of the cavity modes can be obtained to analyze the energy confinement in the circular grating structure.

2.2 Transfer matrix analysis

2.2.1 Maxwell's equation

To solve the wave equation, we define $\vec{E}$ and $\vec{H}$ as the vector electric and magnetic fields in the circular grating structure, and they are represented by (E_z, E_r, E_φ) and (H_z, H_r, H_φ) in cylindrical coordinates. In our 2-D model, we simplify the circular Bragg grating to infinite cylinders, and consider the system invariant in the z direction. Therefore, the electrical field and magnetic field can be expressed as $\vec{E}(r,\varphi)e^{i\omega t}$ and $\vec{H}(r,\varphi)e^{i\omega t}$.

The Maxwell's equation is given below in its differential form

$$\begin{aligned} \nabla \times \vec{E} &= -\mu\, i\omega \vec{H} \\ \nabla \times \vec{H} &= \varepsilon\, i\omega \vec{E} \\ \nabla \cdot \vec{E} &= 0 \\ \nabla \cdot \vec{H} &= 0 \end{aligned} \tag{2.1}$$

where μ and ε are the magnetic permeability and dielectric permittivity in the grating structure, and ω is the angular frequency of the electromagnetic field.

At all layer interfaces, the tangential components of the electric and magnetic field $\vec{E}$ and $\vec{H}$ must be continuous. The system is invariant in z direction, therefore the solutions can be decomposed into two distinct polarizations: transverse electric (TE) and transverse magnetic (TM). We need to explore the general solutions of the Maxwell's equations for the cylindrical symmetry, i.e., Hankel functions, and use them to solve the optical modes based on the transfer matrix method.

We can derive the Helmholtz equation from Maxwell's equation and solve it for the cylindrical coordinate.

$$\left[\nabla^2 + k^2\right]\begin{bmatrix}\vec{E} \\ \vec{H}\end{bmatrix} = 0 \tag{2.2}$$

where k is the wavenumber in the grating structure and satisfies $k^2 = \omega^2 \mu\varepsilon$.

Expressing the Helmholtz equation in cylindrical coordinates, we have

$$\left[\frac{1}{r}\frac{\partial}{\partial r}(r\frac{\partial}{\partial r}) + \frac{1}{r^2}\frac{\partial^2}{\partial \varphi^2} + \frac{\partial^2}{\partial z^2} + k^2\right]\begin{bmatrix}\vec{E} \\ \vec{H}\end{bmatrix} = 0\,. \tag{2.3}$$

Because the system is invariant along the z coordinate, the separation in z components and in a transversal part is possible. Let $k^2 = k_T^2 + k_z^2$, where k_T and k_z represent the component for the polar and z coordinates, respectively.

If we apply the following variable separation to Eq. (2.3),

$$\begin{aligned} E_z(r,\varphi) &= A \cdot R(r)\Phi(\varphi) \\ H_z(r,\varphi) &= B \cdot R(r)\Phi(\varphi) \end{aligned} \tag{2.4}$$

the equation becomes

$$\Phi(\varphi)\frac{\partial^2 R(r)}{\partial r^2} + \Phi(\varphi)\frac{1}{r}\frac{\partial R(r)}{\partial r} + \frac{R(r)}{r^2}\frac{\partial^2 \Phi(\varphi)}{\partial \varphi^2} + R(r)\Phi(\varphi)k_T^2 = 0\,. \tag{2.5}$$

The equation can be separated into two parts with only dependence on r and φ, and each part can be solved on its own.

$$\frac{r^2}{R(r)}\frac{\partial^2 R(r)}{\partial r^2} + \frac{r}{R(r)}\frac{\partial R(r)}{\partial r} + r^2 k_T^2 = -\frac{1}{\Phi(\varphi)}\frac{\partial^2 \Phi(\varphi)}{\partial \varphi^2} = m^2 \tag{2.6}$$

The solution of $\frac{\partial^2\Phi(\varphi)}{\partial\varphi^2}+m^2\Phi(\varphi)=0$ is either

$$\begin{cases} \Phi(\varphi)=\cos(m\varphi), & m\varphi=\pi l \\ \Phi(\varphi)=\sin(m\varphi), & m\varphi=\pi(l+\frac{1}{2}). \\ \Phi(\varphi)=e^{im\varphi} & \end{cases} \tag{2.7}$$

The equation below is known as the Bessel differential equation

$$\frac{r^2}{R(r)}\frac{\partial^2 R(r)}{\partial r^2}+\frac{r}{R(r)}\frac{\partial R(r)}{\partial r}+(r^2k_T^2-m^2)=0. \tag{2.8}$$

Therefore, the general solution of the time harmonic electromagnetic field is the Hankel function, which is a linear combination of Bessel and the Neumann function,

$$\begin{aligned} \mathrm{H}_m{}^{(1)}(r)=J_m(r)+iN_m(r) \\ \mathrm{H}_m{}^{(2)}(r)=J_m(r)-iN_m(r) \end{aligned} \tag{2.9}$$

$\mathrm{H}_m{}^{(1)}$ and $\mathrm{H}_m{}^{(2)}$ are the first-kind and second-kind Hankel functions, respectively, m is the azimuthal order, J_m is the Bessel function, and N_m is the Neumann function.

The solutions of variable separated equations can be inserted into Eq. (2.4),

for the TE mode, $$H_z^j(r,\varphi) \;=\; \sum_{m=0}^{\infty}[\alpha_m\mathrm{H}_m{}^{(1)}(r)+\beta_m\mathrm{H}_m{}^{(2)}(r)]\cdot e^{im\varphi}\;. \tag{2.10}$$

for the TM mode, $$E_z^j(r,\varphi) \;=\; \sum_{m=0}^{\infty}[\alpha_m\mathrm{H}_m{}^{(1)}(r)+\beta_m\mathrm{H}_m{}^{(2)}(r)]\cdot e^{im\varphi}\;. \tag{2.11}$$

2.2.2 Transfer matrix method

The schematic circular grating laser structure is shown in Fig. 2.2. The circular grating structure consists of N infinite cylindrical concentric layers. Each layer consists of alternating dielectric materials with refractive indices n_I and n_{II}.

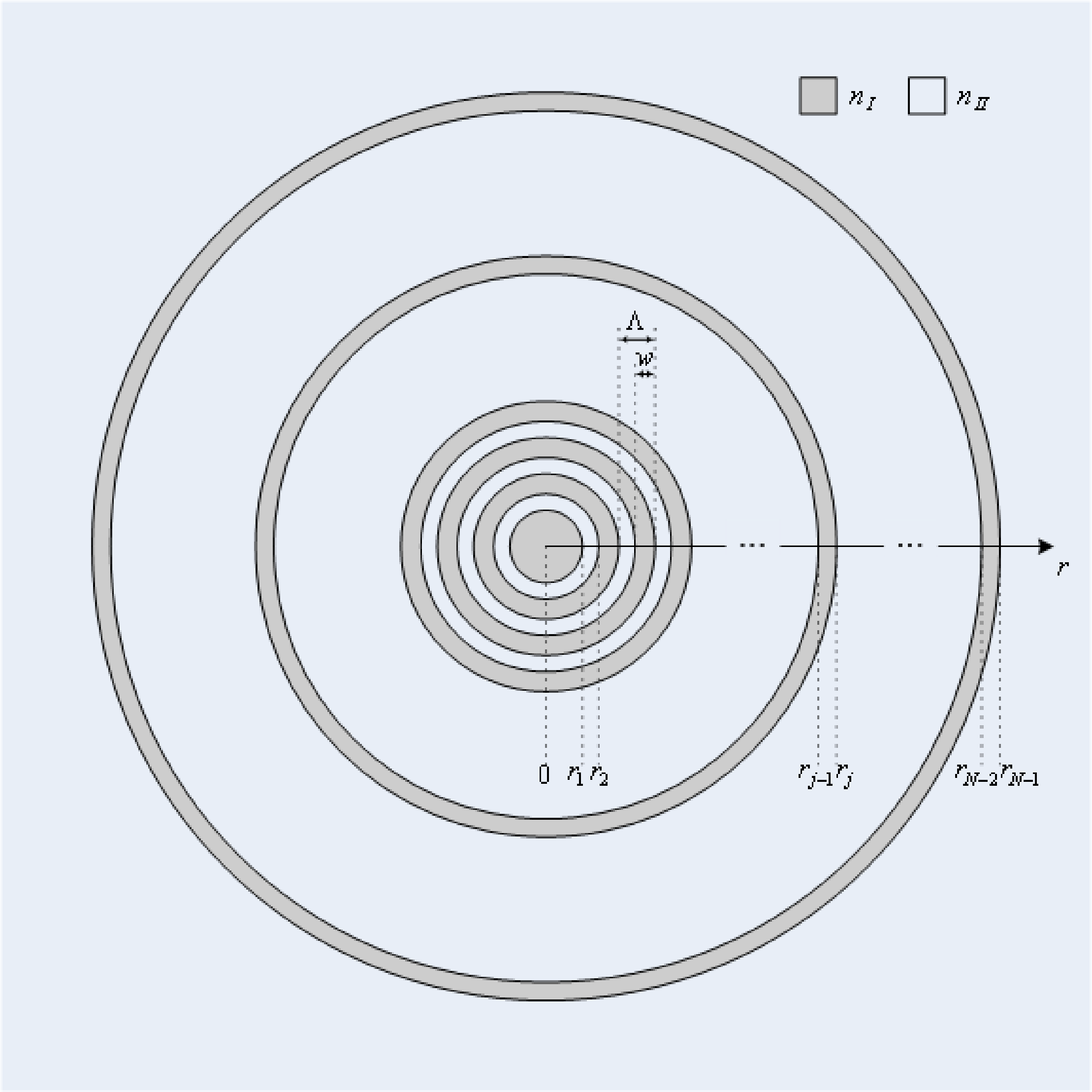

Figure 2.2: Schematic representation of a circular grating structure, with grating period Λ, duty cycle $d_c = w/\Lambda$, effective indices n_I and n_{II}, cavity radius $r_1, r_2, \cdots, r_{N-1}$.

Our goal is to describe the field propagating in a cylindrical waveguide structure shown in Fig. 2.2. Due to the 2-D nature of the problem, the field solutions can be decomposed into TE and TM polarizations, for which the field in the plane is entirely characterized by (H_z, E_r, E_φ) and (E_z, H_r, H_φ), respectively. The present cylindrical geometry suggests we expand the fields using first-kind and second-kind Hankel functions, $\mathrm{H}_m{}^{(1)}$ and $\mathrm{H}_m{}^{(2)}$, which are linearly independent and represent the inward and outward propagating circular (Hankel) waves.

We are mainly considering the TE polarization, since the perpendicular pumping light on the grating surface will cause almost pure excitation of TE waves [23]. As described in the previous chapter, the general TE solutions of the Maxwell's equations in each layer j can be expressed as a linear combination of $\mathrm{H}_m{}^{(1)}(n_j k_0 r)e^{im\varphi}$ and $\mathrm{H}_m{}^{(2)}(n_j k_0 r)e^{im\varphi}$ for each mode $m = 0,1,\ldots,\infty$, n_j is the effective refractive index in each layer j.

The H-field is expressed as

$$\begin{aligned} H_z^j(r,\varphi) &= \sum_{m=0}^{\infty}[\alpha_m^j \mathrm{H}_m{}^{(1)}(n_j k_0 r) + \beta_m^j \mathrm{H}_m{}^{(2)}(n_j k_0 r)]\cdot e^{im\varphi} \\ &= \sum_{m=0}^{\infty} H_z^{j,m}(r)\cdot e^{im\varphi} \end{aligned} \quad . \tag{2.12}$$

Based on Maxwell's equations, $\nabla \times H = \varepsilon_0 n_j^2 i\omega E$,

$$\begin{pmatrix} \partial/\partial z \\ \partial/\partial r \\ \partial/\partial\varphi \end{pmatrix} \times \begin{pmatrix} H_z^j \\ 0 \\ 0 \end{pmatrix} = \begin{pmatrix} 0 \\ \partial H_z^j/\partial\varphi \\ -\partial H_z^j/\partial r \end{pmatrix} = \varepsilon_0 n_j^2 i\omega \begin{pmatrix} 0 \\ E_r^j \\ E_\varphi^j \end{pmatrix} \tag{2.13}$$

$$\begin{aligned} E_r^j(r,\varphi) &= \frac{1}{\varepsilon_0 n_j^2 i\omega}\sum_{m=0}^{\infty}[\alpha_m^j \mathrm{H}_m{}^{(1)}(n_j k_0 r) + \beta_m^j \mathrm{H}_m{}^{(2)}(n_j k_0 r)]\cdot m e^{im\varphi} \\ &= \sum_{m=0}^{\infty} E_r^{j,m}(r)\cdot e^{im\varphi} \end{aligned} \tag{2.14}$$

$$\begin{aligned} E_{\varphi}^{j}(r,\varphi) &= \frac{i}{\varepsilon_0 n_j c}\sum_{m=0}^{\infty}[\alpha_m^j \mathrm{H}_m'^{(1)}(n_j k_0 r)+\beta_m^j \mathrm{H}_m'^{(2)}(n_j k_0 r)]\cdot e^{im\varphi} \\ &= \sum_{m=0}^{\infty} E_{\varphi}^{j,m}(r)\cdot e^{im\varphi} \end{aligned} \quad . \qquad (2.15)$$

$\mathrm{H}_m'^{(1)}$ and $\mathrm{H}_m'^{(2)}$ are the derivative of $\mathrm{H}_m{}^{(1)}$ and $\mathrm{H}_m{}^{(2)}$, respectively.

Similarly, for TM polarization, the E -field is expressed as

$$\begin{aligned} E_{z}^{j}(r,\varphi) &= \sum_{m=0}^{\infty}[\alpha_m^j \mathrm{H}_m{}^{(1)}(n_j k_0 r)+\beta_m^j \mathrm{H}_m{}^{(2)}(n_j k_0 r)]\cdot e^{im\varphi} \\ &= \sum_{m=0}^{\infty} E_{z}^{j,m}(r)\cdot e^{im\varphi} \end{aligned} \quad . \qquad (2.16)$$

Based on Maxwell's equations, $\nabla \times E = -\mu_0 i\omega H$,

$$\begin{pmatrix} \partial/\partial z \\ \partial/\partial r \\ \partial/\partial\varphi \end{pmatrix} \times \begin{pmatrix} E_z^j \\ 0 \\ 0 \end{pmatrix} = \begin{pmatrix} 0 \\ \partial E_z^j/\partial\varphi \\ -\partial E_z^j/\partial r \end{pmatrix} = -\mu_0 i\omega \begin{pmatrix} 0 \\ H_r^j \\ H_\varphi^j \end{pmatrix} \qquad (2.17)$$

$$\begin{aligned} H_{r}^{j}(r,\varphi) &= -\frac{1}{\mu_0\omega}\sum_{m=0}^{\infty}[\alpha_m^j \mathrm{H}_m{}^{(1)}(n_j k_0 r)+\beta_m^j \mathrm{H}_m{}^{(2)}(n_j k_0 r)]\cdot m e^{im\varphi} \\ &= \sum_{m=0}^{\infty} H_{r}^{j,m}(r)\cdot e^{im\varphi} \end{aligned} \qquad (2.18)$$

$$\begin{aligned} H_{\varphi}^{j}(r,\varphi) &= \frac{n_j}{\mu_0 i c}\sum_{m=0}^{\infty}[\alpha_m^j \mathrm{H}_m'^{(1)}(n_j k_0 r)+\beta_m^j \mathrm{H}_m'^{(2)}(n_j k_0 r)]\cdot e^{im\varphi} \\ &= \sum_{m=0}^{\infty} H_{\varphi}^{j,m}(r)\cdot e^{im\varphi} \end{aligned} \quad . \qquad (2.19)$$

2.2.3 Transfer matrix method coefficients

At the interface between the j^{th} and $(j+1)^{th}$ layers, located at $r = r_j$, the tangential fields components (E_z, H_φ for TM polarization; H_z, E_φ for TE polarization) must be continuous. The coefficients calculations of Transfer Matrix below are based on TE polarizations.

$$\begin{aligned} E_z^j(r_j,\varphi) &= E_z^{j+1}(r_j,\varphi) \\ H_z^j(r_j,\varphi) &= H_z^{j+1}(r_j,\varphi) \end{aligned} \tag{2.20}$$

The relationship between the coefficients (α_m^j, β_m^j), $(\alpha_m^{j+1}, \beta_m^{j+1})$ can be expressed by

$$\begin{pmatrix} \alpha_m^{j+1} \\ \beta_m^{j+1} \end{pmatrix} = \begin{pmatrix} a_m^j & b_m^j \\ b_m^{j*} & a_m^{j*} \end{pmatrix} \begin{pmatrix} \alpha_m^j \\ \beta_m^j \end{pmatrix} \tag{2.21}$$

where a_m^{j*}, b_m^{j*} are the complex conjugates of a_m^j, b_m^j.

$$\begin{aligned} a_m^j &= \frac{1}{D_m^j}\left[\mathrm{H}_m^{(1)}(n_j r_j k_0)\mathrm{H}_m'^{(2)}(n_{j+1} r_j k_0) - \gamma\ \mathrm{H}_m^{(2)}(n_{j+1} r_j k_0)\mathrm{H}_m'^{(1)}(n_j r_j k_0)\right] \\ b_m^j &= \frac{1}{D_m^j}\left[\mathrm{H}_m^{(2)}(n_j r_j k_0)\mathrm{H}_m'^{(2)}(n_{j+1} r_j k_0) - \gamma\ \mathrm{H}_m^{(2)}(n_{j+1} r_j k_0)\mathrm{H}_m'^{(2)}(n_j r_j k_0)\right] \end{aligned} \tag{2.22}$$

with the index ratio $\gamma = \dfrac{n_{j+1}}{n_j}$,

$$D_m^j = \mathrm{H}_m^{(1)}(n_{j+1} r_j k_0)\mathrm{H}_m'^{(2)}(n_{j+1} r_j k_0) - \mathrm{H}_m^{(2)}(n_{j+1} r_j k_0)\mathrm{H}_m'^{(1)}(n_{j+1} r_j k_0). \tag{2.23}$$

For TM polarization, the only difference is the index ratio $\gamma = \dfrac{n_j}{n_{j+1}}$.

We can obtain an overall transfer matrix relating the inner cavity to the outmost ring by multiplying the transfer matrices for each layer. For $j = 1,2,\ldots,N-1$,

$$\begin{pmatrix} \alpha_m^N \\ \beta_m^N \end{pmatrix} = T_m^N \cdot \begin{pmatrix} \alpha_m^1 \\ \beta_m^1 \end{pmatrix}. \tag{2.24}$$

The overall transfer matrix T_m^N takes the form

$$T_m^N = \begin{pmatrix} A_m^N & B_m^N \\ B_m^{N*} & A_m^{N*} \end{pmatrix} = \begin{pmatrix} a_m^{N-1} & b_m^{N-1} \\ b_m^{N-1*} & a_m^{N-1*} \end{pmatrix} \cdots\cdots \begin{pmatrix} a_m^1 & b_m^1 \\ b_m^{1*} & a_m^{1*} \end{pmatrix} \tag{2.25}$$

with

$$T_m^1 = \begin{pmatrix} A_m^1 & B_m^1 \\ B_m^{1*} & A_m^{1*} \end{pmatrix} = \begin{pmatrix} 1 & 0 \\ 0 & 1 \end{pmatrix}. \tag{2.26}$$

In order to find resonant modes, we can assume $\alpha_m^1 = \beta_m^1$, since every incoming wave can be considered as an outgoing one after crossing the z axis. The power in each layer j can be defined as $P_m^j = \left|\alpha_m^j\right|^2 + \left|\beta_m^j\right|^2$.

Therefore the ratio of the electromagnetic power confined in the center ring P_m^1 to that in the outmost ring P_m^N is

$$R_m = \frac{P_m^1}{P_m^N} = \frac{\left|\alpha_m^1\right|^2 + \left|\beta_m^1\right|^2}{\left|\alpha_m^N\right|^2 + \left|\beta_m^N\right|^2} \tag{2.27}$$

$$\begin{aligned} \alpha_m^N &= A_m^N \cdot \alpha_m^1 + B_m^N \cdot \beta_m^1 = (A_m^N + B_m^N) \cdot \alpha_m^1 \\ \beta_m^N &= B_m^{N*} \cdot \alpha_m^1 + A_m^{N*} \cdot \beta_m^1 = (A_m^{N*} + B_m^{N*}) \cdot \beta_m^1 \end{aligned} \tag{2.28}$$

with $\left|\alpha_m^N\right|^2 = \alpha_m^N \alpha_m^{N*}$, $\left|\beta_m^N\right|^2 = \beta_m^N \beta_m^{N*}$, we obtain

$$\left|\alpha_m^N\right|^2 + \left|\beta_m^N\right|^2 = \left|\alpha_m^1\right|^2 \cdot \left|A_m^N + B_m^N\right|^2 + \left|\beta_m^1\right|^2 \cdot \left|A_m^N + B_m^N\right|^2 . \tag{2.29}$$

So the Power ratio R_m between the center ring and the outmost ring can be expressed as the function of the wavelength by transfer matrix elements A_m^N and B_m^N,

$$R_m = \frac{1}{\left|A_m^N + B_m^N\right|^2} . \tag{2.30}$$

The power ratio can give us an estimation of the resonance peak of the cavity modes in the absence of any source input, which helps us to have a good understanding of the energy confinement in our circular grating structures.

We can also estimate the field in the microcavity with the assumption $\alpha_m^1 = \beta_m^1$,

$$\begin{pmatrix} \alpha_m^j \\ \beta_m^j \end{pmatrix} = \begin{pmatrix} A_m^j & B_m^j \\ B_m^{j*} & A_m^{j*} \end{pmatrix} \cdot \begin{pmatrix} 1 \\ 1 \end{pmatrix} \quad \Leftrightarrow \quad \begin{aligned} \alpha_m^j &= A_m^j + B_m^j \\ \beta_m^j &= B_m^{j*} + A_m^{j*} = \alpha_m^{j*} \end{aligned} . \tag{2.31}$$

Therefore, in the TE polarization, we can write the H-field as a function of A_m^N and B_m^N

$$\begin{aligned} H_z^{j,m}(r) &= \alpha_m^j \mathrm{H}_m{}^{(1)}(n_j k_0 r) + \beta_m^j \mathrm{H}_m{}^{(2)}(n_j k_0 r) \\ &= \alpha_m^j \mathrm{H}_m{}^{(1)}(n_j k_0 r) + \alpha_m^{j*} \mathrm{H}_m{}^{(2)}(n_j k_0 r) . \\ &= 2\,\mathrm{Re}\left\{(A_m^j + B_m^j)\mathrm{H}_m{}^{(1)}(n_j k_0 r)\right\} \end{aligned} \tag{2.32}$$

Similarly, in the TM polarization, we can express the E-field as

$$E_z^{j,m}(r) = 2\,\mathrm{Re}\left\{(A_m^j + B_m^j)\mathrm{H}_m{}^{(1)}(n_j k_0 r)\right\}. \tag{2.33}$$

2.3 Simulation results

2.3.1 Index Matching

In order to introduce the finite vertical component of the waveguide grating into our transfer matrix formalism, we use the effective index approach. In this method, two characteristic cross sections, the groove and the tooth, form two different slab waveguides, providing effective indices n_I and n_{II} for the corresponding layers in our transfer matrix model.

The effective index approximation for the solid-state circular grating dye laser model is illustrated in Fig. 2.3. The laser waveguide consists of the top cladding (air), the dye-doped polymer film (PMMA), and the lower cladding (Cytop), with the refractive indices of $n_a = 1.0$, $n_f = 1.49$, $n_c = 1.34$, respectively. The variance between n_{eff1} and n_{eff2} is caused by the different thickness of polymer film in the groove and the tooth.

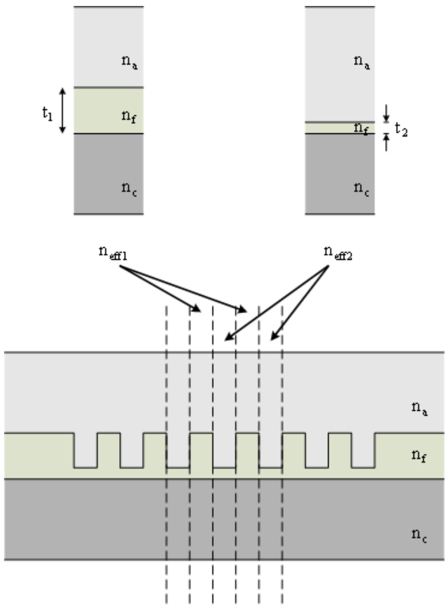

Figure 2.3: Effective index approximation of solid-state dye laser.

In the solid-state circular grating laser structure, the core thickness (the polymer thickness) is 1 um, and the grating trench depth is 400 nm, which gives the thickness of the two slab waveguides as $t_1 = 1\ \mu m$ and $t_2 = 600\ nm$. We can calculate the effective index using the 1-D multilayer waveguide solver [14]. The effective index of the tooth section is $n_{eff1} = 1.4791$, and the effective index of the groove section is $n_{eff2} = 1.3403$.

Similarly, the effective index approximation for the optofluidic circular grating dye laser model is illustrated in Fig. 2.4. The laser waveguide consists of the top cladding (PDMS), the liquid gain medium (dye solution), and the lower cladding (PFPE), with a refractive index of $n_t = 1.40$, $n_d = 1.54$, $n_l = 1.34$, respectively. The thickness of the two slab waveguides can be assumed as $t_1 = 1.6\ \mu m$ and $t_2 = 1\ \mu m$. The resulting effective index of the tooth section is $n_{eff1} = 1.5321$, and the effective index of the groove section is $n_{eff2} = 1.4007$.

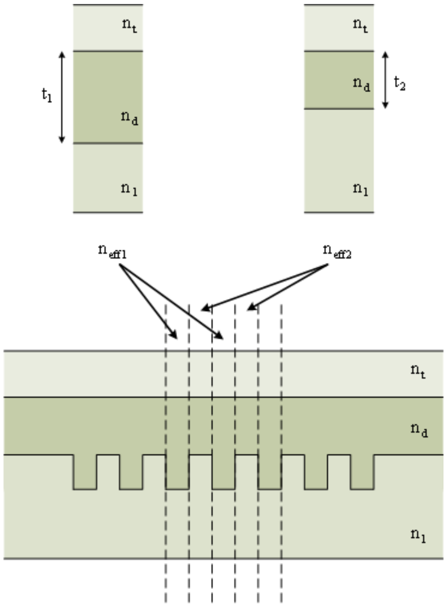

Figure 2.4: Effective index approximation of optofluidic dye laser.

2.3.2 Cavity resonance

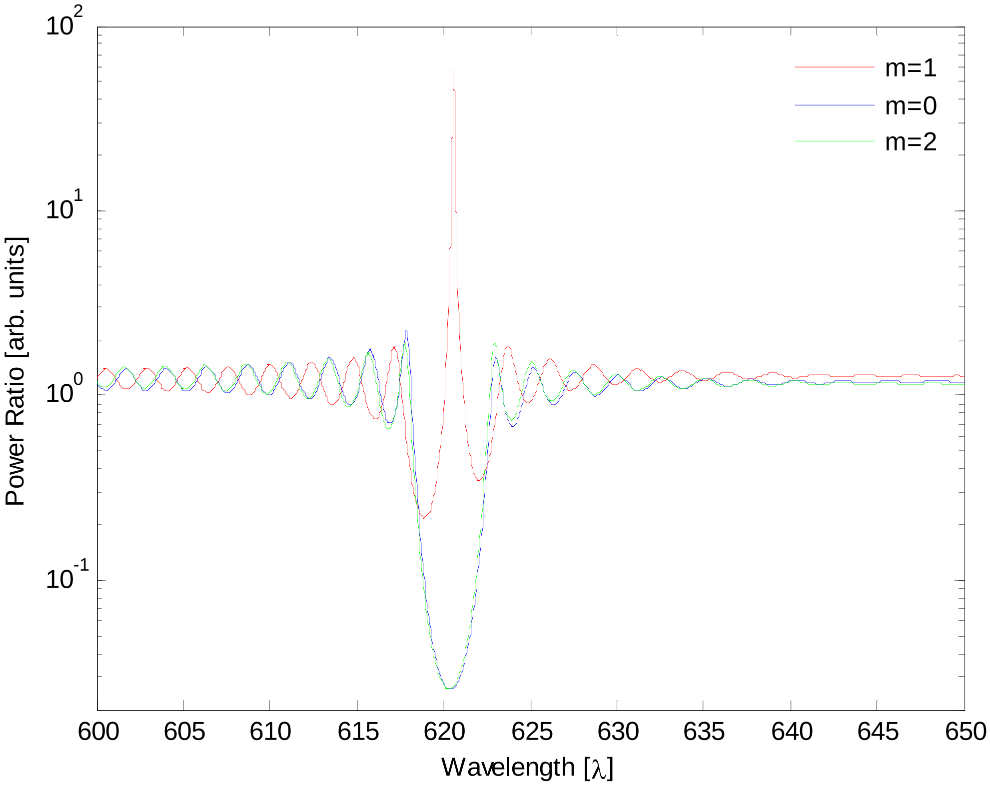

Figure 2.5: The power ratio in circular grating with period of 440 nm for m=0,1,2.

For the solid-state dye laser, the corresponding parameters are introduced to the transfer matrix method. We first choose the grating period to be 440, and the duty cycle to be 0.5. The effective indices are $n_I = 1.48$ and $n_{II} = 1.34$, respectively. The overall diameter of grating is 200 μm, which gives the grating layer number $N = 250$. In Fig. 2.5, we plot the power ratio between the center ring and the outmost ring for different modes $m = 0, \ 1, \ 2$. We observe a pronounced resonant peak at $m = 1$, but no peaks at $m = 0$ or $m = 2$.

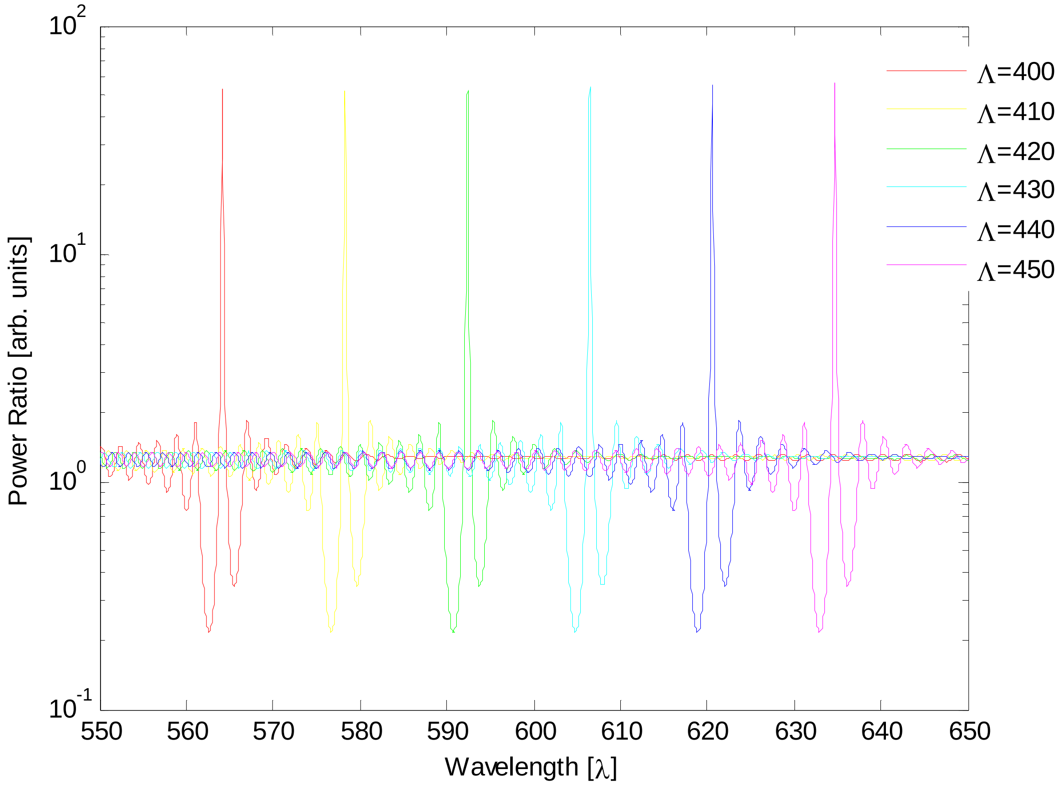

Figure 2.6: The power ratio in circular grating with period varying from 400 nm to 450 nm.

Fig. 2.6 shows the resonance peak corresponding to circular gratings with period from 400 nm to 460 nm. From the simulation results we can see that the cavity resonant modes fulfill the second-order Bragg condition $\lambda_{Bragg} = n_{eff}\Lambda$. The resonant peak for grating with a period of 440 nm matches very well with the experimental results in Chapter 3, which proves that the transfer matrix method is a powerful tool to reveal the spectrum information of the cavity modes.

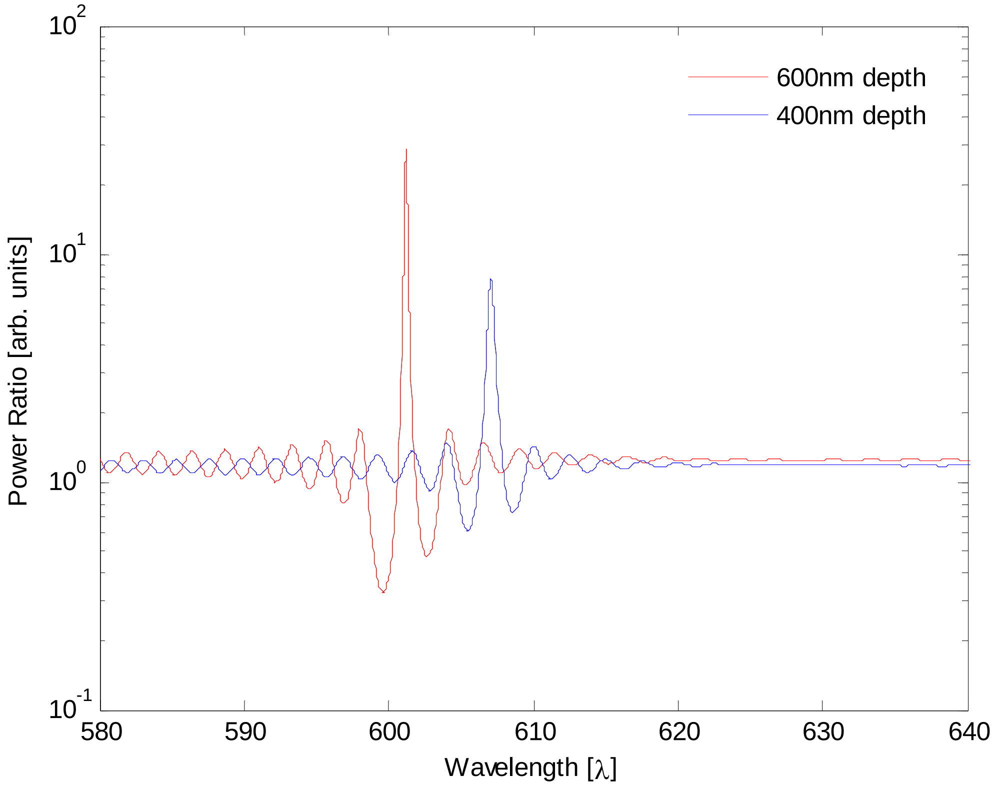

Figure 2.7: The power ratio in circular grating with two groove depths.

For the optofluidic dye laser, the main different grating parameters are their effective refractive indices. Due to the liquid configuration in fluidic dye laser, it is difficult to retrieve the exact waveguide thickness; here we assume the channel height is 1.6 μm. With a 400 nm groove depth, we obtain $n_I = 1.53$ and $n_{II} = 1.43$, if the depth increases to 600 nm, then we have $n_I = 1.53$ and $n_{II} = 1.40$. In Fig. 2.7, we compare the power ratio for these two sets of parameters for m=1. We can see that the resonance in 400 nm deep gratings is considerably weaker than that in the 600 nm deep gratings. Therefore, the low refractive index contrast between the dye solution and the cladding can be compensated for by the deeper grating trenches.

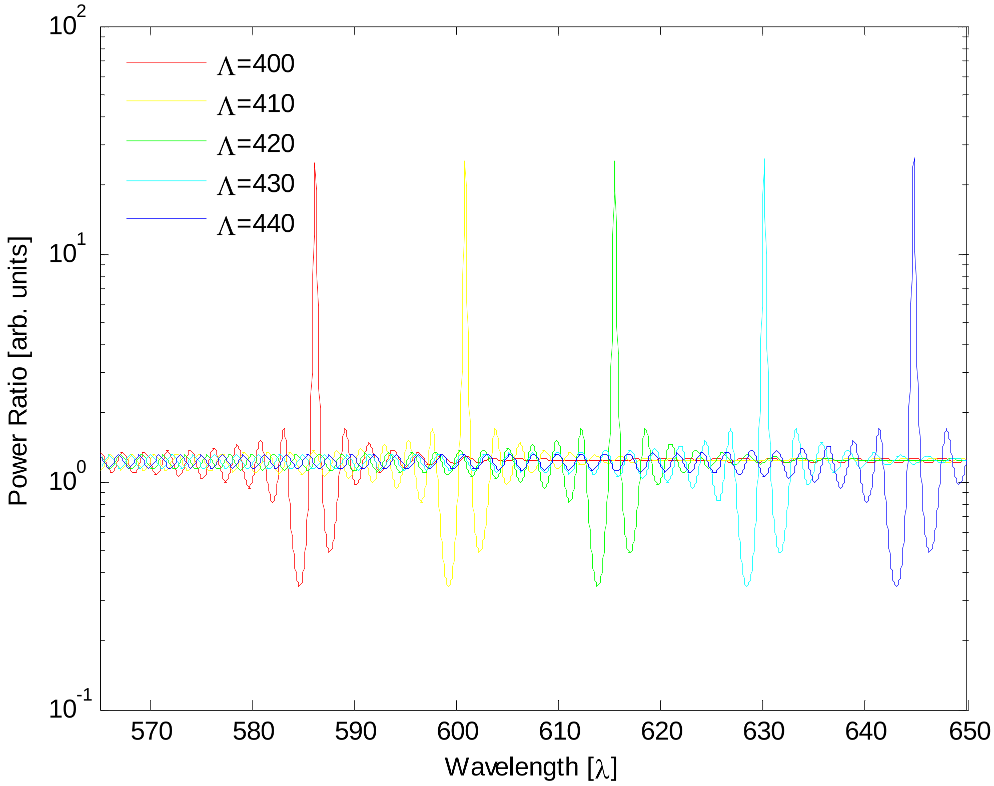

Figure 2.8: The power ratio in circular grating with period varying from 400 nm to 440 nm.

Fig. 2.8 shows a series of resonance in the circular grating with period varying from 400 nm to 440 nm for m=1. The effective refractive indices are $n_I = 1.53$ and $n_{II} = 1.40$, respectively. The duty cycle is 0.5, and the grating layer number is $N = 250$. The resonant peak for grating with period of 400 nm is also very close to the experimental results in Chapter 4.

2.3.3 Electromagnetic field plot

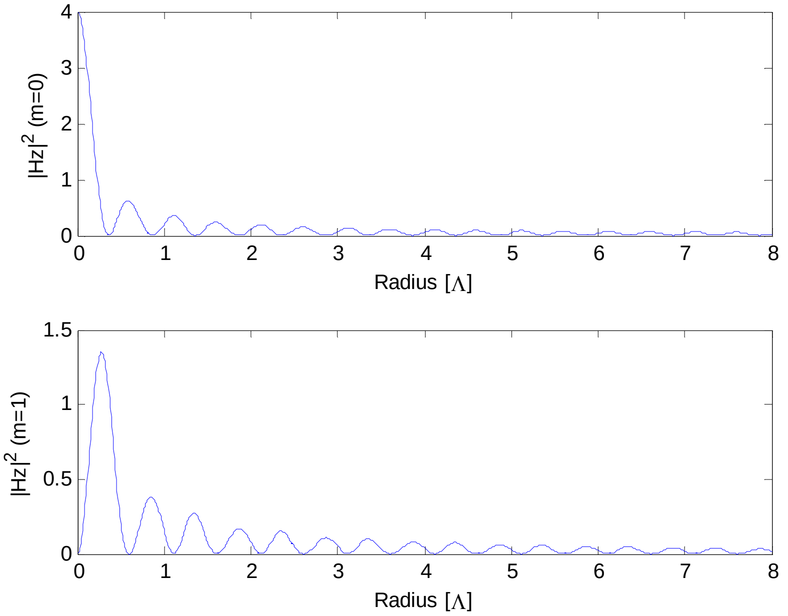

Figure 2.9: The 1-D graph of the normalized $H_z^{j,m}$ field in circular grating for m=0,1.

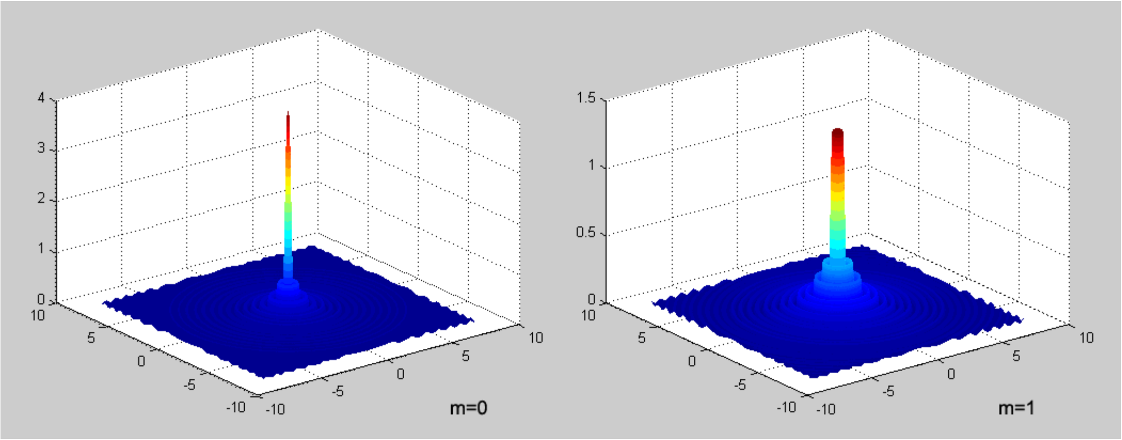

Figure 2.10: The 3-D graph of the normalized $H_z^{j,m}$ field in circular grating for m=0,1.

We can have a better understanding of the electromagnetic field in the circular grating by plotting the normalized $H_z^{j,m}$ field expressed by Eq. (2.32) for m=0 and m=1. Fig. 2.9 plots the 1-D graph of the $H_z^{j,m}$ field, and Fig. 2.10 plots the 3-D graph of the $H_z^{j,m}$ field. The graphs illustrate the electromagnetic field distribution of some fundamental modes in the microcavity.

Chapter 3

Nanoimprinted circular grating dye laser

3.1 Introduction

Within recent years the development of polymer dye lasers has progressed to higher levels of performance and functionality. The most attractive advantages of polymer dye lasers include low-cost processing, wide choice of emission wavelengths, and easy fabrication on flexible substrates. Several waveguide dye lasers have been studied with emission wavelengths ranging from ultraviolet to near infrared [15]. By simply changing the fluorophore doped in the polymer, these lasers can be used as the tunable sources for various applications, including spectroscopy [16].

The 1-D distributed feedback (DFB) structure is a widely employed resonator geometry, and has been previously demonstrated for polymer lasers [17]. Operating characteristics can be significantly improved within 2-D structures. Here, we choose a circular grating distributed feedback structure to obtain low threshold operation, a well-defined output beam, and vertical emission perpendicular to the device plane. Although surface emitting circular grating lasers using semiconducting polymers have been previously demonstrated by Bauer et al. [18] and Turnbull et al. [19], their lasers were fabricated by depositing the organic gain material onto prepatterned dielectric substrates, limiting the depth and the accuracy of the shape of the grating.

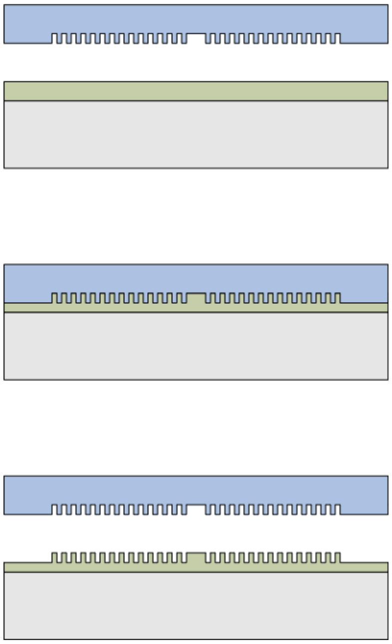

Figure 3.1: The general nanoimprint process.

For better geometric control, we choose nanoimprint lithography [20] as a direct patterning method. A hard mold is used to transfer patterns with high fidelity into target polymers, and this technique has become an attractive approach to define nanofabricated optical resonator structures. Conjugated polymer lasers fabricated by hot embossing have been studied by Lawrence et al. [21], and 1-D DFB lasers based on organic oligomers using a room temperature nanoimprint method were reported by Pisignano et al. [22, 23].

The basic idea of nanoimprint lithography is to press a mold with nanostructures on its surface into a thin layer of resist on a substrate, followed by the removal of the mold. The general nanoimprint process is illustrated in Fig. 3.1. This step creates a thickness contrast and duplicates the nanostructures in the resist film. During the imprint process, the resist is heated to a temperature above its glass transition temperature. At this temperature, the resist, which is thermoplastic, becomes a viscous liquid and can be deformed into the shape of the mold.

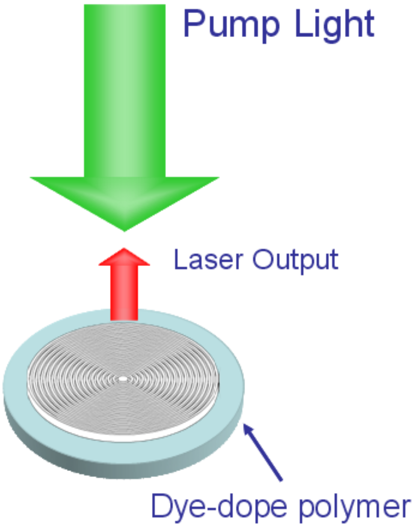

Figure 3.2: Schematic diagram of a nanoimprinted circular grating dye laser chip.

In this chapter, we report a circular grating distributed feedback laser fabricated on dye-doped poly(methylmethacrylate) (PMMA) films, as illustrated in Fig. 3.2. The laser was fabricated on a glass substrate using a low-cost and manufacturable nanoimprint method. Surface emission lasing with single frequency at 618 nm and a linewidth of 0.18 nm was measured from the polymer dye laser exhibiting a threshold value of 1.31 μJ/mm^2. The laser operation characteristics of the circular grating resonator are improved through the high accuracy and aspect ratio nanoimprint pattern transfer. Moreover, the mold can be re-used repeatedly, providing a convenient way of mass production and large-scale fabrication of low-cost polymer dye laser arrays.

3.2 Materials

3.2.1 PMMA

PMMA (poly(methylmethacrylate)) is a well-known highly transparent thermoplast. In our laser device, we chose PMMA to be the dye host matrix as well as the nanoimprint material. PMMA was selected as the polymer matrix because of its solubility of the dye molecules, as well as its low absorption at the wavelength for activating the dye molecule. Using PMMA in nanoimprint lithography is very common due to its good mold release properties and small shrinkage under large changes of temperature and pressure [24]. The building block for PMMA is shown in Fig. 3.3.

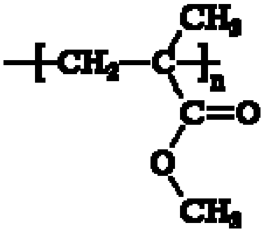

Figure 3.3: The monomer building block of PMMA.

3.2.2 Organic dye

The organic laser dye we use in the laser device is Rhodamine 640 (Exciton). This laser dye has excellent stability for its large quantum efficiency and relatively long life time before bleaching. We chose Rhodamine 640 to match its absorption peak with the cavity resonant frequency. The organic molecular structure is depicted in Fig. 3.4. To dope the organic dye molecules into the polymer, we mixed PMMA with chlorobenzene, methyl isobutyl ketone, ethanol, and Rhodamine 640 to make a 30 mM solution.

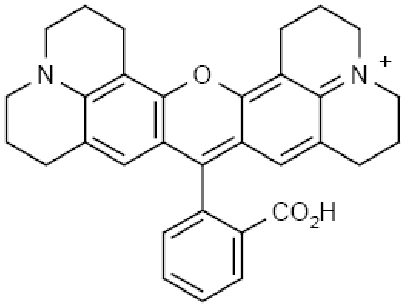

Figure 3.4: Rhodamine 640 molecule structure.

3.2.3 Cytop

Cytop is a low refractive index perfluoropolymer; its molecular structure is shown in Fig. 3.5. This cyclic fluoro-polymer, poly(1,1,2,4,4,5,5,6,7,7-decafluoro-3-oxa-1,6-heptadiene) is made by Asahi chemicals and used in the electronics industry. It is a hard but amorphous material with Tg ~ 1080 °C. We chose Cytop as a cladding material because of its low refractive index (n=1.34). The material system of PMMA and Cytop has previously been used for commercial polymer optical fibers and simple waveguides [25].

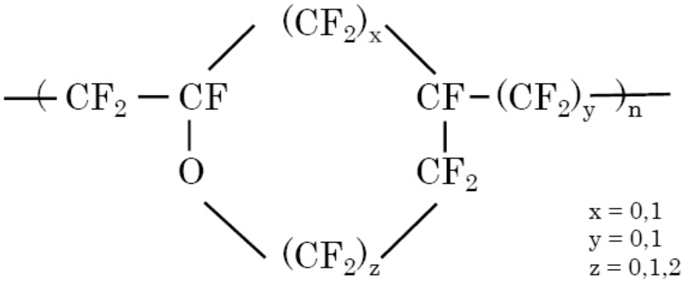

Figure 3.5: Cytop molecule structure.

3.3 Laser cavity design

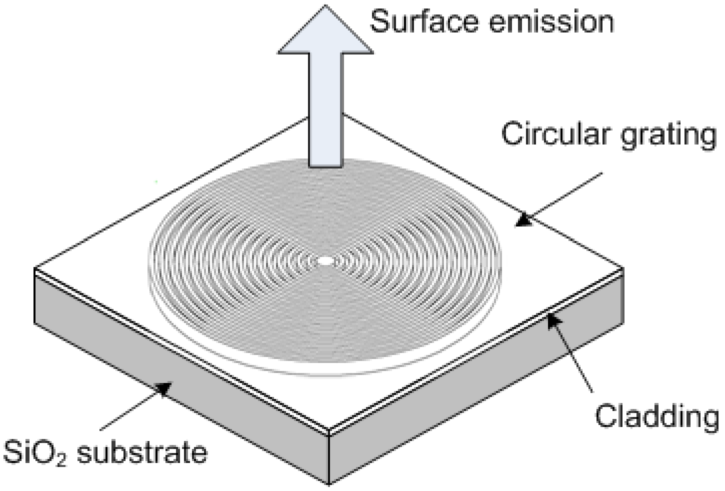

Figure 3.6: General design of a circular grating distributed feedback structure.

The circular grating structure proposed [6] and demonstrated [26] by Erdogan and Hall provides a natural 2-D extension of the basic DFB structure. It allows feedback to be applied in all in-plane directions, and the second-order grating couples the emitted radiation perpendicularly out of the surface of the sample. Fig. 3.6 shows a general design of a circular grating distributed feedback structure. A theoretical analysis of circular grating lasers is described in detail elsewhere [7-9, 27, 28] predicting that only the radial propagating components define the modes in the circularly symmetric grating.

The design parameters of the circular gratings fabricated are selected based on electromagnetic mode calculations and experimental results. A grating period of 440 nm is chosen to match the second-order Bragg condition. The center defect is a 440 nm diameter gain region. The 400 nm groove depth is defined to ensure maximum confinement, whereas the 200 μm overall diameter of the circular grating and the 50% duty cycle are used to reach the maximum coupling strength [29].

3.4 Fabrication process

3.4.1 Imprint mold fabrication

In our experiments, silicon dioxide (SiO_2) was used as the mold material. The grating pattern was defined by electron beam lithography on a LEICA EBPG 5000+ e-beam writer. 8% 495K PMMA was spun on a SiO_2 substrate for 1 min at 4500 rpm and baked for 15 min at 170 °C, which formed a 400 nm thick resist layer. The PMMA was exposed by electron beam at 100 keV and 800 $\mu C/cm^2$ with proximity correction. Development of patterned PMMA film was carried out in a 1:3 MIBK:IPA (methyl isobutyl ketone and isopropanol alcohol) solution for 1 min. The pattern was subsequently transferred from PMMA into SiO_2 substrate via reactive ion etching (RIE) using fluorine chemistry (CHF_3). The condition of RIE was 20 sccm, 60 mTorr of CHF_3 at 110 W for 15 min. Finally the PMMA residue was removed by sonicating the wafer in Chloroform for 2 min. The SiO_2 etching rate in the CHF_3 RIE process is 30 to 35 nm per min. Fig. 3.7 is the SEM image of the cross section of an etched SiO_2 grating with the etched depth of 400 nm. The schematic fabrication procedure for the nanoimprint hard mold is illustrated in Fig. 3.8.

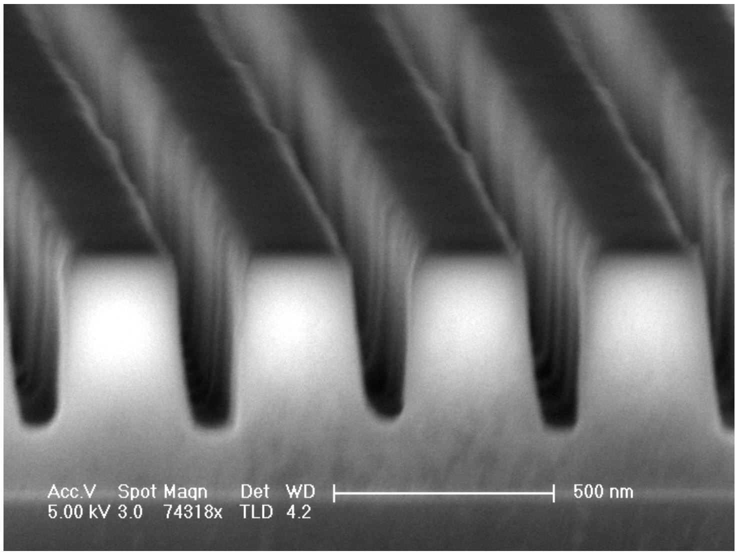

Figure 3.7: The SEM image of the cross section of an etched SiO_2 grating.

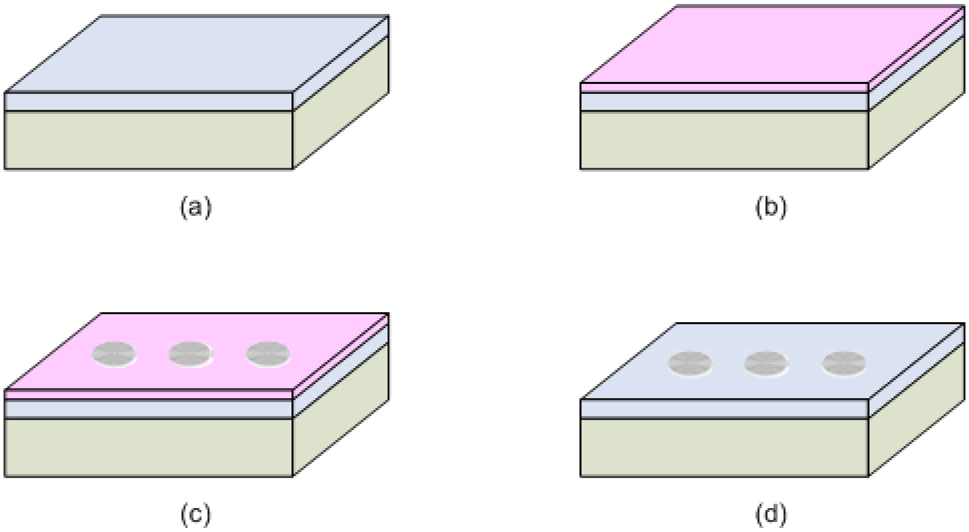

Figure 3.8: Schematic fabrication procedure for the circular grating nanoimprint hard mold. (a) The original wafer with 500 nm SiO_2 on top of silicon substrate. (b) PMMA is spun on the sample for subsequent e-beam lithography steps. (c) The PMMA is exposed by e-beam, and the circular grating pattern is completely transferred into PMMA after developing the exposed resist. (d) The pattern is transferred into the SiO_2 via CHF_3 RIE etch, and the PMMA residue is removed after dry etch.

The SEM images of both the top view and the angled view of an etched SiO_2 mold of circular grating are shown in Fig. 3.9. The grating period is 440 nm, with a center defect of 440 nm and an overall diameter of 200 μm. The trench depth is 400 nm.

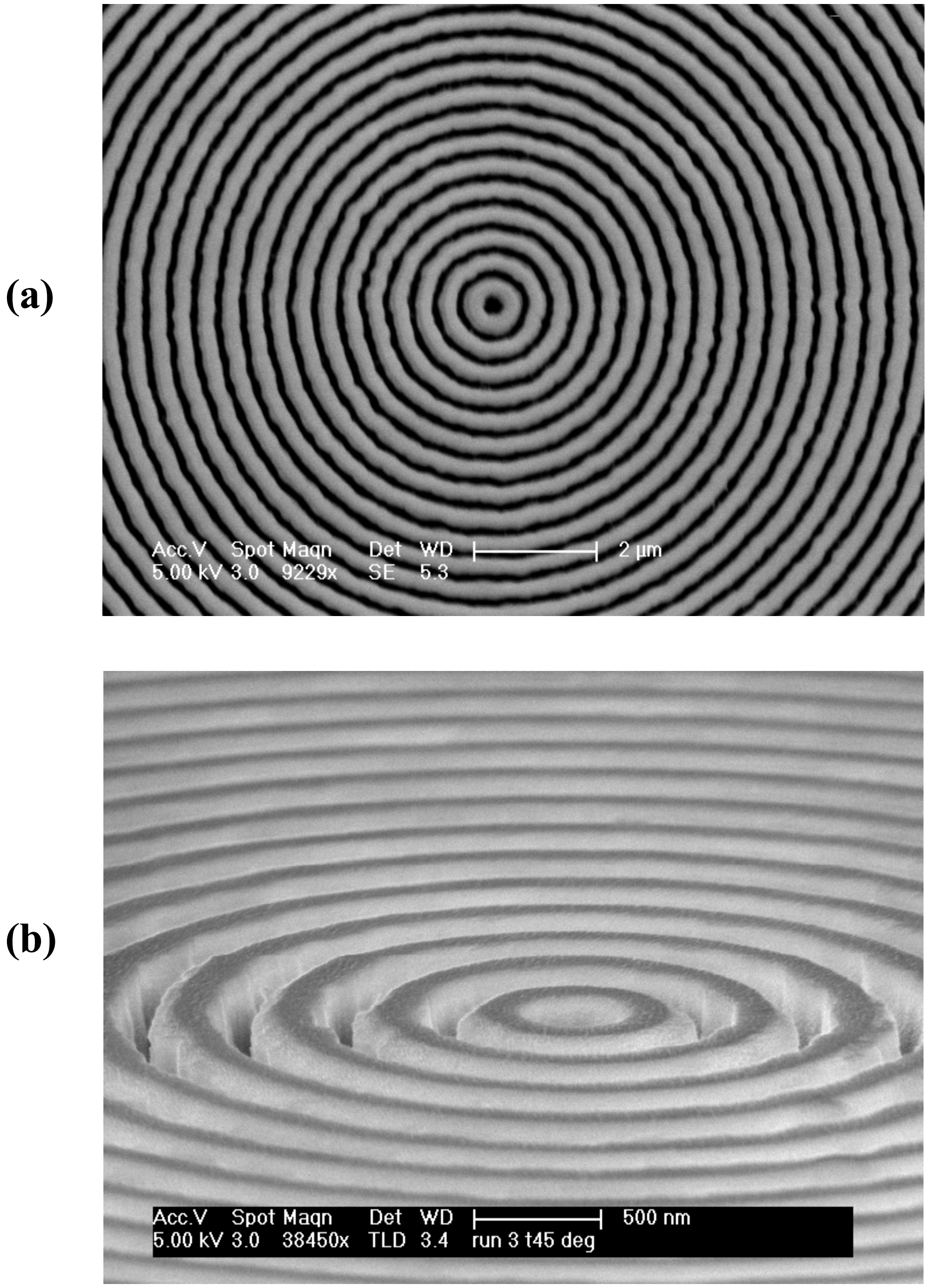

Figure 3.9: SEM images of (a) the top view and (b) the angled view of SiO_2 mold.

3.4.2 Laser chip fabrication

The laser chip consists of three layers, the substrate, the cladding, and the polymer matrix. PMMA was selected as the polymer matrix because of the solubility of the dye in PMMA, as well as its low optical absorption within the wavelength range for activating the dye molecules, and its excellent properties for nanoimprint lithography.

To construct the dye laser, a glass substrate (SiO_2) was spin-coated with Cytop, a low-refractive-index material (n=1.34) as the lower cladding to ensure the vertical optical confinement. After an oxygen plasma treatment to improve the adhesion of Cytop to the PMMA, dye-doped PMMA (n=1.49) was spun on top of the Cytop layer to serve as the gain medium.

The Cytop and PMMA preparation process for the nanoimprint process is summarized in Fig. 3.10. We began the fabrication process by depositing a 5 μm thick layer of Cytop (CTL-809M, Asahi Glass) on a silicon dioxide substrate. The deposition of the Cytop was accomplished via a series of spinning and thermal curing steps to ensure flatness and uniformity over the wafer. First, we spun the Cytop on the substrate at 1500 rpm (adhesion promoters were not necessary). Next, the Cytop was baked at 65 °C for 60 s, 95 °C for 60 s, and 180 °C for 20 min. The ramping of the bake temperature was critical in attaining flat and uniform surfaces. The spinning and baking steps were then repeated two more times, with a final bake at 180 °C for 3 hours. After the chip cooled down, an oxygen plasma treatment (Anatech SP100) of the Cytop was necessary for the adhesion of Cytop to PMMA. We exposed the oxygen plasma to Cytop at an RF power of 80 W and O_2 pressure of 200 mTorr for 30 s.

Next, dye (Rhodamine 640, Exciton)-doped PMMA (30 mM) was spin-coated on top of the Cytop layer at 500 rpm for 15 s and then 5000 rpm for 1 min. This produced a dye-doped polymer thin film with 600 nm thickness as the gain medium. A prebake at 170 °C for 2 min before the nanoimprint process ensured solvents were evaporated and improved the adhesion between the Cytop and PMMA. Then the substrate was ready for the nanoimprint process to define the laser cavity structure.

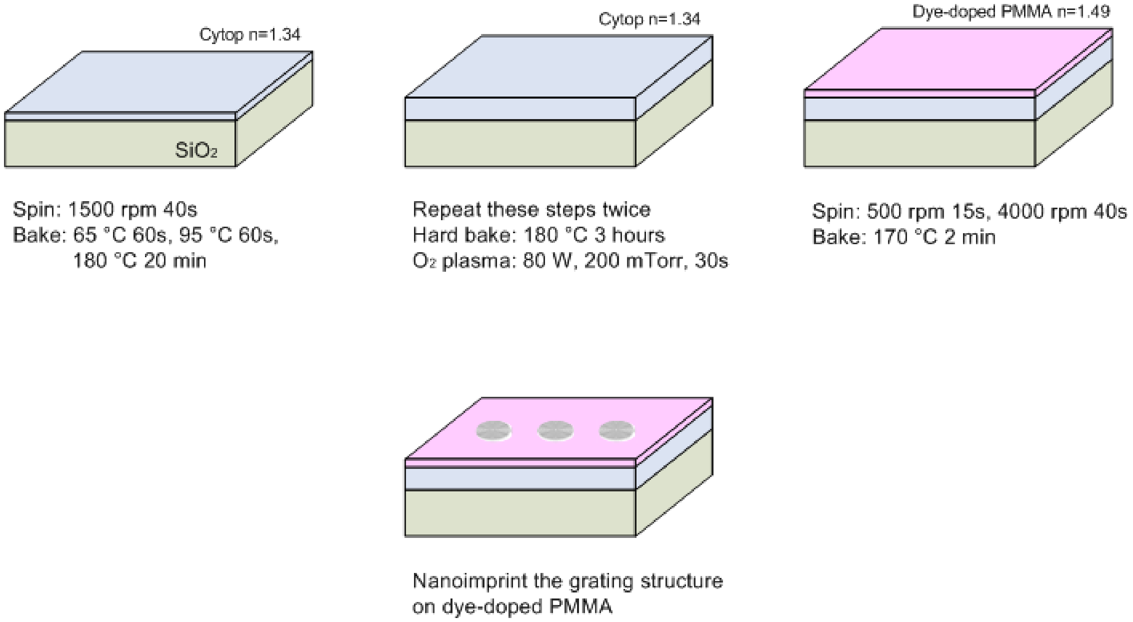

Spin: 1500 rpm 40s
Bake: 65 °C 60s, 95 °C 60s,
180 °C 20 min

Repeat these steps twice
Hard bake: 180 °C 3 hours
O_2 plasma: 80 W, 200 mTorr, 30s

Spin: 500 rpm 15s, 4000 rpm 40s
Bake: 170 °C 2 min

Nanoimprint the grating structure
on dye-doped PMMA

Figure 3.10: Summary of the Cytop and PMMA substrate preparation process.

3.4.3 Nanoimprint process

Nanoimprint lithography exploits the glass transition of polymers to achieve high-fidelity pattern transfer. However, degradation of the light emission efficiency of the organic materials during air exposure at high temperatures presents a challenge in nanoimprint lithography [30]. To solve this problem, a modified nanoimprint method is used to prevent this degradation of the dye-doped PMMA film by sealing the mold and the PMMA substrate into a curable polymer during the imprinting process.

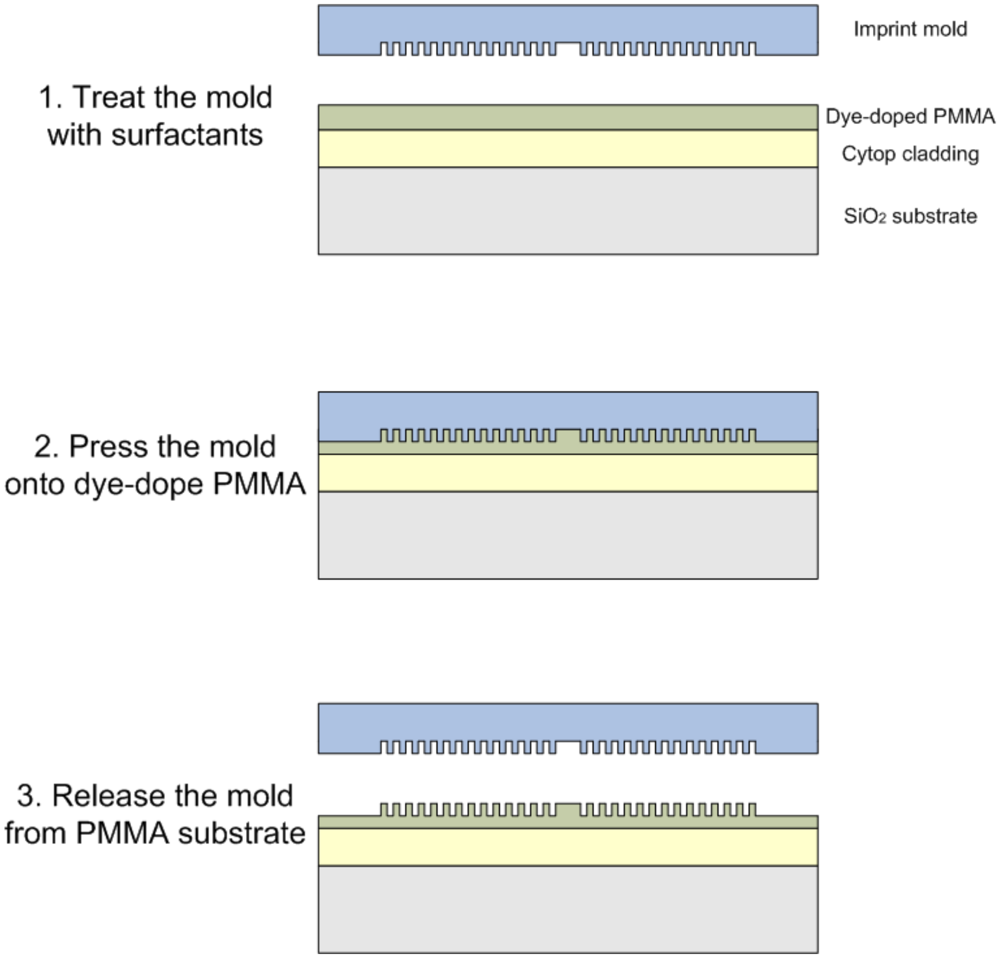

Figure 3.11: Schematic nanoimprint process of circular grating polymer dye laser.

During the nanoimprint process, a mold release reagent such as 1H,1H,2H,2H-perfluorodecyl-trichlorosilane (Alfa Aesar) was also deposited on the dye from the vapor phase to reduce the resist adhesion to the mold. Then, the mold was pressed into the PMMA film by using an automatic mounting press machine (Buehler SimpliMet 1000) at a temperature of 150 °C (above PMMA's glass transition temperature) and a pressure of 1200 psi. After sample cooling, the mold could be easily separated from the patterned polymer laser chip. The nanoimprint process is schematized in Figure. 3.11.

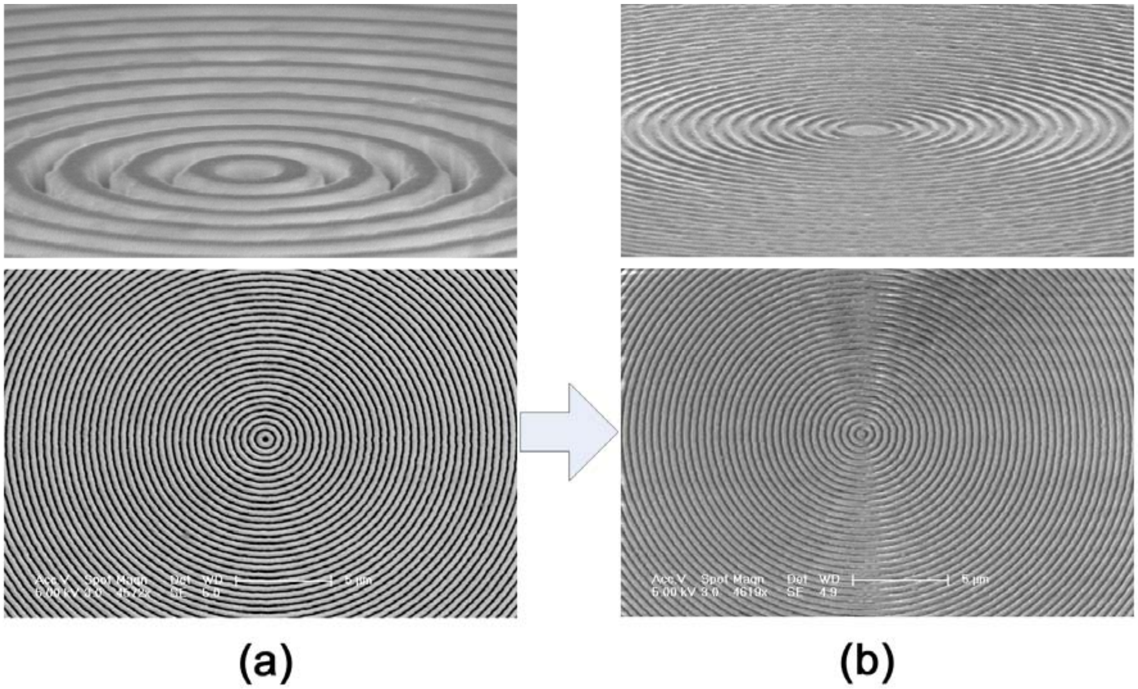

Figure 3.12: SEM images of (a) the SiO_2 mold and (b) the imprinted PMMA film.

Fig. 3.12 shows the SEM images of the mold and the imprinted PMMA. From these pictures, we can observe that the structure on the SiO_2 mold is faithfully replicated on the PMMA substrate surface with high resolution. Photoluminescence spectra confirm that there is no degradation of the luminescence performance of the polymer.

3.5 Results and discussion

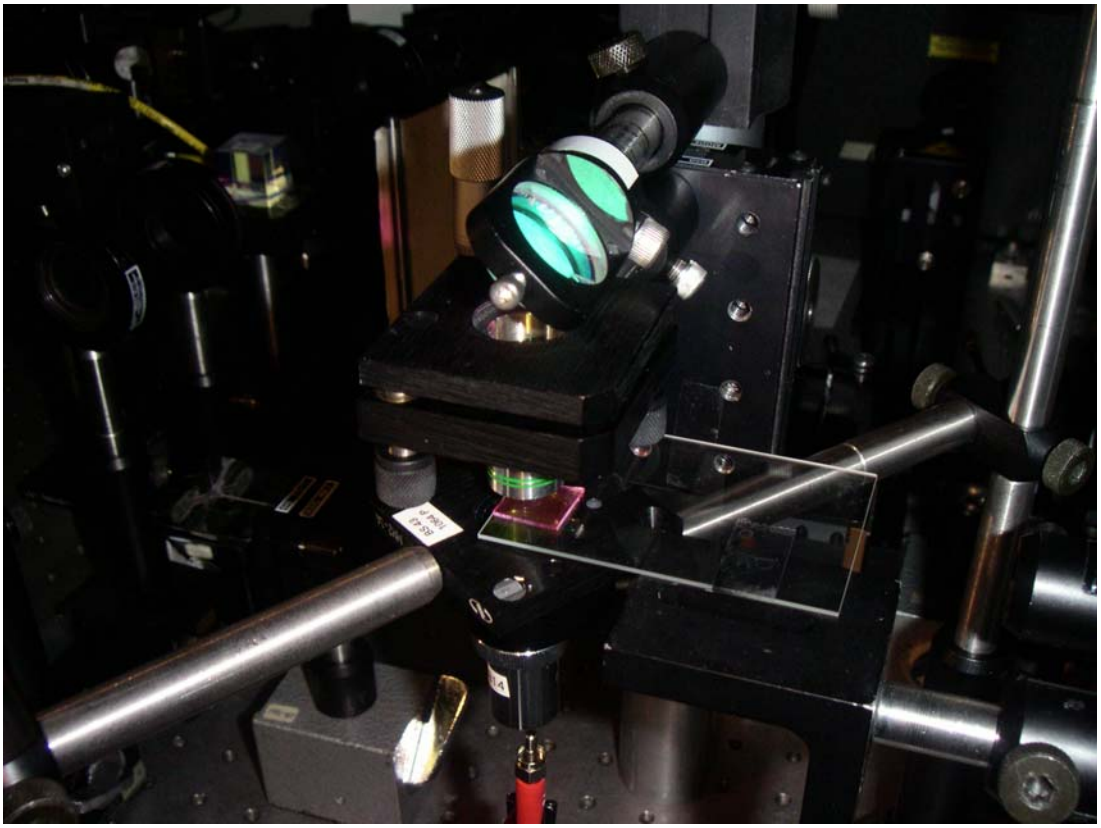

Figure 3.13: Measurement setup for polymer dye laser device.

The polymer laser chip was optically pumped with 6 ns Q-switched Nd:YAG laser pulses at 532 nm wavelength, focused through a 20X objective to the top side of the chip. A 10X microscope objective was used to collect the emission from the bottom side of the chip and deliver it to a fiber coupled CCD-array-based spectrometer with 0.1 nm resolution (Ocean Optics HR4000). The measurement setup is shown in Fig. 3.13.

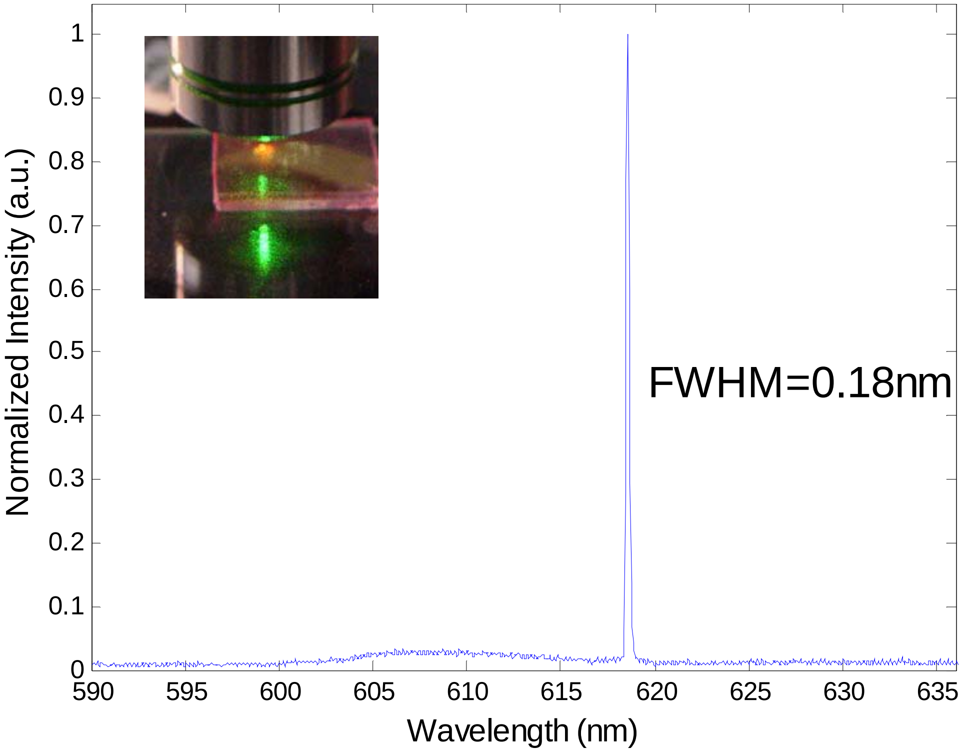

Figure 3.14: Nanoimprinted circular grating DFB dye laser spectrum. The measured linewidth is 0.18 nm. Inset: Polymer laser chip excited by Nd:YAG 532 nm laser pulse.

A typical single-frequency lasing spectrum is shown in Fig. 3.14. The lasing wavelength is 618.52 nm, and the measured linewidth is 0.18 nm. Lasing occurs near the Bragg resonance, determined by the equation $m\lambda_{Bragg} = 2n_{eff}\Lambda$, where $m = 2$ is the order of diffraction, n_{eff} is the effective refractive index of the propagation mode, and Λ is the grating period. The linewidth near threshold is measured as 0.20 nm, which results in a cavity quality factor (Q) of over 3000.

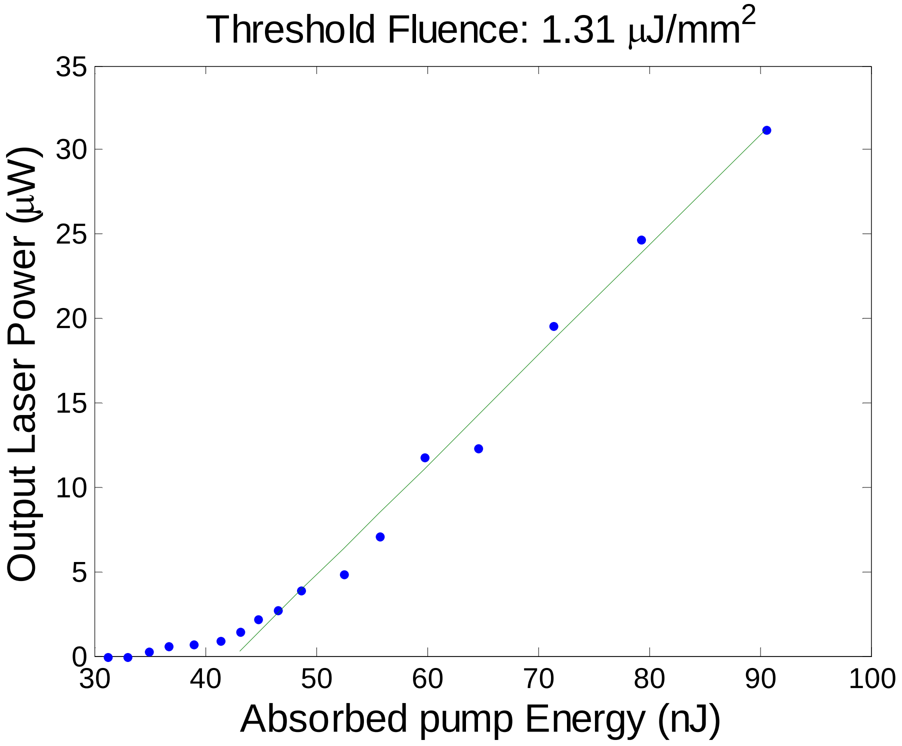

Figure 3.15: The output laser power vs. the absorbed pump energy curve. The threshold pump fluence is 1.31 μJ/mm^2.

Fig. 3.15 shows the variation of the output laser power as a function of absorbed pump energy. With the absorbed threshold energy of 41.3 nJ, the threshold pump fluence is estimated to be 1.31 μJ/mm^2. This pump intensity is well within the reach of commercial high power blue laser diodes (LDs), enabling a self-contained LD pumped device. The polymer laser is pumped from the surface of the chip and the lasing emission is collected from the back side of the chip. The transparency of the substrate, the size and geometry of the laser cavity, and the low threshold match well with the output beams of high power LED and LD. Therefore the replication-molded ring geometry represents a very promising structure for the construction of compact LED or LD pumped portable dye lasers.

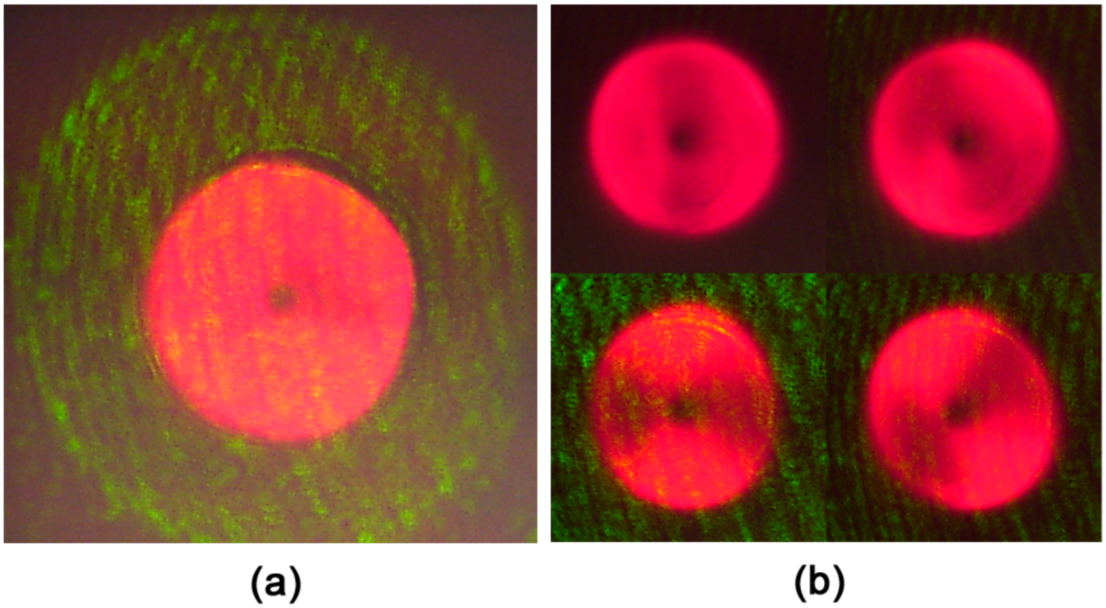

Figure 3.16: (a) Far-field image of the emission pattern recorded by a CCD camera. (b) Circular grating DFB laser far-field radiation patterns through a linear polarizer with different orientation angles. The laser emits an azimuthally polarized, well-confined circular beam.

Fig. 3.16 (a) represents the far-field image of the emission pattern recorded by a CCD camera, and Fig. 3.16 (b) shows the far-field radiation patterns of the laser passing through a linear polarizer with different orientation angles. The laser is expected to be azimuthally polarized [31], as illustrated in the polarization patterns. The azimuthal polarization also results in a zero electrical field (a dark spot) at the center of the laser [26]. In the lasing process, many spatial modes can be excited with their mode thresholds very close to each other [7]. The fundamental mode is normally the favored one, because higher order modes do not overlap well with the gain region.

We observe decreases in the laser emission with increasing exposure time. This result is consistent with previous studies on polymer DFB structures [32]. The lifetime of polymer dye laser can last over 106 shots of pump laser pulse, and if the characterization of the device is carried out under vacuum to inhibit photo-oxidation, the lifetime can be further extended [33]. Because of the low cost of materials and fabrication, replication molded devices are disposable and may not require a long lifetime. In the future, we plan to make an optofluidic version [34, 35] of the circular grating dye laser which allows us to constantly change the dye to increase the device lifetime and to tune the wavelength [36].

3.6 Summary

In summary, we have demonstrated a surface emitting polymer dye laser with a circular grating distributed feedback structure realized by nanoimprint lithography. We have achieved excitation thresholds as low as 1.31 $\mu J/mm^2$ and FWHM linewidths of 0.18 nm. The technique described here enables the fabrication of low cost, high quality and mass producible laser arrays, which may be deployed as compact and inexpensive coherent light sources for lab-on-a-chip applications such as sensing and spectroscopy. Future work will be focused on improving the laser cavity Q values with better electromagnetic design, optimizing the dye concentration, and fabricating smoother surfaces. The ultimate goal is to reduce the lasing threshold to enable the use of LEDs as integrated and inexpensive pump sources for on-chip polymer lasers.

Chapter 4

Optofluidic circular grating dye laser

4.1 Introduction

The field of optofluidics, which is the integration of optics and microfluidics, has attracted great interest for its novel implementation in biotechnology [37]. Among the new class of optofluidic devices, On-chip liquid dye lasers allow the integration of coherent light sources with other microfluidic and optical functionalities, and provide possibilities for building more complete “lab-on-a-chip” systems. These optically pumped devices consist of microfluidic channels with an embedded optical resonator, and a liquid laser dye is used as active gain medium.

There are many unique properties of the miniaturized liquid dye lasers in microfluidic systems. First, compared to solid-state dye lasers, the liquid gain medium in microfluidic dye lasers makes the changing of dye easier, which is very helpful for improving the lasing performance. For example, the photo-bleaching of the dye is significantly reduced by a regenerating flow of dye through the lasing cavity inside the microfluidic channel. Second, the microfluidic circuits include valves, and pumps allow the mixing of different solvents with dyes. Therefore, the tuning of lasing wavelength can be achieved by modifying the refractive index of the dye solution or changing the dye concentration. Third, the flexibility and versatility of microfluidic fabrication enables the large-scale integration of laser arrays in compact devices with more functionality. All these advantages make it possible to build on-chip tunable coherent light sources useful for many applications in biochemical analysis, such as laser-induced fluorescence and spectroscopy.

Distributed feedback (DFB) laser resonators have been proven to be particularly suitable for optofluidic devices because of their low threshold lasing operation features. A DFB microfluidic dye laser was first demonstrated by Balslev et al. [38] who used a high-order Bragg grating in an 8 μm thick polymer film to obtain feedback. Single-mode lasing with a threshold fluence of approximately 20 $\mu J/mm^2$ was obtained due to mode selective losses in the multimode structure where light was not guided in the fluidic segments. Li et al. [34] realized a 15th-order DFB laser using low refractive index poly(dimethylsiloxane) (PDMS) and a high refractive index liquid core. A record low lasing threshold fluence of 8 $\mu J/mm^2$ was obtained. Gersborg-Hansen et al. realized a third-order distributed feedback laser fabricated in a poly(methylmethacrylate) (PMMA) integrated microfluidic device [35].

The tuning of lasing wavelength is also an attractive feature of optofluidic dye lasers. Galas et al. have demonstrated the integration of PDMS-based microfluidic circuits with microfluidic dye lasers to tune the laser wavelength [39]. Tunable output in microfluidic dye laser by changing index and concentration was also investigated by Gersborg-Hansen et al. [36]. Li et al. reported a mechanically tunable dye laser [40]. Vezenov et al. fabricated an edge emitting dye laser in PDMS based on a liquid-liquid (L^2) waveguide and studied its lasing tuning range [41].

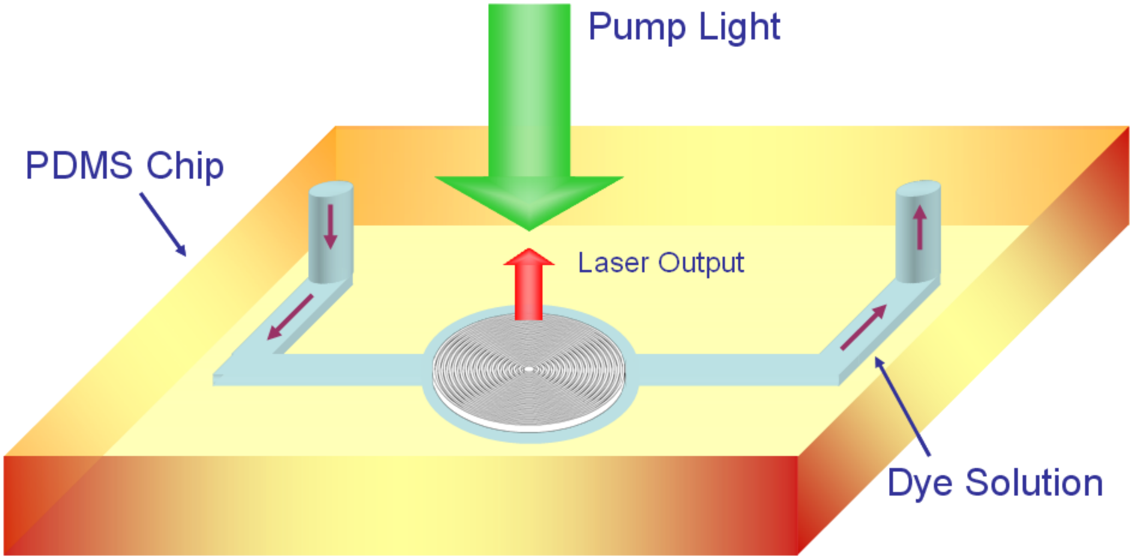

Figure 4.1: Schematic diagram of an optofluidic circular grating dye laser chip.

In this chapter, we present a surface emitting optofluidic dye laser with circular grating distributed feedback (DFB) structure. We choose the circular grating DFB structure as the laser cavity to achieve low-threshold, high-efficiency operation, and vertical emission out of the device plane. The schematic diagram of our microfluidic circular grating dye laser is shown in Fig. 4.1. The laser chip is a hybrid microfluidic device made of poly(dimethylsiloxane) (PDMS) and perfluoropolyether (PFPE). A microfluidic channel with the circular grating structures embedded is filled with dye solutions. The gain medium is a 2 mM solution of Rhodamine 6G in a benzyl alcohol and methanol mixture with refractive index of 1.53. The PDMS forms the microfluidic channel and serves as the upper cladding of the cavity. The lower cladding material is PFPE, which also forms the circular grating that provides the feedback necessary for the laser action.

4.2 Materials

4.2.1 PDMS

The most commonly used polymer in soft lithography to make microfluidic devices is poly(dimethylsiloxane) (PDMS). PDMS is a silicone elastomer and has many advantages for making microfluidic devices. It is optical transparent in a broad range of spectra (240 nm–1100 nm). It can be used to fabricate nanoscale structures by simple replica molding technique because of its high elasticity and intrinsically low adhesion properties [42], and it has easy and superior bonding property to many materials [43]. Also PDMS is low cost (~ $20/kg), biocompatible, and safe to use [44].

The PDMS replication molding process is usually composed of three steps: (1) pouring or spin coating of PDMS prepolymer onto the structured master, (2) thermal curing to cross-link the polymer, (3) peeling-off of cured PDMS from the master. The structured PDMS can be utilized in a further process through bonding with other plates, such as silicon, glass, plain PDMS, and other structured PDMS.

Soft lithography is currently the most useful technique for patterning 500 nm or larger features [45]. However, the replication resolution is limited by the most commonly used PDMS formulation (Sylgard 184, Dow Corning) due to several reasons. First, its low Young's modulus (~ 1.5 Mpa) caused high aspect ratio features to deform or collapse [46]. Second, its surface energy (~ 22–25 mN m^{-1}) is not low enough for fabrication that requires high fidelity [47]. Third, its poor solvent resistance leads to a swelling issue when exposed to most organic solvents [48].

Several variants of PDMS such as h-PDMS [49] and hν-PDMS [50], have been reported to improve the resolution and fidelity in soft lithography. The h-PDMS with short cross-linkers has a relatively high modulus (~ 9 MPa), but its elongation at break is much lower than that of 184-PDMS. It can be used effectively by a composite bilayer patterning method. The combination of a thin layer of h-PDMS with a thick backing of 184-PDMS successfully improved the replication resolution down to 50 nm [46]. The hν-PDMS is a photocurable version of PDMS with a modulus of ~ 4 MPa; the photopatterning in nanostructure fabrication prevents the distortion during the thermal curing process. hν-PDMS is easier to handle since its elongation at break is much higher than that of h-PDMS, and it can also achieve the patterning of high aspect ratio, submicron features.

There are also other ways to improve the resolution of replication molding for 184-PDMS. The use of 184-PDMS as high-resolution mold material was reported by Bender et al. [51], the resulting PDMS reached a modulus of ~ 3 MPa and a surface hardness of 50 Shore A. The resolution can be further increased by a pressure-assisted molding [52] or a diluted PDMS material [53]. However, these processes require baking of PDMS at 130 °C, which fully cures the PDMS and prevents its further bonding with another PDMS layer, and therefore is not advantageous for our optofluidic dye laser device fabrication.

4.2.2 PFPE

The photocurable perfluoropolyether (PFPE) has been reported by DeSimone et al. as an alternative material for microfluidic devices [54] and nanoimprint lithography [47]. This (PFPE-DMA) has a modulus of ~ 4 MPa and a very low surface energy (~12 mN m^{-1}). More importantly, this material is solvent resistant and chemically robust to most organic solvents. These characteristics are very attractive for the fabrication of microfluidic devices that require higher fidelity pattering and more functionality. The main problem with the PFPE is the fact that it is hard to bond two layers of PFPE. By adding different terminal chemical groups to the layers that tend to react with each other, some improvement was achieved in the bonding. However, the synthesis of this fluoropolymer is very complicated and the yield is usually low, the small quantities of PFPE have prevented us from extensive testing of this polymer.

The use of a commercially available form of PFPE (CN4000, Sartomer Company, Inc., MW=1000 g mol^{-1}) is reported by Trong et al. [55]. This PFPE is a fluorinated acrylate oligomer which has the backbone of fluorinated polyether with acryloxy (CH_2=CH−COO−) as ending functional groups instead of methacryloxy groups in the reported PFPE-DMA. This material is cross-linked under UV illumination to form an elastomer with a high modulus (10.5 MPa), a low surface energy (18.5 mN m^{-1}), and a low refractive index (1.341).

With the higher young's modulus of the PFPE, we can achieve replication of higher resolution and higher aspect ratio features, which give rise to the optical confinement of the grating structure. The refractive index of PFPE (n=1.341) is even lower than that of PDMS (n=1.406), which makes it more suitable to serve as a cladding material for our laser device.

However, the bonding of PFPE remains a problem. Experiments have been conducted to test the bonding by partially curing the material, but the results are not very promising. Also the PFPE is too brittle to punch holes through, unlike PDMS. All these disadvantages of PFPE prevent it from being used in simple and conventional multilayer soft lithography to make microfluidic devices.

To successfully fabricate microfluidic channels with the sub-200 nm laser cavity structures embedded, we not only expect the soft lithography material to have high replication resolution, but also require a superior bonding property of the material. Therefore, our optofluidic dye laser is composed of two layers, a stiff layer (PFPE) supported by a flexible layer (PDMS). This composite bilayer patterning method combines the most attractive features of both materials, and it is very useful in defining functional microfluidic devices with nano-scale optical structures embedded.

4.2.3 Laser dye and solvents

The organic laser dye we use in the laser device is Rhodamine 6G, which is also known as Rhodamine 590 Chloride (Exciton). The molecule structure of Rhodamine 6G is depicted in Fig. 4.2. Use of this dye as amplifying medium in lasers is very common due to its large quantum efficiency and relatively long lifetime against bleaching. It is extensively used in tunable lasers in the visible wavelength for many applications, such as spectroscopy. There are other dyes in the Rhodamine family with different wavelength, such as Rhodamine B and Rhodamine 101. We chose Rhodamine 6G to match its absorption peak with the cavity resonant frequency. The stimulated singlet state absorption and emission cross sections are illustrated in Fig. 4.3.

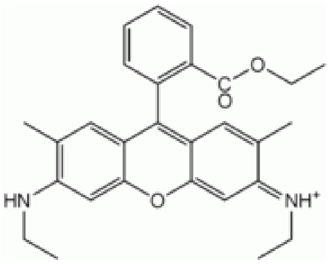

Figure 4.2: Rhodamine 6G molecule structure.

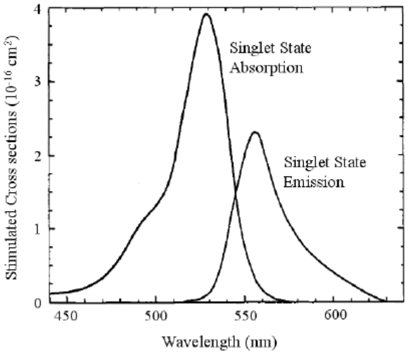

Figure 4.3: Cross sections of stimulated singlet state absorption and emission for Rhodamine 6G in ethanol.

Because of the swelling issue of PDMS for most organic solvents [48], the choice of the solvents for the dye molecules is very limited. The commonly used dye laser solvents which are also compatible with PDMS are listed below: methanol, water, ethanol, ethylene glycol, glycerol, dimethyl sulfoxide (DMSO), and benzyl alcohol. Table 4.1 shows the refractive indices of these organic solvents. The available refractive index range is from 1.33 to 1.54. To obtain the highest refractive index contrast, we used a 20:1 mixture of benzyl alcohol and methanol which has a refractive index close to 1.53. The addition of methanol is mainly to assist the dissolving of the dye molecules. The PDMS-compatible solvents can be mixed to produce laser dye solvents with different refractive indices, thus providing a convenient way to achieve wavelength tuning in optofluidic devices.

Table 4.1: Refractive indices of PDMS-compatible solvents

Solvent	Refractive Index*
Methanol	1.33
DI Water	1.333
Ethanol	1.36
Ethylene Glycol	1.43
Glycerol	1.473
DMSO	1.478
Benzyl Alcohol	1.54

*At room temperature, sodium D line 589.3 nm

4.3 Laser cavity design

4.3.1 Circular grating distributed feedback structure

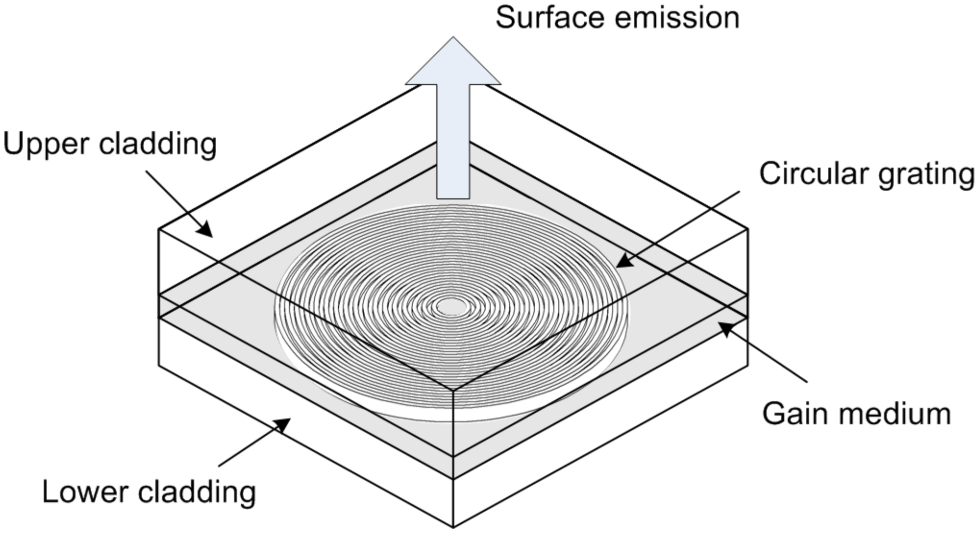

Figure 4.4: General design of an optofluidic circular grating DFB dye laser cavity.

The circular grating distributed feedback (DFB) structure used in our optofluidic devices is basically the same as the one in the nanoimprinted solid-state dye lasers. Instead of doping the dye molecules in the resonator structure, laser dye is dissolved in the organic solvents. Fig. 4.4 shows a general design of an optofluidic circular grating DFB dye laser cavity. The upper cladding and the lower cladding is PDMS (n=1.406) and PFPE (n=1.341), respectively.

The circular grating structure provides a natural 2-D extension of the basic DFB structure. The corrugations in the grating structure provide both distributed feedback and output coupling of the guided optical mode. Theoretical analysis of circular grating lasers predicts that only the radial propagating components define the modes in the circularly symmetric grating. Second-order gratings are used to obtain surface emission, because the first-order Bragg reflection from a second-order grating can phase match radially propagating waves to vertically propagating plane waves, as illustrated in Fig. 4.5.

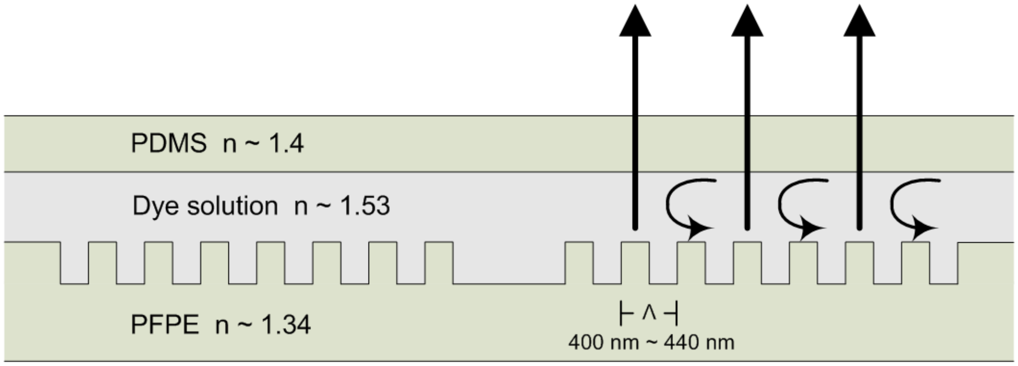

Figure 4.5: Illustration of the Bragg diffraction in the second-order circular grating. First-order Bragg reflection induces coupling to vertical propagating waves, and second-order Bragg reflection leads to in-plane feedback.

The design parameters of the circular gratings fabricated are selected based on electromagnetic mode calculations and experimental results. Grating periods varying from 400 nm to 440 nm are chosen to match the second-order Bragg condition. We use a deeper grating trench to compensate for the low refractive index contrast between the dye solution and the cladding. The 600 nm groove depth is defined to ensure maximum confinement, whereas the 200 μm overall diameter of the circular grating and the 50% duty cycle are used to reach the maximum coupling strength.

4.3.2 Flow channel design

In the optofluidic laser chip, the microfluidic channel filled with dye solution serves as the optical waveguide for the laser operation. We choose the waveguide to be 1.6 μm high, and the flow channel width is 12 μm. The waveguide's thickness is larger than that of the solid-state circular grating dye laser, but it can still effectively confine the light within the gain medium.

Due to the innate softness of PDMS, channels with aspect ratio higher than 20:1 tend to collapse. The overall diameter of the circular grating is 200 μm, so the height of the channel on top of the grating should be at least 10 μm. However, such a high channel cannot form an effective waveguide, since the excess dye in the microfluidic channel creates large background noise during optical pumping.

There are two methods to solve this problem. The first one is making a control valve on top of the grating area by multilayer soft lithography developed by Steven Quake's group and Axel Scherer's group at Caltech [56]. The principle of the two-layered microfluidic circuit is shown in Fig. 4.6. The push-down valve is assumed to control the thickness of the flow channel by applying pressure. However, the pressure controlling leads to uneven surface on top of the flow channel and may not accurately maintain the desired thickness of the waveguide.

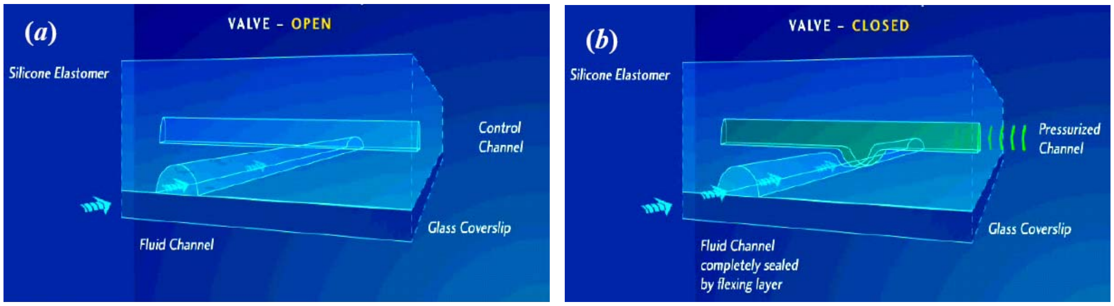

Figure 4.6: PDMS microvalves (push-down version). Source: www.fluidigm.com

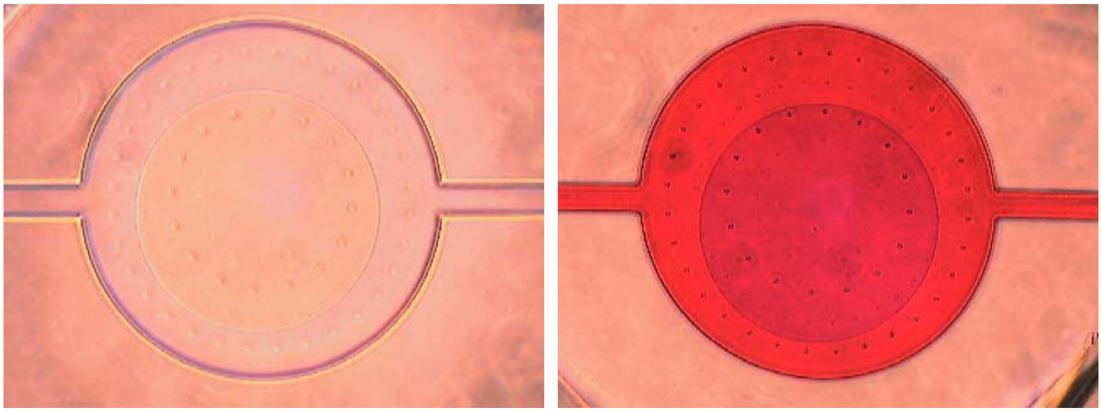

Figure 4.7: Microscope graph of microfluidic flow channel. Left: flow channel covering the grating area. Right: flow channel filled with dye solution.

The other way to make a 1.6 μm high channel over a 200 μm diameter area is more simple and straightforward. Support pillars were fabricated within flow channels to avoid bowing of the extremely wide PDMS channels. Fig. 4.7 shows a microscope graph of microfluidic flow channel with little posts (5 μm diameter) fabricated inside. The spacing between posts is around 30 μm to ensure the proper aspect ratio in between posts. Although the channel aspect ratio (1.6:200) highly exceeds the allowed range (1:20), the flow channel does not collapse and can be filled with dye solution. Since the height of the flow channel is relatively small, the flow rate of the dye solution in the channel is reduced, but it is still enough for the circulation of dye during lasing operation.

4.4 Fabrication process

4.4.1 Mold fabrication

To define our circular grating structure, silicon dioxide (SiO_2) was used as the mold material. In order to obtain a deep, steep-sided grating profile, we chose a deep reactive ion etching (DRIE) process to etch SiO_2. DRIE is a highly anisotropic etching process for creating deep trenches in substrates with relatively high aspect ratio. The DRIE etching in SiO_2 requires the use of higher selective material, i.e., the Cr, as the etching mask.

The original wafer was 1 μm of SiO_2 on top of Si substrate. First, 20 nm of Cr was evaporated on the wafer using a thermal evaporator, then 2% 950K PMMA was spun on top of the Cr layer for 1 min at 3000 rpm and baked for 15 min at 170 °C, which formed a 100 nm thick resist layer. The grating pattern was defined by electron beam lithography on a LEICA EBPG 5000+ e-beam writer at 100 keV and 900 $\mu C/cm^2$ with proximity correction. Development of patterned PMMA film was carried out in a 1:3 MIBK:IPA (methyl isobutyl ketone and isopropanol alcohol) solution for 1 min. Next, the wafer was immersed in chromium etchant (CR-7, Cyantek) for 10 s to remove the Cr underneath the exposed PMMA pattern. The remaining PMMA was removed by methylene chloride.

The pattern was subsequently transferred from Cr into SiO_2 substrate via deep reactive ion etching (DRIE) using C_4F_8. The SiO_2 etching rate in the C_4F_8 DRIE process is 5 nm per second. The schematic fabrication procedure for the soft lithography hard mold is illustrated in Fig. 4.8.

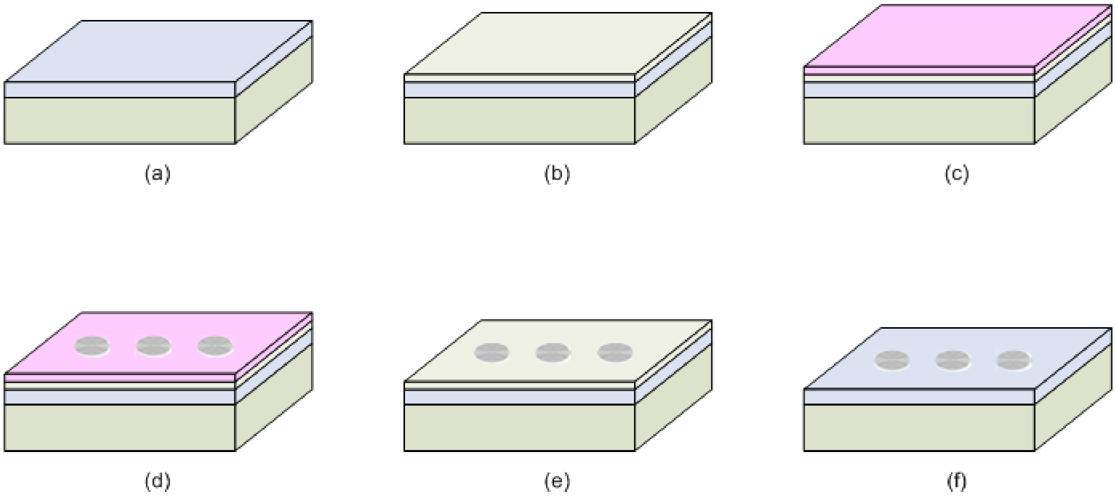

Figure 4.8: Schematic fabrication procedure for the circular grating hard mold. (a) The original wafer with 1 μm SiO_2 on top of Si substrate. (b) Cr is evaporated on the sample. (c) PMMA is spun on top of the Cr for subsequent e-beam lithography steps. (d) The PMMA is exposed by e-beam, and the circular grating pattern is completely transferred into PMMA after developing the exposed resist. (e) The Cr underneath the exposed pattern is removed by wet etch, and the remaining PMMA is also removed. (f) The pattern is transferred into the SiO_2 via DRIE etch.

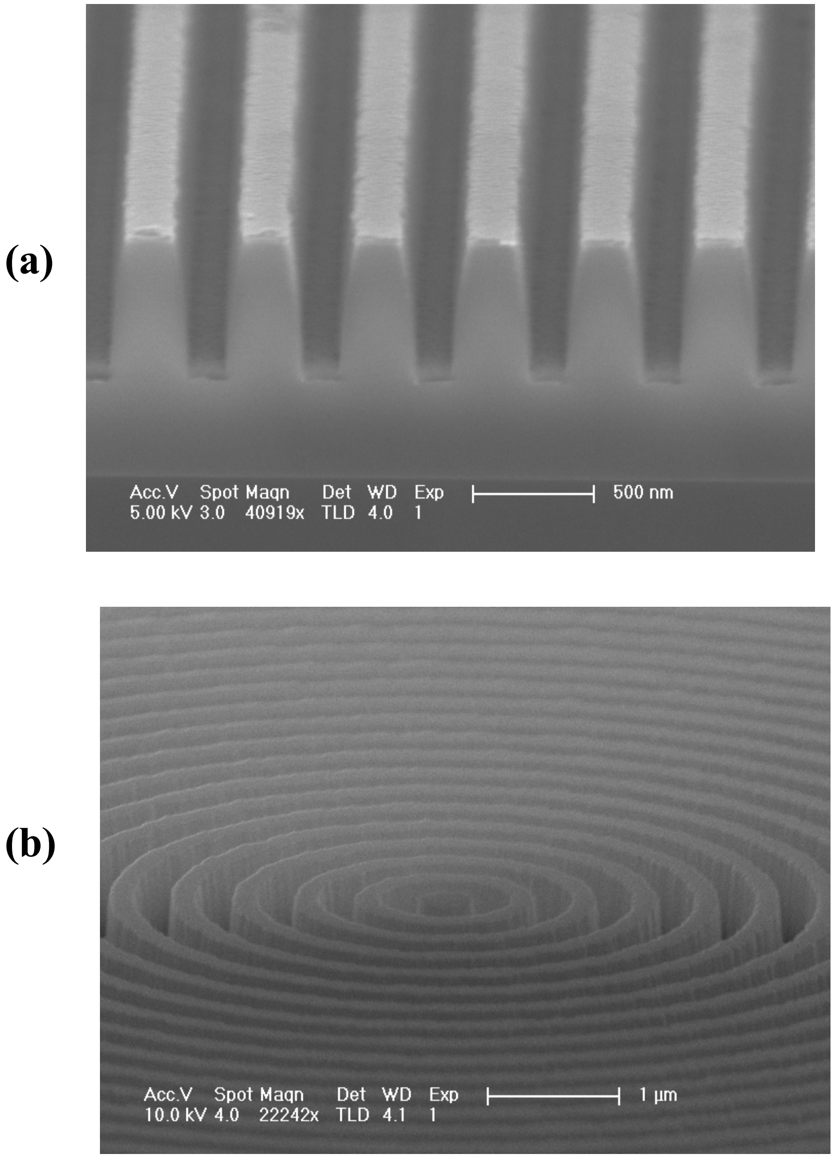

Figure 4.9: The SEM images of the cross section of etched SiO_2 gratings. (a) A cut-away view of the gratings. (b) Deeply etched trenches in the circular grating structure.

The SEM image of the cross section of etched SiO_2 gratings is shown in Fig. 4.9. (a) is a cut-away view of the gratings indicating an excellent anisotropic profile with a depth of 600 nm; (b) shows the deeply etched trenches with vertical and smooth side walls in the circular grating structure. The SEM images of both the top view and the angled view of an etched SiO_2 mold of circular grating are shown in Fig. 4.10.

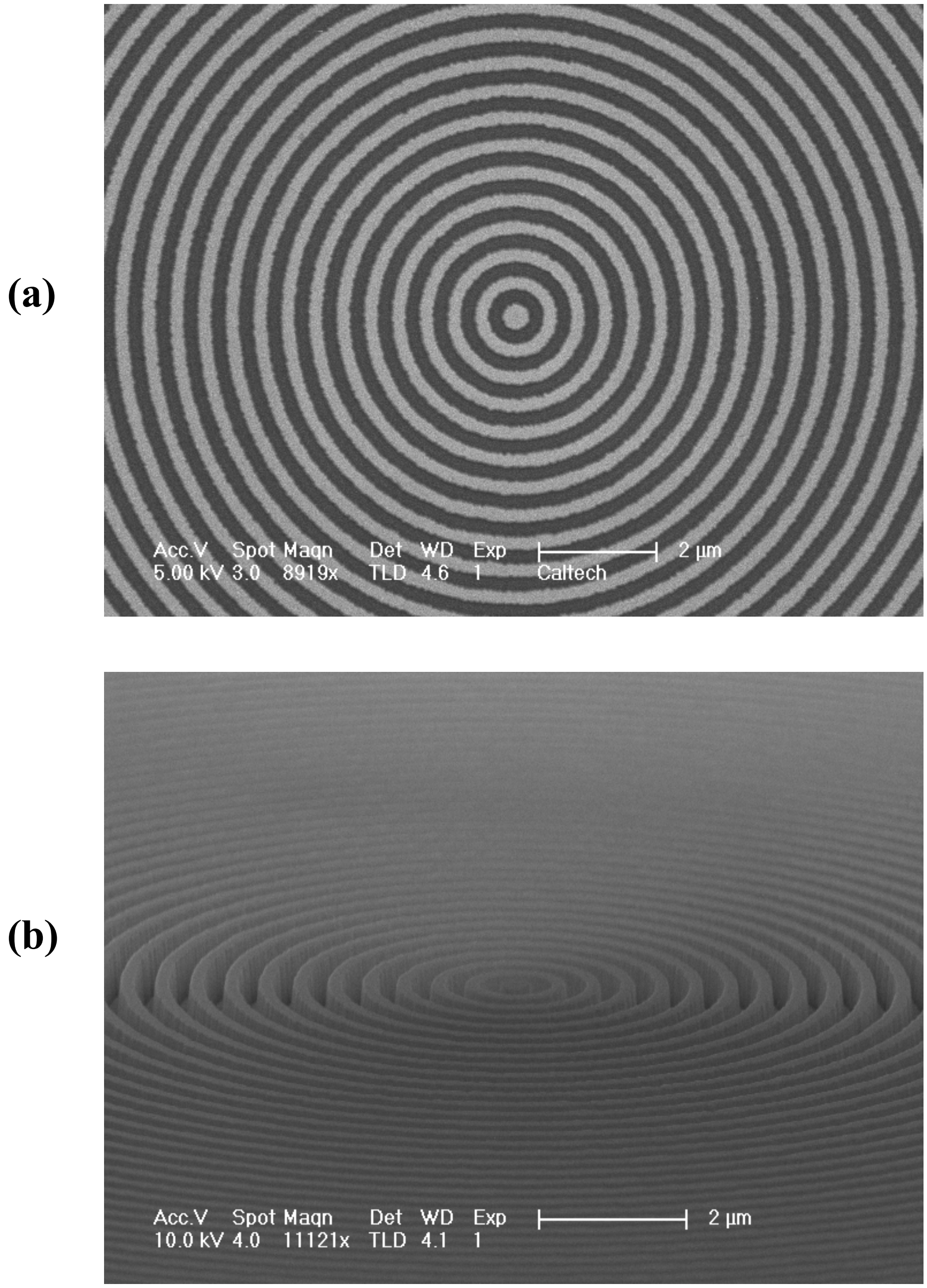

Figure 4.10: SEM images of (a) the top view and (b) the angled view of the SiO_2 mold.

4.4.2 Laser chip fabrication

The optofluidic dye laser device is fabricated by conventional multilayer soft lithography techniques. The chip consists of two layers, the grating layer and the flow layer. The grating layer is made of PFPE supported by a flexible PDMS backbone, and it is bonded to the thin layer of PDMS with flow channels inside.

In our experiments, we used a commercially available form of PFPE. It is a 1 wt% mixture of a photoinitiator, Darocurr 4265 (Ciba Specialty Chemicals), and a fluorinated acrylate oligomer, CN4000 (Sartomer Company, Inc., MW=1000 g mol^{-1}). Mixing the two chemicals for 2 hours followed by filtering the mixture through a 0.22 μm syringe filter produced a photocurable liquid resin. Exposing the material the under UV (365 nm) for 1 hour cured the material.

The fabrication of the hybrid material laser chip started with aligning a thin PDMS layer on top of the grating mold to cover most of the mold except the grating areas. Then the PFPE was spincoated (2000 rpm for 1 min) on the mold, followed by UV exposure for 1 hour to cure the material. After peeling of the thin PDMS layer, a new PDMS prepolymer (5:1 RTV A:B) was poured onto the PFPE layer and degassed in a vacuum chamber for 30 min, then the prepolymer was partially cured at 80 °C for 30 min. This process formed a support layer for the composite PFPE/PDMS structure. The PFPE/PDMS layer was peeled from the grating mold and bonded to another PDMS layer with the flow channel. Finally, the device was baked at 80 °C for 3 hours to ensure bonding between the two layers. The bonding between PFPE and PDMS is not very strong, but the adhesion is sufficient for the laser chip operation. The fabrication process of the hybrid PFPE/PDMS laser chip is illustrated in Fig. 4.11.

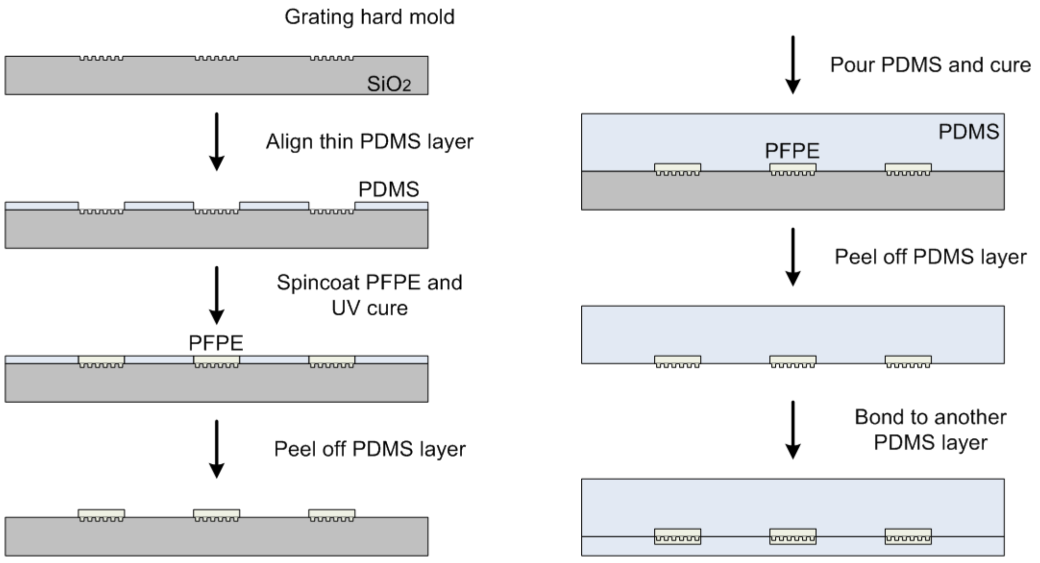

Figure 4.11: Fabrication process of the hybrid PFPE/PDMS laser chip.

The SEM images of SiO_2 mold with circular grating structure and its replica in PFPE are shown in Fig. 4.12. The image of PFPE was obtained using an environmental SEM (ESEM) operating at a water vapor pressure of 0.98 Torr in the chamber, and an accelerating potential of 5 kV, in order to mitigate charging effects from the nonconductive polymer samples. From the ESEM image we can see that the structure on the SiO_2 mold is faithfully replicated on the PFPE with high resolution, and there is no lateral collapse between the grating lines even with aspect ratios above 3:1.

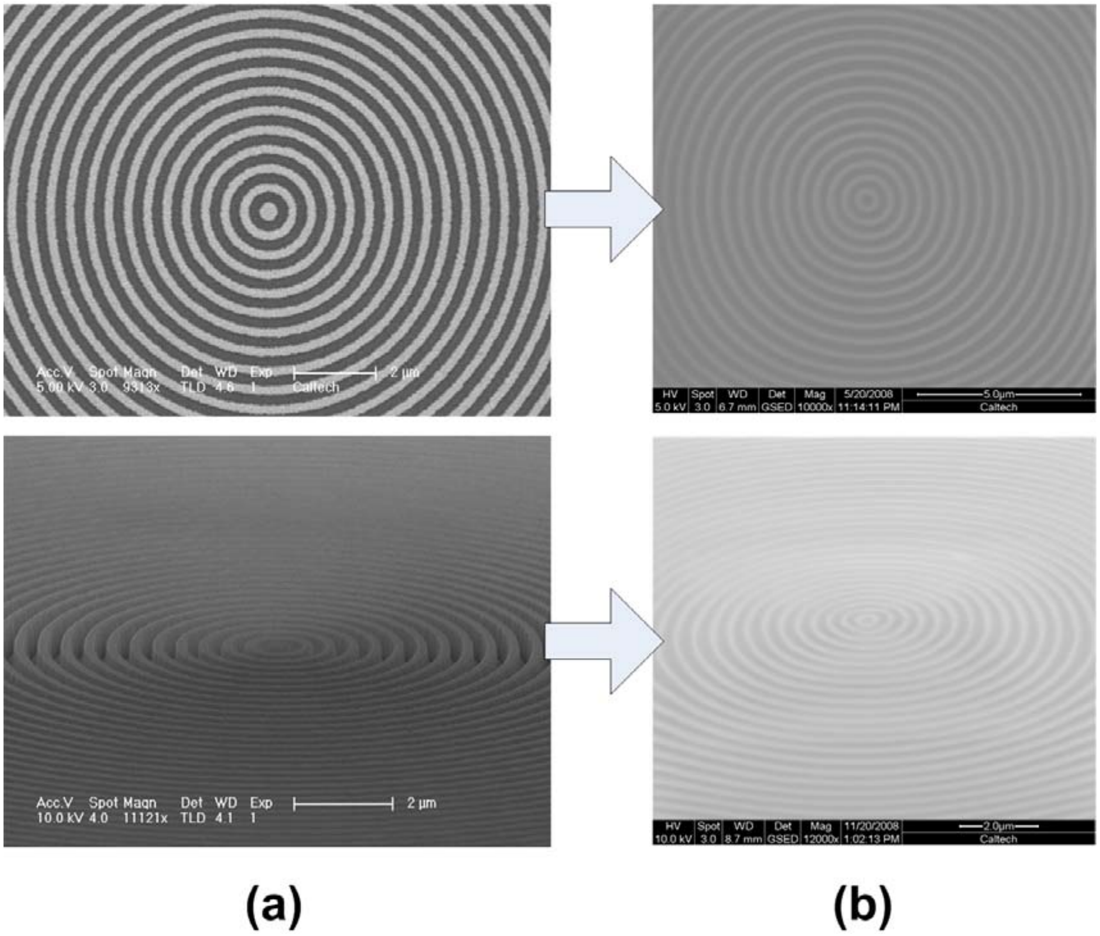

Figure 4.12: (a) SEM images of SiO_2 mold. (b) ESEM images of PFPE replica.

4.5 Results and discussion

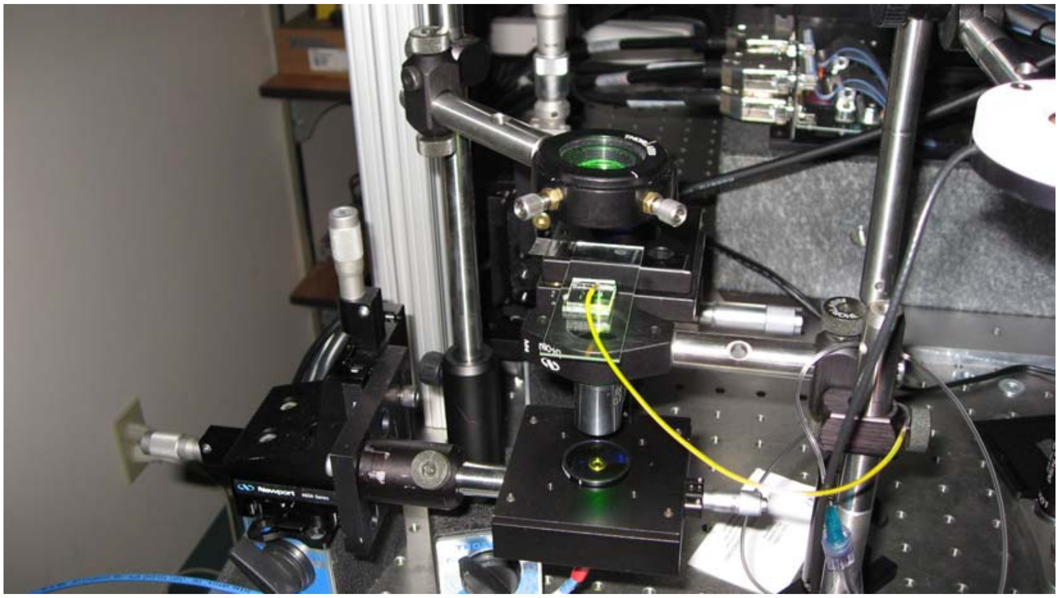

Figure 4.13: Measurement setup of optofluidic dye laser chip.

The optofluidic dye laser chip was optically pumped with 6 ns Q-switched Nd:YAG laser pulses at 532 nm wavelength, focused through a 20X lens to the top side of the chip. A 10X microscope objective was used to collect the emission from the bottom side of the chip and deliver it to a fiber coupled CCD-array based spectrometer with 0.3 nm resolution (Ocean Optics USB2000). The fluidic control tubing connected to a pressure source was used to circulate the dye solution in the flow channel. The measurement setup of optofluidic dye laser chip is shown in Fig. 4.13.

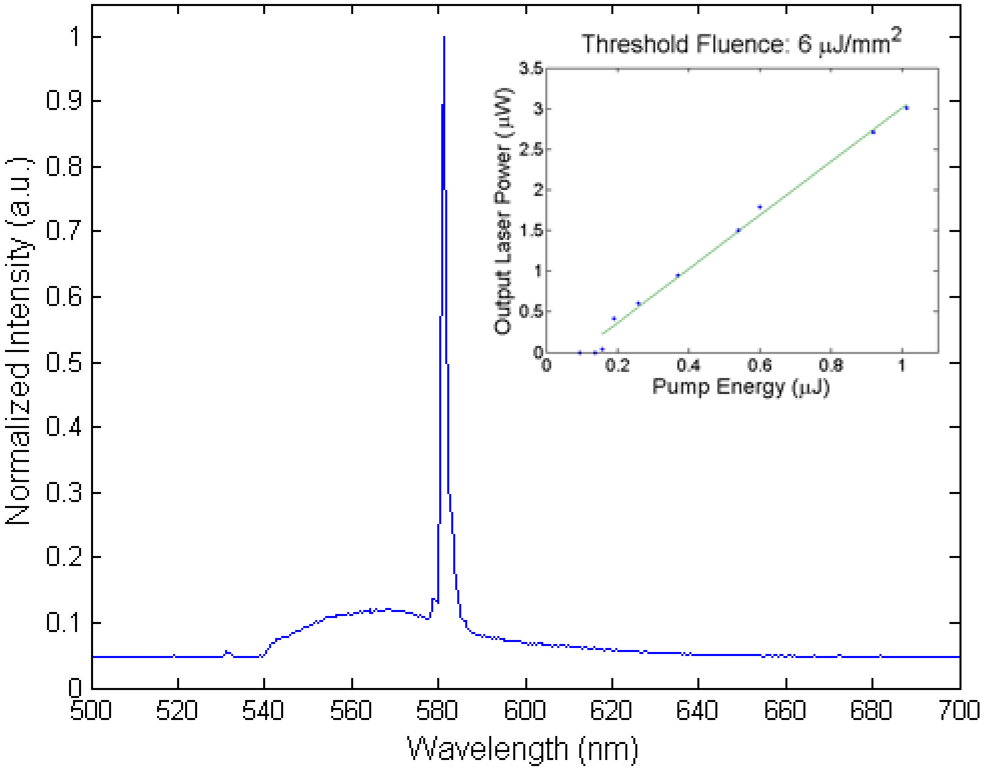

Figure 4.14: Optofluidic circular grating DFB dye laser spectrum. Inset: The output laser power vs. the pump energy curve.

A typical single-frequency laser spectrum, measured from one of the circular grating dye lasers, is shown in Fig. 4.14. The lasing wavelength for this device is 581.13 nm, and lasing occurs near the Bragg resonance, determined by the equation $m\lambda_{Bragg} = 2n_{eff}\Lambda$, where $m = 2$ is the order of diffraction, n_{eff} is the effective refractive index of the propagation mode, and Λ is the grating period. In this laser, with the grating period of 410 nm, the n_{eff} is 1.42, which is close to the effective index simulation result of the waveguide. The laser is azimuthally polarized, and only the fundamental mode exhibits here because it overlaps most efficiently with the gain spectrum of Rhodamine. The optofluidic dye laser is pumped from the surface of the chip, and the lasing emission is collected from the back side of the chip.

The inset shows the variation of the output laser power as a function of pump energy, the threshold pump fluence is estimated to be 6 μJ/mm^2. This relatively low pump threshold is within the reach of high power laser diodes operating in pulsed mode. In order to realize light-emitting diode pumped optofluidic dye lasers, however, further reduction of the dye laser threshold is required. The small size and surface emitting geometry of the laser cavity also provide a simple but efficient scheme to construct laser arrays with geometrically controlled emission wavelengths, pumped with a single wavelength source.

The decrease in the laser emission with increasing exposure time was observed during laser operation. Since the typical photo-bleaching time of Rh6G is ~ 50 ms under pump intensities required for laser threshold (~ 100 kW/cm^2), circulating the dye solution with an appropriate flow rate prevents the dye molecules from photo-bleaching under pulse operation. Therefore, the optofluidic version of the circular grating dye laser allows us to constantly change the dye to increase the device lifetime.

Due to the small size (~ 200 μm) of the laser geometry, it is convenient to construct laser arrays with different grating periods in the same chip. The whole chip can be excited simultaneously to achieve parallel operation of the laser arrays. The grating periods vary from 400 nm to 440 nm with a spacing of 5 nm so that the resulting lasing wavelengths are within the gain spectrum of the laser dye Rhodamine 6G. Different laser dyes with separated absorption peaks can also be introduced in multiple flow channels to expand the emission spectral range.

The microfluidic compatibility of the laser chip also suggests that we can achieve wavelength tuning by mixing two solvents with different refractive indices. The mixing and delivery of dye solutions can be implemented in a microfluidic chip using pneumatic valves and pumps.

4.6 Summary

In this chapter, we demonstrate a second-order circular grating distributed feedback structure embedded in an optofluidic dye laser system. We obtain surface emitting single frequency lasing at a relatively low pumping threshold. To construct these circular grating dye lasers, we have developed a hybrid PFPE/PDMS soft lithography technique that enables the fabrication of low cost, disposable, and high quality dye laser arrays. This polymer heterostructure also provides a convenient method for fabricating optofluidic device with nano-scale optical structures embedded within traditional PDMS flow channels. Parallel lasing operation and automatic wavelength tuning can also be achieved using the microfluidic circuit. The construction of compact and inexpensive coherent light sources fully integrated with microfluidics provides an efficient approach to realize complete “lab-on-a-chip” systems.

Chapter 5

Microfluidic device as a platform for single cell biochemical analysis

5.1 Introduction

5.1.1 Microfluidic device as a platform for biochemical analysis

Over the decade of its existence, the rapid development of polydimethylsiloxane (PDMS)-based microfluidics and its components have found many useful applications in biotechnology. The now-established techniques in microfluidics not only include microchannels with pneumatic valves, pumps, mixers, and other specialized structures, but also enables large-scale-integration of thousands components in a single chip. There are many successful applications in biochemistry, such as cell sorting and cytometry, nanoliter PCR, protein crystallization, DNA sequencing, nucleic acids extraction and purification, immunoassays, cell studies, and chemical synthesis.

In this chapter, we focus on how to use microfluidic systems to extract gene expression information on single cells. Microfluidic devices fabricated by multilayer soft lithography possess the ability to manipulate fluids on the nanoliter scale. Therefore, they provide an ideal platform to improve single-cell gene expression profiling by manipulation of a single cell in nanoliter reactions. Cells can easily be isolated in a high-throughput manner, with highly concentrated cDNA being generated using a solid phase synthesis approach. Then the cDNA can be extracted and realtime quantitative PCR can be performed outside of the chip to amplify the target genes and measure their molecule numbers.

5.1.2 Significance of single-cell gene analysis

The fundamental challenge for stem-cell gene expression study is that stem cells are extremely rare in the context of numerous differentiated and mature cells, and there is no definitive marker for the isolation of a homogenous pure stem cell population. There is especially a lack of markers to distinguish closely related stem cells and progenitor cells. Many stem-cell gene expression profiling studies have by default used heterogeneous populations of stem cells and progenitor cells. Data obtained from these population-averaging expression profiles reflect the sum of all the subpopulations. Without knowing the relative percentages of stem cells and progenitor cells in the interrogated population, these gene expression profiles, which are the sum of all expression profiles from various cell types, are very difficult to interpret and not sufficiently informative. Even if the percentages are known, variation in the expression profiles among individual stem cells in different phases of the cell cycle would not be detectable by these current methods. Single-cell transcriptome analysis can overcome this hurdle and provide precise information on stem cell gene regulation as revealed in individual, separately analyzed cells.

Single-cell gene expression profiling from early embryos has suggested the transient expression of critical regulatory genes, again underscoring the importance of systematical single-cell expression profiling [57, 58]. Currently, multiple-color florescent-activated cell sorting (FACS) has limited utility for isolation of pure stem cell populations due to a lack of discriminating cell markers. Single-cell gene expression profiling studies with laser capture microdissection (LCM) [59-68], patch-clamp analysis [58, 69, 70], and *in situ* mRNA amplification [69, 71] have been reported, but analysis of a large number of cells has proven to be very difficult with these methods. Single-cell whole genome microarray gene expression screening [60, 61, 72] and single-cell cDNA library construction [57, 73, 74] also have been conducted on a limited number of cells. While these studies demonstrate the potential value of single-cell gene expression profiling, they also show the limitation of these methods when processing a large number of samples. Material loss and low biochemical reaction efficiency (mRNA capture and RT reaction) are other major challenges for single-cell analysis. A single mammalian cell contains 20–40 pg of total RNA [75, 76], but only 0.5–1.0 pg of mRNA (10^5 to 10^6 mRNA molecules) [77]. Therefore, detecting single-cell mRNA is difficult with current methods.

The microfluidic device described here significantly increases the mRNA-to-cDNA processing efficiency ~ 5-fold to 54% compared to bulk reactions (~ 12%) [78, 79]. With this device, we measured the absolute copy number of three genes in individual single hESCs and compared these data to those obtained from cDNA of FACS-sorted hESCs in G0/G1 phase. Our results indicate that the hESC colony is a heterogeneous cell population and many single cells do not express all three of the interrogated genes. This result suggests that pluripotent hESC colonies are not homogeneous cell populations, rather they are a highly heterogeneous cell population regulated by different gene networks. Besides stochastic factors of individual cells, heterogeneity of cells with respect to cell cycle and other factors may be a major contributor to observed variations in mammalian single-cell gene expression.

5.2 Design of microfluidic devices for single-cell analysis

5.2.1 First generation of microfluidic chip

Previous work which has been done by Joshua Marcus in the Quake laboratory [81] provided a starting point for the design of a microfluidic single-cell gene analysis device. The integrated process of cell capture/lysis, mRNA isolation/purification, and cDNA synthesis/purification is implemented in a multilayer microfluidic chip.

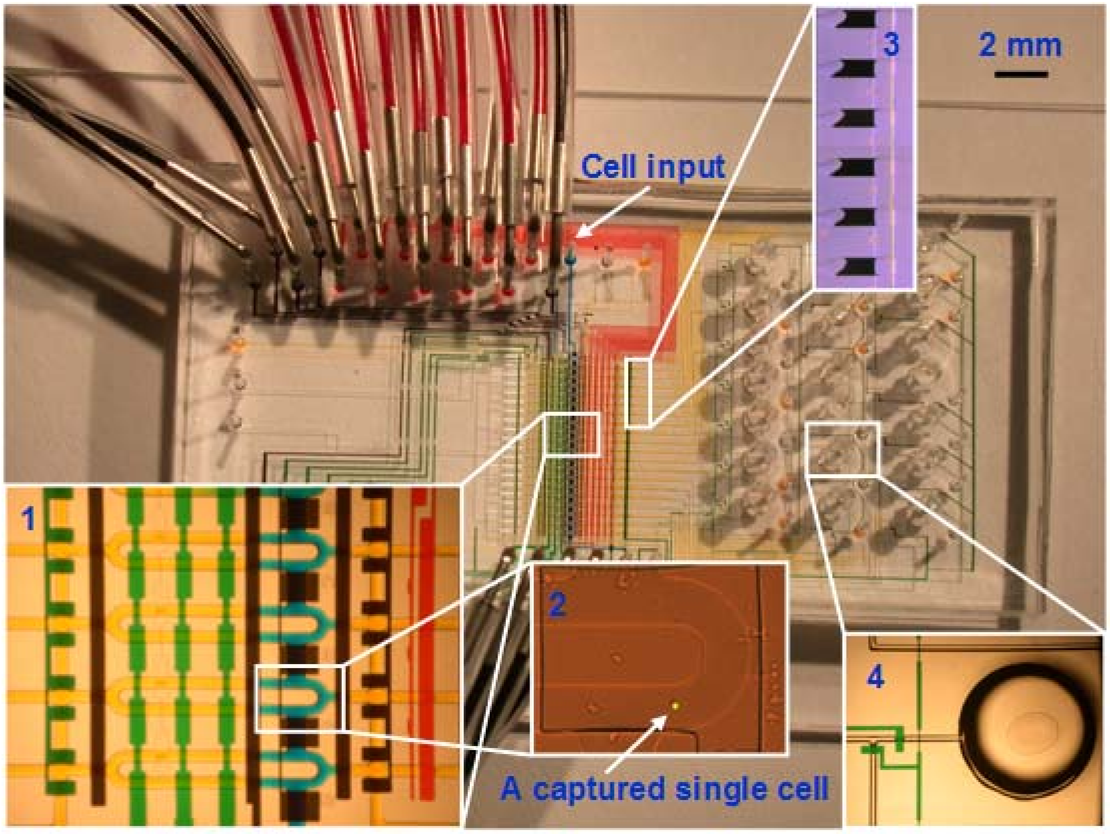

Figure 5.1: 20X single-cell mRNA extraction microfluidic device filled with food dye.

The first generation of microfluidic single-cell mRNA extraction microfluidic chip is shown in Fig. 5.1. All flow channels are filled with yellow food dye, multiplexer control channels are filled with red dye, control channels are in green dye. After loading cell suspension from the cell input inlet, single cells are captured in cell lysis module (Inset 1) within the flow channels (blue). The pump valves are green, the separation valve is black, and the lysis buffer is yellow. A captured single hESC is labeled with a fluorescent dye (green) and shown in Inset 2. Cell lysis is performed by opening the portion valve and pumping to mix lysis buffer (yellow) with the captured cell (blue). The resulting cell lysate is pushed through oligo-dT beads columns for mRNA capture. Oligo-dT beads are stacked into columns by closing the sieve valve while loading bead suspension. Inset 3 shows six stacked oligo-dT bead columns next to the sieve valve. After washing beads with buffers, RT reaction master mix is flowed through the bead columns to synthesize cDNA from the captured mRNA at 40 C. After RT reaction, beads with attached cDNA are pushed to collection wells (Inset 4) by opening the sieve valve. The beads are recovered by cutting the wells off the chips and centrifuging a flipped-well in a microcentrifuge tube.

5.2.2 Second generation of microfluidic chip

The output efficiency of the first generation of microfluidic chip is considerably low because the cells are randomly loaded in each reaction chamber. We intend to improve the efficiency of the gene analysis on the microfluidic platform to achieve real single-cell analysis. In order to achieve this goal, the chip design can be changed to implant multiplexer in both the cell loading and mRNA extraction parts of the device. Therefore, the second generation of microfluidic chip shown in Fig. 5.2 can carry out single-cell gene analysis in a 32X parallel manner. Although we do not greatly increase the number of cells to be processed, efficiency of 100% of single-cell processing can be achieved by the improved design.

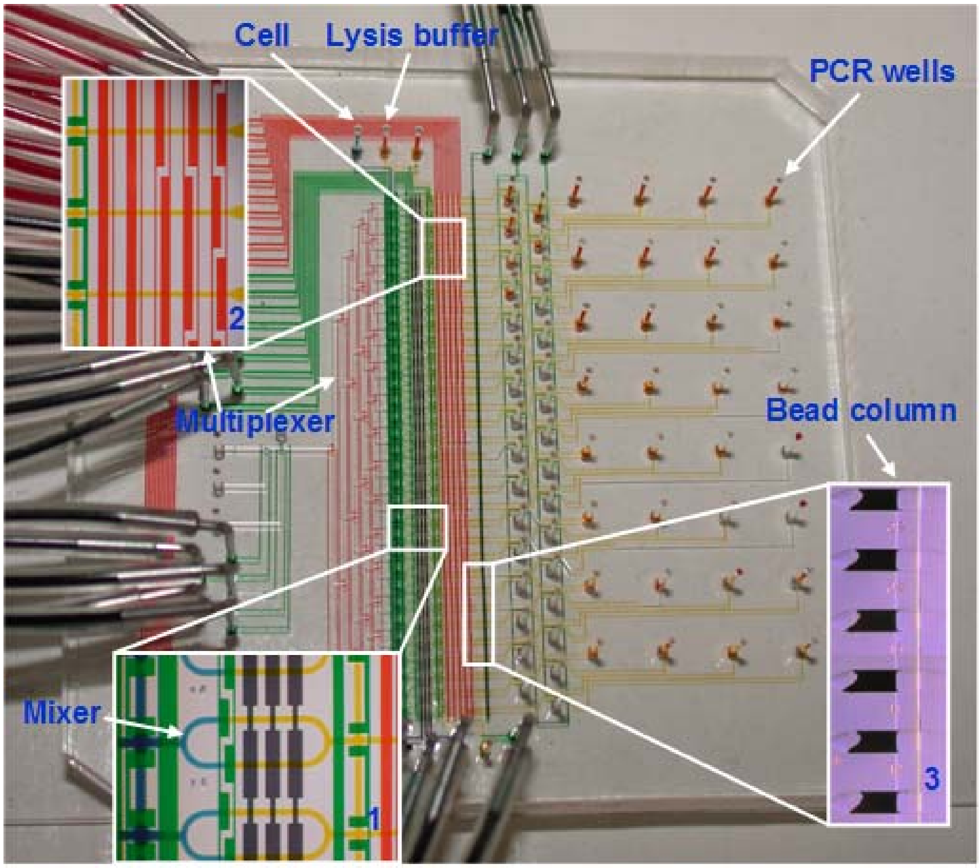

Figure 5.2: 32X single-cell gene profiling microfluidic device filled with food dye.

In the 32X single-cell microfluidic processor, all flow channels are filled with yellow dye, control channels are filled with green dye, multiplexer control channels are filled with red dye, and the cell loading portion is in blue dye. First the cell suspension is flowed through the cell loading portion, and the captured single cell can be individually pushed to the cell lysis module (Inset 1) by operating the corresponding valve in the multiplexer (Inset 2). 32 reactions can be carried out in one microfluidic device. Cell lysis is performed by opening the portion valve and pumping to mix lysis buffer (yellow) with the captured cell (blue). The resulting cell lysate is pushed through oligo-dT bead columns (Inset 3) for mRNA capture. The following RT reaction and cDNA synthesis are the same as the process in the previous version of microfluidic chip.

5.3 Materials and methods

5.3.1 Mold fabrication

All photomasks were designed with AutoCAD software, and printed at a resolution of 20,000 dots per inch on transparency films (CAD/Art services). We used both the control mold and flow mold to define device features. The control mold with 24 um high features was fabricated with a single step using SU8-2025 (Microchem, USA). The flow mold was fabricated with three lithographic steps. First we defined the 10 um high column construction flow channels with SU8-2010 (Microchem, USA). Then the 12 um high output, bead, and buffer delivery channels were fabricated using SPR220-7 (Shipley, USA). In addition, a hard bake process at 200 °C facilitating channel rounding was necessary for valve closure. The last step was to construct the 40 um high cell loading channels with AZ-50 (Clariant). In all optical lithography processes, mold exposures were under UV light on a MA6 mask aligner.

5.3.2 Device fabrication

The microfluidic devices were fabricated by multilayer soft lithography with the silicone elastomer polymethylsiloxane (PDMS, General Electric). Each device employs push-up valve geometry and consists of a three-layer elastomeric structure.

The molds were first exposed to chlortrimethylsilane (TMCS, Aldrich) vapor for 2 min to promote elastomer release after the baking steps. For the flow layer of the device, a mixture of PDMS (5 parts A: 1 part B) was poured onto a flow mold. After degassing, the flow molds were baked for 45 min at 80 °C. For the control layer of the device, a mixture of PDMS (20 parts A: 1 part B) was spun on the control mold at 1800 rpm and baked for 30 min at 80 °C. The flow layer was separated from the flow mold and flow channel access holes were then punched. Next, the flow and control layers were aligned and baked for 45 min at 80 °C. The two-layer structure was peeled from the control mold with control channel access holes punched, and was mounted to another thin PDMS layer made by spinning 20:1 PDMS mixture on a blank wafer. After baking for 3 hours at 80 °C, the three-layer structure was bonded to a clean microscope slide and baked overnight at 80 °C.

5.3.3 Microfluidic station

Fig. 5.3 shows the setup of the microfluidic system. The microfluidic valves within the device are controlled by individual pressure regulators (Fluidigm, USA) and are interfaced via 23 gauge stainless steel tubing (New England Small Tube) and tygon tubing (VWR). An NI-DAQ card through a Labview interface (National Instruments) was used to control the pressure regulators.

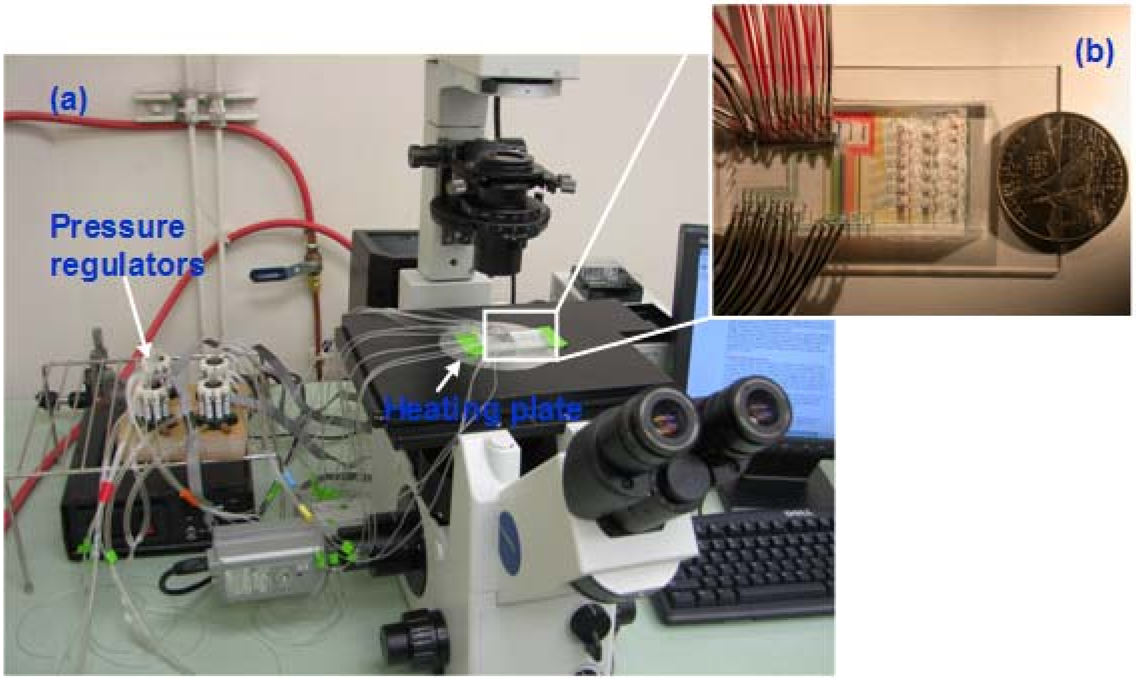

Figure 5.3: The setup of the microfluidic device for single hESC mRNA extraction. (a) The system includes a microscope, a computer to control air pressure with pressure regulators, and a heating plate. (b) A typical microfluidic chip.

5.3.4 Synthesis of cDNA from hESCs

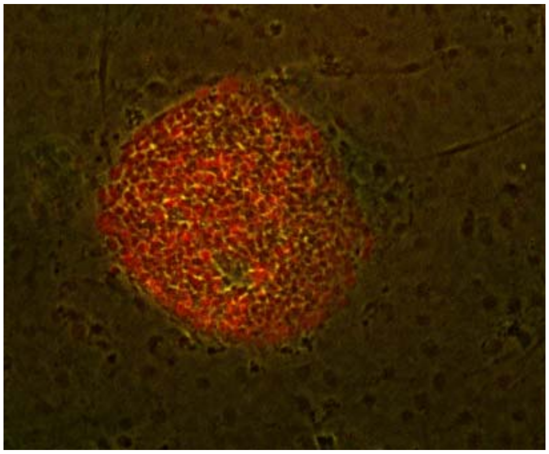

Figure 5.4: Merged image of immunofluorescent-stained (Oct-3/4) and light microscope images from a pluripotent hESC colony. The hESC colony was labeled with mouse α human Oct-3/4 IgG and PE-conjugated rabbit anti-mouse IgG antibodies. Only cells in the center of the hESC colony expressed Oct-3/4.The intensity of the labeling indicates the Oct-3/4 positive cells expressed Oct-3/4 at different levels. The spontaneous differentiated cells around the colony do not express Oct-3/4.

Fig. 5.4 shows the human embryonic stem cell (hESC) colonies for microfluidic analysis. The centers (100 to 200 cells) of hESC colonies from feeder-free cultures (matrigel) were mechanically picked up with a 25 gauge needle. The cells were disassociated into single-cell suspension with trypsin. After being labeled with a DNA-selective dye for living cells, Vybrant DyeCycle Green (Invitrogen, USA), FACS was performed to isolate cells in G0/G1 phase based on DNA content. These isolated cells were pooled to extract total RNA with Trizol LS (Invitrogen, USA), or loaded into the microfluidic device for processing. Typically, 150,000 FACS-sorted cells were pooled for Trizol RNA extraction, and 2,000 to 5,000 cells were used for microfluidic experiments. To compare the efficiency of bench-top bulk assays to microfluidic assay, the same biochemical reagents were used for the bulk assay and the microfluidic device.

Single-cell lysis, mRNA capture, and RT were performed in the same microfluidic device to convert mRNA into cDNA. Dynabeads with oligo $(dT)_{25}$ (Invitrogen, USA) were used to capture mRNA. Sensiscript RT kit (Qiagen, USA) was used for converting captured mRNA to cDNA. The oligo $(dT)_{25}$ sequence in Dynabeads serves as both mRNA capture sequence and primer for cDNA synthesis. After oligo $(dT)_{25}$ beads with attached cDNA were flushed to the collection wells, the wells were cut off from the chip. Centrifugation was used to transfer the beads from individual wells into PCR tubes. These beads with attached cDNA from individual cells were subjected to realtime qPCR for measurement of molecule numbers of interrogated mRNA in IQ5 (Bio-Rad, USA).

5.4 Operation of microfluidic device

The process flow in the single-cell microfluidic processor is shown in Fig. 5.5. The processor captures mRNA from 20 single cells separately and simultaneously, and then converts it into individual cDNA. The lysis buffer was loaded into the flow channels until it reached the waste outlets, so as to leave no air bubbles in the channel. Oligo $(dT)_{25}$ beads (Invitrogen, USA) were then loaded, and columns were built serially by addressing flow lines individually with the multiplexer control channels, while keeping the sieve valve actuated. Once columns were built, excess beads still present in the flow channels were flushed with the lysis buffer to the constructed columns. A single-cell suspension was then loaded. By adjusting cell concentration and flow rate, a single hESC was captured in an individual cell-lysis module. Cells were then lysed chemically by mixing cells with the lysis buffer in the ~ 10 nl ring. Mixing occurred by executing a peristaltic pump sequence [80, 81] with control channels. Cell lysates were then pushed via pneumatic pressure over the affinity columns to captured mRNA with oligo $(dT)_{25}$ beads. After washing the columns with a first strand synthesis buffer, the reverse transcription (RT) master mix was introduced. Once the RT master mix filled the flow channels, first strand synthesis was then carried out by heating the processor to 40 °C on a thermal microscope stage. The oligo $(dT)_{25}$ beads served as both primers (oligo $(dT)_{25}$ sequences and a solid phase support. The RT reaction mixture (99 ul) was flowed over the columns for 45 min until the RT reaction was completed at a flow rate of ~ 20 μm/s. Upon completion of the RT reaction, the waste valves were closed, and collection valves were opened. The beads were sent to collection wells by opening the sieve valves and flowing columns of the processor in a serial manner with a PCR buffer. The fluid multiplexer was used to push beads in each of the 20 reaction channels individually. Beads were collected by cutting the collection wells off the device and centrifuging the beads into PCR tubes.

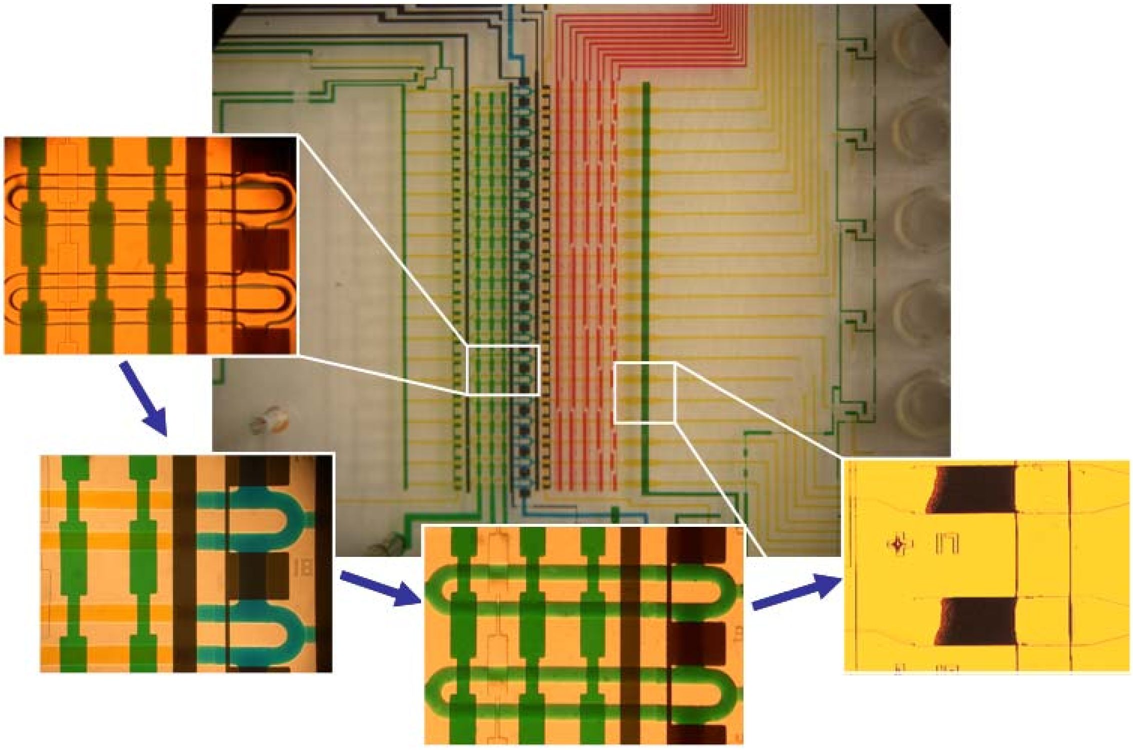

Figure 5.5: The process flow in the single-cell microfluidic processor.

5.5 Results and discussion

5.5.1 Device efficiency

Single-cell measurement of mRNA is difficult. One difficulty results from the loss of material during the steps of single-cell capture, lysis, mRNA isolation, and cDNA synthesis. Unlike the DNA molecule, mRNA is very susceptible to degradation by widely existing RNase. Therefore, it is essential to carry out the cDNA first strand synthesis on the same device immediately after mRNA capture. Another difficulty in measurement is the low mRNA-to-cDNA efficiency, mRNA capture (~ 40–50%) and RT reaction (~ 20%) [78, 79] in bulk assays.

In order to measure the absolute number of molecules of mRNA with standard curves, the mRNA-to-cDNA efficiency of the processor must be obtained. An artificial Poly-A RNA standard (Affymetrix, USA) was used to compare the input mRNA copy number to the cDNA copy number which was measured by qPCR at the end of the processes. This RNA standard contains known amounts of artificial RNAs with poly-A tails from 4 *B. subtilis* genes, *lys, phe, thr,* and *dap.* The *lys* gene was used as RNA standard for calculation of mRNA-to-cDNA efficiency. A standard curve was generated with a known amount of *lys* DNA at 10-fold dilutions. The mRNA capture and RT reaction were carried out at both conventional micro-liter level and at nanoliter scale with the microfluidic processor.

In the conventional reaction, a 50 μl RT reaction was carried out after capturing 4 μl of artificial mRNA (7.3 nM) with 30 μl oligo $(dT)_{25}$ beads, as instructed by the manufacturer. One microliter of the RT product (corresponding to 2.16×10^8 molecules of *lys* artificial mRNA) was used for realtime quantitative PCR (qPCR) detection. Based on the standard curve, the final detected molecule number was $2.5\pm 0.5\times10^7$ molecules (Table 5.1). The processing efficiency of a conventional microliter scale reaction is 12%. To compare the efficiency of conventional and microfluidic approaches, the same artificial RNA sample was introduced into the cell capturing chamber, processed into cDNA and detected with realtime qPCR. Each of the 20 cell-capture chambers in the microfluidic device has a volume of 3.4 nl, resulting in 1.84×10^6 molecules of input *lys* artificial mRNA.

The qPCR detected absolute *lys* cDNA molecule number is $1.0\pm 0.3\times10^6$ with the standard curve. The total processing efficiency was 54% which is approximately 5 times the efficiency of the conventional approach. A series of 10-fold dilutions of the artificial RNA were used and verified that the processing efficiencies of both approaches do not vary significantly in different concentrations of the input artificial RNA. The standard deviations of both bench-top and microfluidic reactions were also calculated and are similar (Table 5.1). The small standard deviation of the 20 reactions in the same device indicates consistent processing efficiency among the 20 reaction chambers.

Table 5.1: Microfluidic device increasing mRNA capture and reverse transcription (RT) efficiency. Known amounts of artificial *lys* mRNAs in a mixture with 3 other polyA artificial RNAs were processed with traditional microliter scale reaction or with microfluidic device in nanoliter scale. A standard curve was generated with a known amount of *lys* DNA for the detection of cDNA molecule numbers (y = -3.5547X + 39.538 R2 = 0.99). Molecule numbers of *lys* cDNA were calculated from the standard curve with real-time PCR threshold cycles. Processing efficiencies were calculated by dividing the measured cDNA molecule numbers to the input mRNA molecule numbers.

	Input *lys* RNA (molecule umber)	Threshold Cycle	Detected cDNA (molecule number)	Efficiency (%)
Microliter Reaction (Bench-top)	2.16×10^8	13.22 ± 0.37 (n = 20)	$2.6\pm0.6\times10^7$	12 %
Nanoliter Reaction (Microfluidic)	1.84×10^6	18.15 ± 0.46 (n = 20)	$1.0\pm0.3\times10^6$	54 %

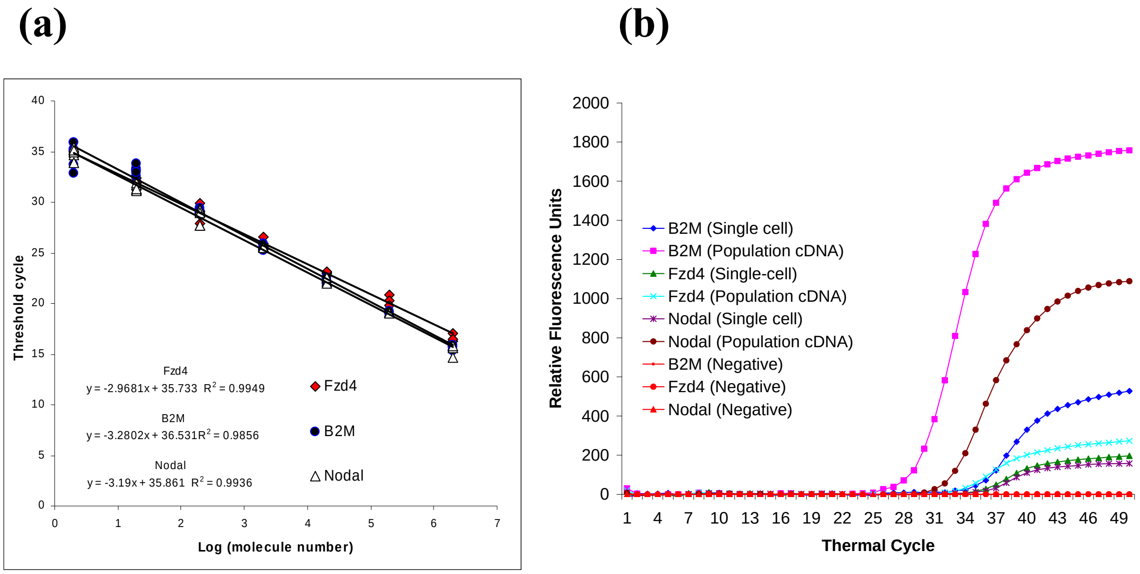

Figure 5.6: Measuring absolute molecule numbers of three genes in single hESC with multiplex quantitative PCR. (a) Standard curves are generated with known amounts of plasmid DNA containing the full sequence of the genes. The curves cover from 2 to $2x10^6$ copies of the respective genes. With our primer design, all the curves overlap each other, and indicate similar PCR efficiency. The insert is the representative amplification cures of the B2M genes from 2 to $2x10^6$ copies in 10-fold dilution. (b) The multiplex quantitative PCR amplification curves obtained from cDNA of hESC colonies are plotted with curves obtained from cDNA of a representative hESC. Because the standard curves of the three genes are very similar, these amplification curves show that the expression ratio of B2M and Nodal is similar in population cDNA and this single-cell cDNA. However, the expression of Fzd4 and Nodal is very similar in this particular single hESC, but very different in the hESC population. Unlike this single hESC, some single hESC do not express all three genes. This result suggests the heterogeneity of hESC and underscores the importance of single-cell analysis.

5.5.2 Gene expression of single hESC cells

Conventional gene expression studies were carried out with RNA extracted from cell populations. To investigate whether the gene expression of a cell population is a reasonable sum of the expressions of individual cells, the expression levels of three genes were measured by two approaches: with pooled cDNA from the hESC population and with cDNA from individual hESCs.

Based on the mRNA-to-cDNA efficiency calculated above, the molecule numbers of three mRNA in single hESCs were measured. Standard curves were constructed with known amounts of full-length B2M, Fzd 4, and Nodal cDNA. The three standard curves overlap each other, indicating similar qPCR efficiency for each set of the primers (Fig. 5.6). These standard curves have a range of 2 to 2×10^6 molecules that allows the direct comparison of the expression levels of these three genes from their amplification curves (Figure 3B). The minimal detectable level is 4 molecules (2/54%) for our microfluidic processor, and 17 molecules (2/12%) for bulk assays with these standard curves.

The pluripotent hESC colonies are often considered and treated as a homogenous population. However, our data indicate that this is not the case. As Figure 3B shows, the absolute expression levels (mRNA molecule number) measured from cDNA equivalents to 1,000 cells are not even close to 1,000 fold of the levels measured from a typical single-cell. With cDNA equivalent to 1,000 G1/G0 phase hESC, the absolute molecule numbers of B2M, Nodal, and Fzd4 are 6,034±660, 402±55, and 69±19, respectively. However, the distributions of molecule numbers of these 3 genes are diverse in single hESCs (Fig. 5.7). Among the 54 interrogated single hESCs, 14.8%, 37% and 37% of hESC did not express detectable levels (less than 4 copies) of B2M, Fzd4 and Nodal respectively. The expression of B2M ranged from 4 to 76 copies, with the majority between 30 and 50 copies. The expression of Fzd4 and Nodal ranged from 6 to 548 copies, and 22 to 504 copies respectively. All cells expressed at least one of the 3 genes.

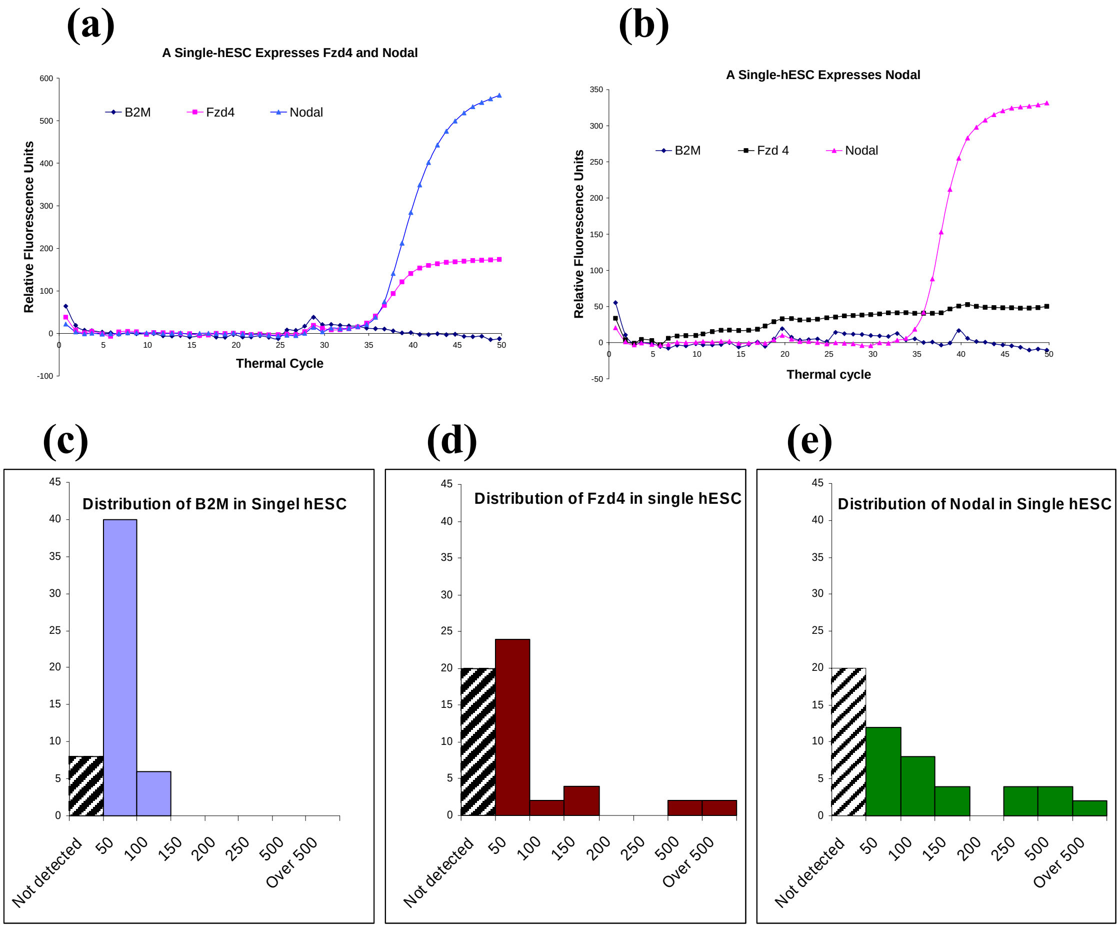

Figure 5.7 Expression of B2M, Nodal, and Fzd4 in a single hESC. (a) A single-hESC expresses both Nodal and Fzd4, but does not express B2M in a detectable level. (b) A single hESC expresses only Nodal. The mRNAs of B2M and Fzd4 are undetectable. (c), (d), and (e) show the distribution of the B2M, Fzd4 and Nodal in a single hESC. Among the 54 interrogated single hESC, 14.8%, 37%, and 37% of cells (indicated by black strait pattern) do not express detectable levels (less than 4 copies) of B2M, Fzd4, and Nodal, respectively. The distribution pattern of expressions is narrower in B2M compared to the other 2 genes. The discontinued distribution of Nodal and Fzd4 suggest a high heterogeneity of the 54 cells.

Many gene expression studies, such as microarray or quantitative PCR, are based on the relative expression level of genes with normalization to a housekeeping gene which is assumed to have similar expression in all samples. Our data show that even the relative expression level of the three genes are very different between measurements derived from cDNA of a cell population and separately from individual cells. In the measurement from population cDNA, the expression level of Fzd4 is approximately 8-fold lower than the expression of Nodal after being normalized to B2M. However, in a representative single hESC, the expression levels of Nodal and Fzd4 are very similar after normalization with B2M (Fig. 5.7).

5.6 Conclusions

Microfluidic devices that are designed to manipulate nanoliter amounts of reagents provide a desirable platform for single-cell gene expression processing. As our data indicate, capturing mRNA and converting it to cDNA in a microfluidic device not only consumes significantly less reagents, but most importantly increases the efficiency of biochemical reactions. The microfluidic device described has a mRNA-to-cDNA efficiency 5 times better than the corresponding bench-top reactions. Previous studies showed a 40–55% mRNA capture efficiency of oligo $(dT)_{25}$ [78], and ~ 20% RT efficiency [79] in conventional bench-top reactions. The 12% overall efficiency of our bulk assay is consistent with these previous studies (55% × 20%). With our microfluidic device, the mRNA-to-cDNA processing efficiency is 54% (5-fold better than bulk assay). This finding indicates a very efficient mRNA-to-cDNA processing that may be due to the nanoliter scale reaction. This mRNA-to-cDNA efficiency is similar to the previously reported efficiency from other microfluidic devices [82].

Due to the nanoliter scale nature of the microfluidic device, the input number of mRNA in conventional reaction and microfluidic reaction is ~ 100-fold different when the same RNA standard is used. To rule out the possibility of RNA concentration in processing efficiency, serial 10-fold dilutions of the RNA standard were used for the same experiments. The mRNA-to-cDNA efficiencies are not significantly different for either bench-top or microfluidic reactions. Therefore, the high mRNA-to-cDNA efficiency is a desirable characteristic of microfluidic devices. With this 54% processing efficiency, the microfluidic device described potentially can detect 2 mRNA copies of interrogated genes.

In our device, there are 20 individual single-cell processing reactors for simultaneously processing. The standard deviation of threshold cycles of the 20 reactors is small (0.37) and similar to those from conventional reactions (~ 0.5). These data indicate that the processing efficiencies among the 20 reactors are very similar. Similar results are also obtained in multiple lots of devices. This aspect is critical for comparing results from individual cells intra- and inter-device.

With this device, we profiled the expression of three genes in hESC. Our data indicated that even for FACS-sorted G1/G0 phase hESC, the expression data from population cDNA can not be used to estimate the gene expression level in individual cells. Approximately 10–15% of individual cells do not express one of the three interrogated genes. Therefore, the population averaging effect distorts the expression levels of the three genes in bulk assays conducted with population cDNA from hESC colonies. Because the population averaging effects are not the same for all three genes, the relative expression levels are also distorted. The qPCR with cDNA from 1,000 hESC indicates that Nodal is expressed approximately 8 times higher than Fzd4 after normalization to B2M. However, in individual cells the expressions of these genes are very diverse. The difference observed in pooled cDNA may be due to the different number of cells expressing the respective genes.

It has been reported that gene expression is highly variable at the single-cell levels [83, 84]. A speculation is that the high variability is due to experimental variation. In the present study, we showed that experimental variation may not be the main factor. The stochastic gene expression behavior of single cells (biological noise) has been reported in various studies of prokaryote cells [85-89]. Biochemical processes such as transcription, translation, RNA and protein degradation have been thought of as the primary contributors. However, heterogeneity of the mammalian cell populations may be a factor related to the observed expression variations in single-cell analysis of mammalian cells. When gene expression studies are conducted at the single-cell level, we must recognize that no two cells are identical. In a particular mammalian cell population, two cells are always different in cell cycle, differentiation stages, and environmental stimulation. The variation of gene expression at the single-cell levels is expected, and the reason may be due to stochastic expression fluctuation, or to heterogeneity of the cell populations. In mammalian cells which are regulated by more complex gene networks than yeast and bacteria, cell heterogeneity may be the major contributor of variation of gene expression at single-cell levels.

Chapter 6

Summary

Microfluidics is increasingly being used in many areas of biotechnology to achieve reduced reagent volumes, improved performance, parallelism and integration. In this thesis, we presented the construction of both the solid-state and optofluidic dye lasers as active light sources in microfluidic system, and studied the biochemical compatibility of the microfluidic system. The work we demonstrated here represents two important aspects of integration in microfluidics: optics and biochemistry. Through the nanofabrication technology, the useful implementation of biotechnology in microfluidic devices will continue to increase.

The miniaturized dye lasers with circular grating resonant cavities have many attractive lasing performance features, such as low threshold operation, surface emission, and well-defined output beam. Typical laser thresholds achieved are well within the reach of commercial high-power laser diodes, thus enabling the construction of portable laser devices using compact laser diodes as the pump source.

There are many microsystem analyses in the field of biochemistry that require the use of coherent light sources. For example, fluorescence actuated cell sorters (FACS), fluorescence-based DNA sequencers, and laser-induced fluorescence spectrometers are some of the applications that can utilize the dye laser system. The scheme for making highly parallel multiplexed biosensors and scanning free spectrometer on chip using tunable laser arrays is very straightforward and promising. With the development of an integrated microfluidic spectroscopy system, the creation of a true lab-on-a-chip is very close to reality.

Microfluidic devices that are designed to manipulate nanoliter amounts of reagents provide a desirable platform for single-cell gene expression processing. The single cell analysis presented here provides an example of using microfluidic circuits to perform various biochemical experiments. The system can be further developed to accommodate many other related biochemical process, such as PCR and microarray, which can utilize the miniaturized light sources to construct compact detection systems. The combination of miniaturized light source, imager, appropriate filters, and microfluidics allows the creation of a powerful experimental tool.

In summary, the work described in this thesis presents an important step towards completely integrated microfluidics with optical functionality and biochemical compatibility. The full potential of microfluidics integration has yet to be explored, with novel materials and improved fabrication techniques, we believe that new implementations in microfluidics with useful biochemical applications can be achieved.

Appendix A

Fabrication Recipes for Microfluidic Single Cell Processor

A.1 Photolithography processes

A.1.1 SU8-2010 10 µm / SPR220-7 15 µm / AZ-50 40 µm flow mold

1. Spin SU8-2010 at 3000 rpm for 1 min with an acceleration of 15.
2. Soft bake mold for 1 min / 3 min at 65 °C / 95 °C.
3. Expose mold for 20 s on MA6 mask aligner.
4. Post bake mold after exposure for 1 min / 3 min at 65 °C / 95 °C.
5. Develop in SU8 developer.
6. Once developed, hard bake mold at 150 °C for 2 hr.
7. Expose mold to HMDS vapor for 2 min.
8. Spin SPR220-7 at 1500 rpm for 1 min with an acceleration of 15.
9. Soft bake mold for 90 s at 105 °C.
10. Expose mold under a positive transparency mask for 100 s on MA6 mask aligner.
11. Develop mold in MF-319 developer and rinse under a stream of H_2O.
12. Hard bake 2 hr at 200 °C.
13. Expose mold to HMDS vapor for 90 s.
14. Spin AZ-50 at 1600 rpm for 1 min with an acceleration of 15.
15. Soft bake mold for 2 min / 5 min at 65 °C / 115 °C.
16. Expose mold under a positive transparency mask for 150 s on MA6 mask aligner.

17. Develop mold in 3:1 H_2O:2401 developer. Rinse mold under a stream of H_2O.
18. Once developed, hard bake 3 hr at 200 °C.

A.1.2 SU8-2025 23 μm control mold

1. Spin SU8-2025 at 3000 rpm for 1 min with an acceleration of 15.
2. Soft bake mold for 2 min / 5 min at 65 °C / 95 °C.
3. Expose mold under a negative transparency mask for 30 s on MA6 mask aligner.
4. Post bake mold after exposure for 2 min / 5 min at 65 °C / 95 °C.
5. Develop in SU8 developer.
6. Once developed, bake mold at 95 °C for 1 min to evaporate excess solvent.

A.2 3-layer PDMS device fabrication (push-up valves)

1. Prepare 5:1 GE RTV A : RTV B (mix 1 min, de-foam 5 min).
2. Expose flow mold to TMCS vapor for 2 min.
3. Pour 30 g 5:1 GE RTV A : RTV B on respective flow mold.
4. Degas flow mold under vacuum.
5. Bake flow mold for 45 min at 80 °C.
6. While flow mold is de-gassing, prepare 20:1 GE RTV A : RTV B (mix 1 min., de-foam 5 min.).
7. Expose control mold to TMCS vapor for 2 min.
8. Spin 20:1 RTV mix at 1800 rpm for 60 s with a 15 s ramp.
9. Let RTV settle on control mold for ~ 30 min before baking for 30 min at 80 °C.
10. Bake control mold for 30 min at 80 °C.
11. Cut devices out of flow mold and punch holes with 650 μm diameter punch tool (Technical Innovations #CR0350255N20R4).

12. Clean flow device with transparent tape and align to control mold.

13. Bake 2-layer device for 45 min at 80 °C.

14. While 2-layer device is baking, prepare 20:1 GE RTV A : RTV B (mix 1 min, defoam 5 min) to spin on blank silicon wafer.

15. Expose blank wafer to TMCS vapor for 2 min.

16. Spin 20:1 RTV mix on a blank wafer at 1600 rpm for 60 s with a 15 s ramp.

17. Bake blank wafer for 30 min at 80 °C.

18. Cut out 2-layer device from control mold, punch holes with 650 μm diameter punch tool (Technical Innovations #CR0350255N20R4). Also punch the 2 mm big holes using the big punch tool (Technical Innovations # CR0830655N14R4).

19. Clean with tape and mount on blank wafer. Check for debris and collapsed valves.

20. Bake 3-layer RTV device for 2 hr at 80 °C.

21. Cut 3-layer device out, clean with tape and mount on a clean glass slide. Check for collapse.

22. Bake finished device overnight at 80 °C.

Appendix B

Single Cell Preparation Recipes

B.1 Culture of human embryonic stem cell

The hESC line (H9) was obtained from the WiCell Research Institute (Madison, WI) and maintained as instructed [90]. Undifferentiated hESCs were cultured on an irradiated (5,500 rads) layer of mouse embryonic fibroblast (MEF) feeder cells in 6-well plates or in matrigel-coated plates with MEF-conditioned medium. To avoid contamination of mouse cells from the MEF, hESC colonies were dissected and transferred to matrigel-coated plates before using for microfluidic processing.

MEF were prepared from the embryos of 13–14 day pregnant CF-1 mice (Charles River Labs) and stocks were cryopreserved until required for culture of hESCs. hESCs were consistently observed as large clumps that appeared on the matrigel-coated surface, consistent with the published observations of others. Periodic karyotyping confirmed their human diploid chromosomal character. After injection into severe combined immunodeficient (SCID) mice, these cells produced teratomas which include tissues of ectodermal, mesodermal, and endodermal origin. Immunostaining of the hESC colonies for alkaline phosphatase and with antibodies specific for SSEA-4, TRA-1-60, TRA-1-81, or Oct-3/4 confirmed the pluripotency of these cells.

B.2 Standard curves for PCR amplification

Human fetal brain cDNA (Invitrogen, USA) and cDNA generated from poly-A RNA control kit (Affymetrix, USA) were used as templates to obtain quantitative PCR amplicons. Quantification of the PCR amplicons was performed by gel densitometry with DNA ladders (Norgen, Canada). These amplicons contain the majority of the cDNA sequence of the respective genes and were used for generating standard curves for qPCR. The *lys* standard curve was generated with a known amount of a 846 bp fragment of the *lys* cDNA. The primers for the amplification were: cagtcaacccttaccgcatt (forward) and acatggacaggaggcatttc (reverse).

Three sets of primers were used to amplify 905bp, 982bp, and 890bp fragments of B2M, Nodal, and Fzd4, respectively from human brain cDNA (Invitrogen, USA). The primer sets were:

B2M: ggcattcctgaagctgaca (forward) and ccagattaaccacaaccatgc (reverse);

Nodal: cttcctgagccaacaagagg (forward) and cagactccactgagcccttc (reverse);

Fzd4: gggacgtctaaaatcccaca (forward) and ggcagtggagatgaaacaca (reverse).

B.3 Quantitative PCR

Four sets of multiplex Taqman primers and probes were designed with Beacon Designer (Premier Biosoft International, USA).

B2M: aattgctatgtgtctgggtttcatcc (forward), gcttacatgtctcgatcccacttaac (reverse) and acaaagtcacatggttcacacggcaggca (probe-FAM);

Nodal: catacatccagagtctgctgaaacg (forward), atcagaggcacccacattcttcc (reverse) and cccaccgagtcccttccacttgttgtgcc (probe-Cy5);

Fzd4: cgaccccatccgcatctcc (forward), acattggcacataaacagaacaaagg (reverse) and ccagaacctcggctacaacgtgaccaaga (probe-Hex);

Lys: ggccggttttgtgttagcag (forward), gcggttcatcatcttccgtataac (reverse) and ccgaaacctcctccaagattcagcacct (probe-FAM).

Multiplex quantitative PCR was performed with IQ-5 (bio-rad, USA) and Quantitect Taqman PCR kit (Qiagen, USA) for B2M, Nodal, and Fzd4. The qPCR of *lys* was performed independently from the multiplex qPCR.

Bibliography

[1] G. M. Whitesides, "The origins and the future of microfluidics," *Nature,* vol. 442, pp. 368-373, Jul 27 2006.

[2] E. Verpoorte, "Chip vision - optics for microchips," *Lab on a Chip,* vol. 3, pp. 42n-52n, 2003.

[3] F.P.Schafer, *Dye Lasers*, 3rd ed. New York, 1990.

[4] A. E. Siegman, *lasers*. Mill Valley: University Science Books, 1986.

[5] C. M. Wu, T. Makino, J. Glinski, R. Maciejko, and S. I. Najafi, "Self-Consistent Coupled-Wave Theory for Circular Gratings on Planar Dielectric Wave-Guides," *Journal of Lightwave Technology,* vol. 9, pp. 1264-1277, Oct 1991.

[6] T. Erdogan and D. G. Hall, "Circularly Symmetrical Distributed Feedback Semiconductor-Laser - an Analysis," *Journal of Applied Physics,* vol. 68, pp. 1435-1444, Aug 15 1990.

[7] T. Erdogan and D. G. Hall, "Circularly Symmetrical Distributed Feedback Laser - Coupled Mode Treatment of Te Vector-Fields," *IEEE Journal of Quantum Electronics,* vol. 28, pp. 612-623, Mar 1992.

[8] P. L. Greene and D. G. Hall, "Effects of radiation on circular-grating DFB lasers - Part I: Coupled-mode equations," *IEEE Journal of Quantum Electronics,* vol. 37, pp. 353-364, Mar 2001.

[9] P. L. Greene and D. G. Hall, "Effects of radiation on circular-grating DFB lasers - Part II: Device and pump-beam parameters," *IEEE Journal of Quantum Electronics,* vol. 37, pp. 365-371, Mar 2001.

[10] P. Yeh, A. Yariv, and E. Marom, "Theory of Bragg Fiber," *Journal of the Optical Society of America*, vol. 68, pp. 1196-1201, 1978.

[11] A. Yariv, *Optical Electronics in Modern Communications*, 5th ed. New York: Oxford University Press, 1997.

[12] D. Ochoa, R. Houdre, M. Ilegems, H. Benisty, T. F. Krauss, and C. J. M. Smith, "Diffraction of cylindrical Bragg reflectors surrounding an in-plane semiconductor microcavity," *Physical Review B,* vol. 61, pp. 4806-4812, Feb 15 2000.

[13] A. Jebali, D. Erni, S. Gulde, R. F. Mahrt, and W. Bachtold, "Analytical calculation of the Q factor for circular-grating microcavities," *Journal of the Optical Society of America B-Optical Physics,* vol. 24, pp. 906-915, Apr 2007.

[14] M. Hammer, "1-D multilayer slab waveguide mode solver," *http://wwwhome.math.utwente.nl/~hammer/oms.html*, 2003.

[15] Y. Oki, K. Aso, D. Zuo, N. J. Vasa, and M. Maeda, "Wide-wavelength-range operation of a distributed-feedback dye laser with a plastic waveguide," *Japanese Journal of Applied Physics Part 1-Regular Papers Short Notes & Review Papers,* vol. 41, pp. 6370-6374, Nov 2002.

[16] Y. Oki, S. Miyamoto, M. Maeda, and N. J. Vasa, "Multiwavelength distributed-feedback dye laser array and its application to spectroscopy," *Optics Letters,* vol. 27, pp. 1220-1222, Jul 15 2002.

[17] Y. Oki, T. Yoshiura, Y. Chisaki, and M. Maeda, "Fabrication of a distributed-feedback dye laser with a grating structure in its plastic waveguide," *Applied Optics,* vol. 41, pp. 5030-5035, Aug 20 2002.

[18] C. Bauer, H. Giessen, B. Schnabel, E. B. Kley, C. Schmitt, U. Scherf, and R. F. Mahrt, "A surface-emitting circular grating polymer laser," *Advanced Materials,* vol. 13, pp. 1161-+, Aug 3 2001.

[19] G. A. Turnbull, A. Carleton, G. F. Barlow, A. Tahraouhi, T. F. Krauss, K. A. Shore, and I. D. W. Samuel, "Influence of grating characteristics on the operation of circular-grating distributed-feedback polymer lasers," *Journal of Applied Physics,* vol. 98, pp. -, Jul 15 2005.

[20] S. Y. Chou, P. R. Krauss, and P. J. Renstrom, "Nanoimprint lithography," *Journal of Vacuum Science & Technology B,* vol. 14, pp. 4129-4133, Nov-Dec 1996.

[21] J. R. Lawrence, P. Andrew, W. L. Barnes, M. Buck, G. A. Turnbull, and I. D. W. Samuel, "Optical properties of a light-emitting polymer directly patterned by soft lithography," *Applied Physics Letters,* vol. 81, pp. 1955-1957, Sep 9 2002.

[22] D. Pisignano, L. Persano, P. Visconti, R. Cingolani, G. Gigli, G. Barbarella, and L. Favaretto, "Oligomer-based organic distributed feedback lasers by room-temperature nanoimprint lithography," *Applied Physics Letters,* vol. 83, pp. 2545-2547, Sep 29 2003.

[23] D. Pisignano, M. F. Raganato, L. Persano, G. Gigli, P. Visconti, G. Barbarella, L. Favaretto, M. Zambianchi, and R. Cingolani, "The luminescence quantum yield of

organic one-dimensional periodic nanostructures," *Nanotechnology,* vol. 15, pp. 953-957, Aug 2004.

[24] S. Y. Chou, P. R. Krauss, and P. J. Renstrom, "Imprint of Sub-25 Nm Vias and Trenches in Polymers," *Applied Physics Letters,* vol. 67, pp. 3114-3116, Nov 20 1995.

[25] Y. G. Zhao, W. K. Lu, Y. Ma, S. S. Kim, S. T. Ho, and T. J. Marks, "Polymer waveguides useful over a very wide wavelength range from the ultraviolet to infrared," *Applied Physics Letters,* vol. 77, pp. 2961-2963, Nov 6 2000.

[26] T. Erdogan, O. King, G. W. Wicks, D. G. Hall, E. H. Anderson, and M. J. Rooks, "Circularly Symmetrical Operation of a Concentric-Circle-Grating, Surface-Emitting, Algaas/Gaas Quantum-Well Semiconductor-Laser," *Applied Physics Letters,* vol. 60, pp. 1921-1923, Apr 20 1992.

[27] G. F. Barlow, A. Shore, G. A. Turnbull, and I. D. W. Samuel, "Design and analysis of a low-threshold polymer circular-grating distributed-feedback laser," *Journal of the Optical Society of America B-Optical Physics,* vol. 21, pp. 2142-2150, Dec 2004.

[28] G. A. Turnbull, A. Carleton, A. Tahraouhi, T. F. Krauss, I. D. W. Samuel, G. F. Barlow, and K. A. Shore, "Effect of gain localization in circular-grating distributed feedback lasers," *Applied Physics Letters,* vol. 87, pp. -, Nov 14 2005.

[29] A. Jebali, R. F. Mahrt, N. Moll, D. Erni, C. Bauer, G. L. Bona, and W. Bachtold, "Lasing in organic circular grating structures," *Journal of Applied Physics,* vol. 96, pp. 3043-3049, Sep 15 2004.

[30] J. Wang, X. Y. Sun, L. Chen, and S. Y. Chou, "Direct nanoimprint of submicron organic light-emitting structures," *Applied Physics Letters,* vol. 75, pp. 2767-2769, Nov 1 1999.

[31] R. H. Jordan, D. G. Hall, O. King, G. Wicks, and S. Rishton, "Lasing behavior of circular grating surface-emitting semiconductor lasers," *Journal of the Optical Society of America B-Optical Physics,* vol. 14, pp. 449-453, Feb 1997.

[32] G. Heliotis, R. Xia, D. D. C. Bradley, G. A. Turnbull, I. D. W. Samuel, P. Andrew, and W. L. Barnes, "Two-dimensional distributed feedback lasers using a broadband, red polyfluorene gain medium," *Journal of Applied Physics,* vol. 96, pp. 6959-6965, Dec 15 2004.

[33] P. Del Carro, A. Camposeo, R. Stabile, E. Mele, L. Persano, R. Cingolani, and D. Pisignano, "Near-infrared imprinted distributed feedback lasers," *Applied Physics Letters,* vol. 89, pp. -, Nov 13 2006.

[34] Z. Y. Li, Z. Y. Zhang, T. Emery, A. Scherer, and D. Psaltis, "Single mode optofluidic distributed feedback dye laser," *Optics Express,* vol. 14, pp. 696-701, Jan 23 2006.

[35] M. Gersborg-Hansen and A. Kristensen, "Optofluidic third order distributed feedback dye laser," *Applied Physics Letters,* vol. 89, pp. -, Sep 4 2006.

[36] M. Gersborg-Hansen and A. Kristensen, "Tunability of optofluidic distributed feedback dye lasers," *Optics Express,* vol. 15, pp. 137-142, Jan 8 2007.

[37] D. Psaltis, S. R. Quake, and C. H. Yang, "Developing optofluidic technology through the fusion of microfluidics and optics," *Nature,* vol. 442, pp. 381-386, Jul 27 2006.

[38] S. Balslev and A. Kristensen, "Microfluidic single-mode laser using high-order Bragg grating and antiguiding segments," *Optics Express,* vol. 13, pp. 344-351, Jan 10 2005.

[39] J. C. Galas, J. Torres, M. Belotti, Q. Kou, and Y. Chen, "Microfluidic tunable dye laser with integrated mixer and ring resonator," *Applied Physics Letters,* vol. 86, pp. -, Jun 27 2005.

[40] Z. Y. Li, Z. Y. Zhang, A. Scherer, and D. Psaltis, "Mechanically tunable optofluidic distributed feedback dye laser," *Optics Express,* vol. 14, pp. 10494-10499, Oct 30 2006.

[41] D. V. Vezenov, B. T. Mayers, R. S. Conroy, G. M. Whitesides, P. T. Snee, Y. Chan, D. G. Nocera, and M. G. Bawendi, "A low-threshold, high-efficiency microfluidic waveguide laser," *Journal of the American Chemical Society,* vol. 127, pp. 8952-8953, Jun 29 2005.

[42] Y. N. Xia and G. M. Whitesides, "Soft lithography," *Annual Review of Materials Science,* vol. 28, pp. 153-184, 1998.

[43] H. Makamba, J. H. Kim, K. Lim, N. Park, and J. H. Hahn, "Surface modification of poly(dimethylsiloxane) microchannels," *Electrophoresis,* vol. 24, pp. 3607-3619, Nov 2003.

[44] L. P. Tang, M. S. Sheu, T. M. Chu, and Y. H. Huang, "Anti-inflammatory properties of triblock siloxane copolymer-blended materials," *Biomaterials,* vol. 20, pp. 1365-1370, Aug 1999.

[45] Y. N. Xia, J. A. Rogers, K. E. Paul, and G. M. Whitesides, "Unconventional methods for fabricating and patterning nanostructures," *Chemical Reviews,* vol. 99, pp. 1823-1848, Jul 1999.

[46] T. W. Odom, J. C. Love, D. B. Wolfe, K. E. Paul, and G. M. Whitesides, "Improved pattern transfer in soft lithography using composite stamps," *Langmuir,* vol. 18, pp. 5314-5320, Jun 25 2002.

[47] J. P. Rolland, E. C. Hagberg, G. M. Denison, K. R. Carter, and J. M. De Simone, "High-resolution soft lithography: Enabling materials for nanotechnologies," *Angewandte Chemie-International Edition,* vol. 43, pp. 5796-5799, 2004.

[48] J. N. Lee, C. Park, and G. M. Whitesides, "Solvent compatibility of poly(dimethylsiloxane)-based microfluidic devices," *Analytical Chemistry,* vol. 75, pp. 6544-6554, Dec 1 2003.

[49] H. Schmid and B. Michel, "Siloxane polymers for high-resolution, high-accuracy soft lithography," *Macromolecules,* vol. 33, pp. 3042-3049, Apr 18 2000.

[50] K. M. Choi, "Photopatternable silicon elastomers with enhanced mechanical properties for high-fidelity nanoresolution soft lithography," *Journal of Physical Chemistry B,* vol. 109, pp. 21525-21531, Nov 24 2005.

[51] M. Bender, U. Plachetka, J. Ran, A. Fuchs, B. Vratzov, H. Kurz, T. Glinsner, and F. Lindner, "High resolution lithography with PDMS molds," *Journal of Vacuum Science & Technology B,* vol. 22, pp. 3229-3232, Nov-Dec 2004.

[52] N. Koo, U. Plachetka, M. Otto, J. Bolten, J. H. Jeong, E. S. Lee, and H. Kurz, "The fabrication of a flexible mold for high resolution soft ultraviolet nanoimprint lithography," *Nanotechnology,* vol. 19, pp. -, Jun 4 2008.

[53] N. Koo, M. Bender, U. Plachetka, A. Fuchs, T. Wahlbrink, J. Bolten, and H. Kurz, "Improved mold fabrication for the definition of high quality nanopatterns by soft UV-nanoimprint lithography using diluted PDMS material," *Microelectronic Engineering,* vol. 84, pp. 904-908, May-Aug 2007.

[54] J. P. Rolland, R. M. Van Dam, D. A. Schorzman, S. R. Quake, and J. M. DeSimone, "Solvent-resistant photocurable "liquid teflon" for microfluidic device fabrication," *Journal of the American Chemical Society,* vol. 126, pp. 2322-2323, Mar 3 2004.

[55] T. T. Truong, R. S. Lin, S. Jeon, H. H. Lee, J. Maria, A. Gaur, F. Hua, I. Meinel, and J. A. Rogers, "Soft lithography using acryloxy perfluoropolyether composite stamps," *Langmuir,* vol. 23, pp. 2898-2905, Feb 27 2007.

[56] M. A. Unger, H. P. Chou, T. Thorsen, A. Scherer, and S. R. Quake, "Monolithic microfabricated valves and pumps by multilayer soft lithography," *Science,* vol. 288, pp. 113-116, Apr 7 2000.

[57] J. Adjaye, R. Daniels, V. Bolton, and M. Monk, "cDNA libraries from single human preimplantation embryos," *Genomics,* vol. 46, pp. 337-44, 1997.

[58] L. Rambhatla, B. Patel, N. Dhanasekaran, and K. E. Latham, "Analysis of G protein alpha subunit mRNA abundance in preimplantation mouse embryos using a rapid, quantitative RT-PCR approach," *Molecular Reproduction & Development,* vol. 41, pp. 314-24, 1995.

[59] M. K. Chiang and D. A. Melton, "Single-cell transcript analysis of pancreas development," *Developmental Cell,* vol. 4, pp. 383-93, 2003.

[60] F. Kamme and M. G. Erlander, "Global gene expression analysis of single cells," *Current Opinion in Drug Discovery & Development,* vol. 6, pp. 231-6, 2003.

[61] L. Luo, R. C. Salunga, H. Guo, A. Bittner, K. C. Joy, J. E. Galindo, H. Xiao, K. E. Rogers, J. S. Wan, M. R. Jackson, and M. G. Erlander, "Gene expression profiles of laser-captured adjacent neuronal subtypes.[erratum appears in Nat Med 1999 Mar;5(3):355]," *Nature Medicine,* vol. 5, pp. 117-22, 1999.

[62] I. Tietjen, J. M. Rihel, Y. Cao, G. Koentges, L. Zakhary, and C. Dulac, "Single-cell transcriptional analysis of neuronal progenitors," *Neuron,* vol. 38, pp. 161-75, 2003.

[63] D. A. Rappolee, A. Wang, D. Mark, and Z. Werb, "Novel method for studying mRNA phenotypes in single or small numbers of cells," *Journal of Cellular Biochemistry,* vol. 39, pp. 1-11, 1989.

[64] L. H. Trumper, G. Brady, A. Bagg, D. Gray, S. L. Loke, H. Griesser, R. Wagman, R. Braziel, R. D. Gascoyne, S. Vicini, and et al., "Single-cell analysis of Hodgkin and Reed-Sternberg cells: molecular heterogeneity of gene expression and p53 mutations," *Blood,* vol. 81, pp. 3097-115, 1993.

[65] G. Brady, F. Billia, J. Knox, T. Hoang, I. R. Kirsch, E. B. Voura, R. G. Hawley, R. Cumming, M. Buchwald, and K. Siminovitch, "Analysis of gene expression in a complex differentiation hierarchy by global amplification of cDNA from single cells.[erratum appears in Curr Biol 1995 Oct 1;5(10):1201]," *Current Biology,* vol. 5, pp. 909-22, 1995.

[66] A. K. Dixon, P. J. Richardson, K. Lee, N. P. Carter, and T. C. Freeman, "Expression profiling of single cells using 3 prime end amplification (TPEA) PCR," *Nucleic Acids Research,* vol. 26, pp. 4426-31, 1998.

[67] M. R. Emmert-Buck, R. F. Bonner, P. D. Smith, R. F. Chuaqui, Z. Zhuang, S. R. Goldstein, R. A. Weiss, and L. A. Liotta, "Laser capture microdissection.[comment]," *Science,* vol. 274, pp. 998-1001, 1996.

[68] C. A. Suarez-Quian, S. R. Goldstein, T. Pohida, P. D. Smith, J. I. Peterson, E. Wellner, M. Ghany, and R. F. Bonner, "Laser capture microdissection of single cells from complex tissues," *Biotechniques,* vol. 26, pp. 328-35, 1999.

[69] J. Eberwine, H. Yeh, K. Miyashiro, Y. Cao, S. Nair, R. Finnell, M. Zettel, and P. Coleman, "Analysis of gene expression in single live neurons," *Proceedings of the National Academy of Sciences of the United States of America,* vol. 89, pp. 3010-4, 1992.

[70] K. M. Schmidt-Ott, S. Tuschick, F. Kirchhoff, A. Verkhratsky, L. Liefeldt, H. Kettenmann, and M. Paul, "Single-cell characterization of endothelin system gene expression in the cerebellum in situ," *Journal of Cardiovascular Pharmacology,* vol. 31, pp. Suppl 1:S364-6, 1998.

[71] P. B. Crino, J. Q. Trojanowski, M. A. Dichter, and J. Eberwine, "Embryonic neuronal markers in tuberous sclerosis: single-cell molecular pathology," *Proceedings of the National Academy of Sciences of the United States of America,* vol. 93, pp. 14152-7, 1996.

[72] F. Kamme, R. Salunga, J. Yu, D. T. Tran, J. Zhu, L. Luo, A. Bittner, H. Q. Guo, N. Miller, J. Wan, and M. Erlander, "Single-cell microarray analysis in hippocampus CA1: demonstration and validation of cellular heterogeneity," *Journal of Neuroscience,* vol. 23, pp. 3607-15, 2003.

[73] S. Y. Ying, H. M. Lui, S. L. Lin, and C. M. Chuong, "Generation of full-length cDNA library from single human prostate cancer cells," *Biotechniques,* vol. 27, pp. 410-2, 1999.

[74] L. H. Trumper, G. Brady, S. Vicini, J. Cossman, and T. W. Mak, "Gene expression in single Reed Sternberg cells of Hodgkin's disease: results from PCR generated single cell cDNA libraries," *Annals of Oncology,* vol. 4, pp. 25-6, 1992.

[75] R. C. Roozemond, "Ultramicrochemical determination of nucleic acids in individual cells using the Zeiss UMSP-I microspectrophotometer. Application to

isolated rat hepatocytes of different ploidy classes," *Histochemical Journal,* vol. 8, pp. 625-38, 1976.

[76] E. Uemura, "Age-related changes in neuronal RNA content in rhesus monkeys (Macaca mulatta)," *Brain Research Bulletin,* vol. 5, pp. 117-9, 1980.

[77] G. Brady, "Expression profiling of single mammalian cells--small is beautiful," *Yeast,* vol. 17, pp. 211-7, 2000.

[78] Y. Hamaguchi, Y. Aso, H. Shimada, and M. Mitsuhashi, "Direct reverse transcription-PCR on oligo(dT)-immobilized polypropylene microplates after capturing total mRNA from crude cell lysates," *Clinical Chemistry,* vol. 44, pp. 2256-63, 1998.

[79] J. Zhang and C. D. Byrne, "Differential priming of RNA templates during cDNA synthesis markedly affects both accuracy and reproducibility of quantitative competitive reverse-transcriptase PCR," *Biochemical Journal,* vol. 337, pp. 231-41, 1999.

[80] H. P. Chou, M. A. Unger, and S. R. Quake, "A microfabricated rotary pump," *Biomedical Microdevices,* vol. 3, pp. 323-330, 2001.

[81] J. S. Marcus, W. F. Anderson, and S. R. Quake, "Parallel picoliter rt-PCR assays using microfluidics," *Analytical Chemistry,* vol. 78, pp. 956-8, 2006.

[82] L. Warren, D. Bryder, I. L. Weissman, and S. R. Quake, "Transcription factor profiling in individual hematopoietic progenitors by digital RT-PCR," *Proceedings of the National Academy of Sciences of the United States of America,* vol. 103, pp. 17807-12, 2006.

[83] M. Bengtsson, A. Stahlberg, P. Rorsman, and M. Kubista, "Gene expression profiling in single cells from the pancreatic islets of Langerhans reveals lognormal distribution of mRNA levels," *Genome Research,* vol. 15, pp. 1388-92, 2005.

[84] N. Rosenfeld, J. W. Young, U. Alon, P. S. Swain, and M. B. Elowitz, "Gene regulation at the single-cell level.[see comment]," *Science,* vol. 307, pp. 1962-5, 2005.

[85] J. R. Newman, S. Ghaemmaghami, J. Ihmels, D. K. Breslow, M. Noble, J. L. DeRisi, and J. S. Weissman, "Single-cell proteomic analysis of S. cerevisiae reveals the architecture of biological noise," *Nature,* vol. 441, pp. 840-6, 2006.

[86] P. S. Swain and A. Longtin, "Noise in genetic and neural networks," *Chaos,* vol. 16, 2006.

[87] G. M. Suel, R. P. Kulkarni, J. Dworkin, J. Garcia-Ojalvo, and M. B. Elowitz, "Tunability and noise dependence in differentiation dynamics," *Science,* vol. 315, pp. 1716-9, 2007.

[88] M. B. Elowitz, A. J. Levine, E. D. Siggia, and P. S. Swain, "Stochastic gene expression in a single cell.[see comment]," *Science,* vol. 297, pp. 1183-6, 2002.

[89] J. Ryley and O. M. Pereira-Smith, "Microfluidics device for single cell gene expression analysis in Saccharomyces cerevisiae," *Yeast,* vol. 23, pp. 1065-73, 1065.

[90] J. A. Thomson, J. Itskovitz-Eldor, S. S. Shapiro, M. A. Waknitz, J. J. Swiergiel, V. S. Marshall, and J. M. Jones, "Embryonic stem cell lines derived from human blastocysts.[see comment][erratum appears in Science 1998 Dec 4;282(5395):1827]," *Science,* vol. 282, pp. 1145-7, 1998.